

IDOM

Liquid Lithium solid impurities cyclone separator

First Light Fusion

01/2024

Chemical assessment of particulate impurities

S022641 / SIM0001 v.0

NUCLEAR SERVICES

DRAFT

Total or partial reproduction, transfer, distribution or storage of part or all of the contents in this document by any kind of digital media, printing or any other kind is prohibited without the prior written permission of IDOM, Consulting, Engineering & Architecture, S.A.U.

Copyright ©2024, IDOM, Consulting, Engineering & Architecture, S.A.U.



first light

First Light Fusion
Liquid Lithium solid impurities cyclone separator

<i>Performed by:</i>	<i>Reviewed by:</i>	<i>Approved by:</i>
Alexandre Sureda (ASC) Fernando Scarafia (FS) Juan Diego Iberico (DIL)	Andhika Feri Wibisono (AFW)	Beatriz Echeste (BE)
3/2024	3/2024	3/2024

<i>Project</i> <i>ID:</i> Quality:	<i>Document</i> <i>SIM0001</i>	<i>Version</i> <i>v.0</i>	<i>CD</i> <i>S022641.04.02</i>
--	---------------------------------------	----------------------------------	---------------------------------------

DRAFT

Intentionally left blank

RECORD OF CHANGES

<i>Version</i>	<i>Date</i>	<i>Changes</i>
v.0	01/2024	Draft version

CHANGES TO PREVIOUS VERSION

N/A

PENDING INFORMATION

<i>No.</i>	<i>Section</i>	<i>Description</i>
N/A	N/A	N/A

DRAFT

Intentionally left blank

Contents

1 EXECUTIVE SUMMARY	13
2 INTRODUCTION AND BACKGROUND	14
3 SCOPE	15
3.1 Exceptions	15
3.2 Exclusions	15
4 STRUCTURE OF THE DOCUMENT	16
5 METHODOLOGY	17
6 INPUTS	18
7 IMPURITY AND CORROSION ANALYSIS	19
7.1 Impurities Matrix	19
7.1.1 Lithium initial impurities	19
7.2 Corrosion Products	21
7.3 Maroni's Process	22
8 CHEMICAL ANALYSIS	24
8.1 Nucleation Theory	24
8.1.1 Driving force	26
8.1.2 Surface energy	31
8.2 Kinetic theory	34
8.3 Impurities results	40
8.3.1 Metallic impurities	40
8.3.2 Non-metallic impurities	52
9 CENTRIFUGAL TECHNOLOGY SELECTION	61
9.1 Single Step Separation Approach	61
9.2 Multi-Step Separation Approach	66
9.3 Hydrocyclone: Mathematical modelling	68
9.4 Fluid model	69
9.5 Motion of suspended particles	70
9.6 Cyclone effective volume	71
9.7 Residence time model	72
9.8 Separation efficiency model	72
10 Results: Parametric analysis	73
10.1 Parametric analysis: Temperature	73

10.2 Parametric analysis: Cyclone diameter	74
10.3 Parametric analysis: volumetric inlet flow rate	75
10.4 Optimization methodology	76
10.4.1 Geometrical optimization	76
10.4.2 Optimization: Results	77
10.5 Conceptual Design Approach	81
11 CONCLUSIONS	82
REFERENCES	83
ANNEX 1	89

DRAFT

List of Figures

5-1 Methodology	17
7-1 Initial lithium impurities.	19
7-2 Schematic diagram of a molten-salt extraction diagram [15].	22
8-1 Required free energy, as per classical nucleation theory, for the formation of a cluster of size i . Curves represent different constant values of supersaturation and temperature, illustrating the free energy barrier associated with the critical size.	27
8-2 Simulation and reference size dependent free energy of clusters for the uncorrected classical droplet model, CNT.	36
8-3 Effect of upper boundary condition comparison between simulation and reference cluster number density distribution for different sizes $i_{\max} = 40$ and 100	37
8-4 Effect of upper boundary condition comparison between simulation and reference postcritical nucleation rates for different sizes $i_{\max} = 40$ and 100	38
8-5 Effect of upper boundary condition comparison between simulation and reference postcritical total cluster number density for different sizes $i_{\max} = 40$ and 100	38
8-6 Nucleation rates for different observable sizes for closed- boundary (top) and open-boundary(bottom) for $i_{\max} = 40$ (left) and 100 (right).	39
8-7 Total number density for different observable sizes for closed- boundary (top) and open-boundary(bottom) for $i_{\max} = 40$ (left) and 100 (right).	40
8-8 Phase diagram of Li-Fe mixture from FactSage database [58].	41
8-9 Fe solubility in liquid lithium dependence on temperature ??	41
8-10 Iron cluster number density distribution for different sizes $i_{\max} = 400$ and 900	44
8-11 Iron nucleation rates for different sizes $i_{\max} = 400$ and 900	44
8-12 Iron postcritical total number density for different sizes $i_{\max} = 400$ and 900	45
8-13 Iron nucleation rates for different observable sizes for $i_{\max} = 400$ (left) and 900 (right).	45
8-14 Iron postcritical total number density for different observable sizes for $i_{\max} = 400$ (left) and 900 (right).	46
8-15 Phase diagram of Li-Cr mixture from FactSage database [58].	47
8-16 Cr solubility in liquid lithium dependence on temperature ??	47
8-17 Chromium cluster number density distribution for different sizes $i_{\max} = 200$ and 600	48
8-18 Chromium nucleation rates for different sizes $i_{\max} = 200$ and 600	49
8-19 Chromium postcritical total number density for different sizes $i_{\max} = 200$ and 600	50
8-20 Iron nucleation rates for different observable sizes for $i_{\max} = 200$ (left) and 600 (right).	51
8-21 Iron postcritical total number density for different observable sizes for $i_{\max} = 200$ (left) and 600 (right).	51
8-22 Temperature dependence of hydrogen isotope solubility in lithium. [58].	52
8-23 Temperature dependence of hydrogen isotope solubility in lithium.	54
8-24 LiH phase diagram from FactSage database (left) and for [65] (right).	55

8-25 Hydrides cluster number density distribution for $i_{\max} = 1000$	57
8-26 Hydrides postcritical nucleation rates for $i_{\max} = 1200$	58
8-27 Hydrides postcriticalnumber density for $i_{\max} = 1200$	59
8-28 Hydrides nucleation rates (deuterium (left) and tritium (right)) for $i_{\max} = 1200$	59
8-29 Hydrides nucleation rates (deuterium (left) and tritium (right)) for $i_{\max} = 1200$	60
9-1 Centrifugal technologies comparison chart	62
9-2 Hydrocyclone vs Disk Stack separator: radar plot results	62
9-3 Multi stage configuration	66
9-4 Multi stage device data-sheet	67
9-5 Schematic diagram of typical cyclone dimensions.	69
9-6 Scheme of the 2 ideal vortex model and the tangential velocity distribution in a real vortex. ref.[73]	70
9-7 volume of control used in the separation efficiency model. ref.[71]	72
10-1 Separation efficiency as a function of the particle diameter of Fe for different temperatures.	74
10-2	74
10-3	75
10-4	76
10-5	78
10-6 Conceptual design approach: possible lines of work	81

List of Tables

7-1	Lithium initial impurities concentration ref. [3].	20
7-2	Corrosion Effects of Impurities in Liquid Lithium on Materials.	21
7-3	Maroni process: advantages/disadvantages [15], [16].	23
8-1	Simplified set of physical properties of LS ₂	36
8-2	Equilibrium compositions of iron using FactSage and reference data.	42
8-3	Equilibrium compositions of iron using FactSage with an iron molar fraction used as input.	42
8-4	Equilibrium compositions of iron using FactSage with an iron molar fraction increased to $x_l^A = 9.2880 \times 10^{-5}$	42
8-5	Parameters for Fe	43
8-6	Critical values for Fe	43
8-7	Equilibrium compositions of iron using FactSage and reference data.	48
8-8	Equilibrium compositions of chromium using FactSage with a chromium molar fraction used as input.	48
8-9	Equilibrium compositions of chromium using FactSage with a chromium molar fraction increased to $x_l^A = 1.1190 \times 10^{-5}$	49
8-10	Parameters for Cr	49
8-11	Critical values for Cr	50
8-12	Solubility of hydrogen isotopes in lithium	54
8-13	Hydrogen nuclides production	55
8-14	Parameters for LiH, LiD, and LiT	56
8-15	Critical values for H, D, and T	56
9-1	Description of the geometrical variables of one cyclone.	69
10-1	Input information used for the parametric analysis section	73
10-2	Volumetric flow rate for the pilot and commercial plant calculated in ref. [75]	78
10-3	Cyclone optimization results	79
11-1	Centrifugal separator comparison data-sheet	89

MEASUREMENT SYSTEM IDENTIFICATION

International System of Units (see ref. [1]).

GLOSSARY OF TERMS

Term	Term definition
Fusion	Nuclear reaction that results in the union of two or more nuclei resulting in an excess of energy
RTPR	Reference Theta-Pinch Reactor tor2
v	Velocity [m/s]
Q/VFR	Volumetric flow rate [m^3/s]
\dot{m}/MFR	Mass flow rate [kg/s]
$v_{.,f}$	Fluid velocity [m/s]
$v_{.,p}$	Particle velocity [m/s]
$v_{r,..}$	Radial velocity [m/s]
$v_{\theta,..}$	Tangential velocity [m/s]
V	Volume [m^3]
V_{cs}	Cyclone effective volume [m^3]
c	Specific concentration [mol/m^3]
d_p	Particle diameter [m]
t_{res}	Residence time [s]
η	Separation efficiency
$d_{p,c}$	Cut particle diameter [m], diameter for which there is 50% separation

1 EXECUTIVE SUMMARY

XXXXXXXXXXXXXXXXXXXXXX

DRAFT

2 INTRODUCTION AND BACKGROUND

First Light Fusion (FLF) inertial confinement fusion device is based on the nuclear reaction induced by the impact of a high-speed projectile onto a target mainly made of the fusion fuel (D-T). The use of Liquid Lithium (LL) in form of jet array in the Reactor Chamber (RC) plays a key role as tritium breeder, primary carrier of energy throughout the system, heat and nuclear shielding.

Taking into account that the primary carrier of energy is the LL, its circulation through the system is key to achieve the desired power cycle. This involves ensuring optimal circulation within the primary loop to maximize desired outcomes, such as purification of liquid metal from impurities introduced during operation and efficient management of tritium generated by neutron interactions for overall fuel cycle efficiency.

Considering the requirement to achieve an impurities control in the LL loop of the RC system, the current project studies the feasibility to separate the solid impurities from the liquid metal by means of centrifugal technologies. The first deliverable ref. [2] explored the different technologies that potentially could address the LL loop purification.

The objective of the present document is to study from chemical point of view the feasibility of separate the solids impurities from the liquid media (LL), by means of Classical Nucleation Theory (CNT) where fundamental parameters such as critical radius, and its evolution by means of nucleation in the media.

3 SCOPE

The present document is part of three deliverables: the first deliverable ref. [2] addressed the SoA of centrifugal technologies. The second deliverable (which is the current document) is focused in the chemical analysis of the impurities and the technology selection for the centrifuge device, being more specific:

- **Impurity and Corrosion Analysis:**

- Impurities matrix, given different source.
- Corrosion products identification.
- Maroni's process analysis.

- **Chemical analysis:**

- Particle Size Distribution (PSD) by means of CNT, for the given FLF impurities:

- * Fe
- * Cr
- * AlN
- * Li₂O
- * LiQ
- * Li₂C₂

- Impurity critical radius time-evolution: Nucleation analysis.
- Homogeneous precipitation: advective-reacting diffusion equation.

- **Centrifugal technology selection:**

- Single step separation stage approach.
- Multi-step separation stage approach.
- Conceptual design approach.
- Thermo-hydraulic analytical model.

3.1 Exceptions

N/A

3.2 Exclusions

N/A

4 STRUCTURE OF THE DOCUMENT

The present document it is divided in three main blocks, as per the scope section 3 list. The blocks are divided by disciplines: impurities analysis SoA, chemical assessment, and engineering assessment including the thermo-hydraulic solid separator mathematical model.

Section 7 reviews the impurities and corrosion products in the FLF primary loop. The source of impurities are analyzed from chemical perspective in order to establish a baseline for future analysis. At the same time, a subsection is dedicated to review in the literature the corrosion products from the interaction of liquid lithium with the pipelines made SS316-Ti. The last subsection discusses the Maroni method for tritium extraction and addresses its advantages/disadvantages.

Section 8 is deeply dedicated to the chemical analysis of the impurities, specially focused on six impurities (established by FLF: Fe, Cr, AlN, Li₂O, LiQ, Li₂C₂) studying the Particle Size Distribution and its temporal evolution to establish the critical radius of the impurities. A specific analysis has been carried to explain the solvers and convergence benchmarks for the Ordinary Differential Equations (ODE's) system develop to understand the different phenomena. Finally, for the non-metallic impurities, a dedicated analysis is the precipitation of those impurities by means of advective-reacting diffusion equation model.

Section 9 studies the single and multi-step solid separators with the aim to select the most appropriate centrifugal system for the FLF purification process for the primary loop. Mathematical model has been developed of a solid separator to study different parameter in order to set the possible efficiencies of the device per particle size. Finally, the section describes which device should be studied in the next stage of the current project, from a design and CFD point of view.

5 METHODOLOGY

The development of the present document follows a methodology (figure 5-1) based on three lines of work by discipline (SoA, Chemistry,) that run by batches (presented in box form and sub-tasks). Besides the tasks runs in parallel, they are transversal to all disciplines in terms of technical results, as per the interaction of the outputs and intermediate results.

The figure 5-1 presents the diagram of the methodology and the expected outputs per batch & disciplines.

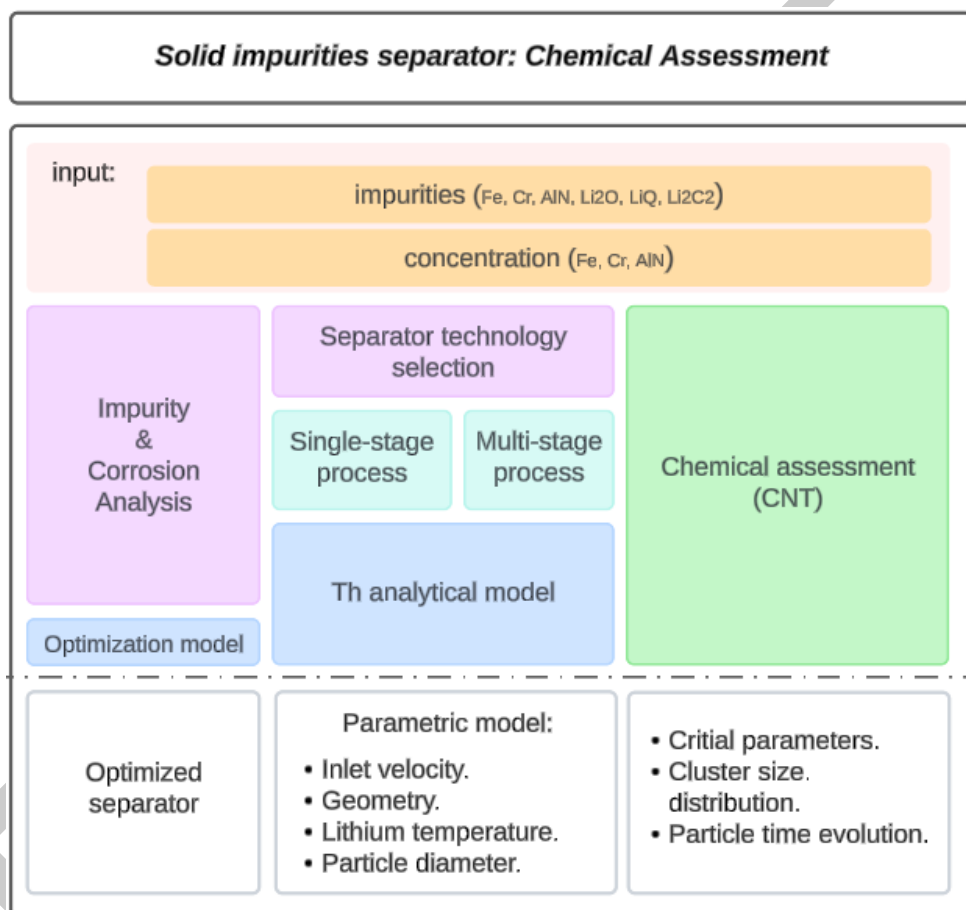


Figure 5-1: Methodology

6 INPUTS

To accurately analyze the impact of the impurities from chemical point of view, the following assumptions based on FLF input has been considered to target the impurities concentration, as follows:

Inputs & Assumptions

The metallic impurities are calculated in the following manner:

- **135.000 kg/yr** of insoluble metal per year are generated as impurity.
- **8000 hr/yr** of Reactor Chamber (RC) operation.
- Assumed concentration:
 - 80% Fe
 - 10% Cr
 - 10% AlN
- **1/10 Hz** of Pulsed operation.
- **439.38 Tn** of LL in the loop.

Impurities mass produced in 1 pulse in the entire LL loop: **0.421 Kg**

Where the concentrations are:

- Fe = 0.00839 mol/m³
- Cr = 0.00112 mol/m³
- AlN = 0.00142 mol/m³

With an impurities ratio:

- Li = 0.999 e-00
- Fe = 1.201 e-07
- Cr = 1.613 e-08
- AlN = 2.046 e-08

7 IMPURITY AND CORROSION ANALYSIS

7.1 Impurities Matrix

Within the scope of the current document, the identification of the impurities source and its main properties is key to provide the necessary context for the coming sections. Given the FLF machines and components, such as: machine gun (upper launcher), Reactor Chamber (RC), and the liquid lithium primary loop, the identified impurity sources are:

- **Lithium initial impurities.**
 - **Corrosion:** mainly given by the primary loop (piping and components) made of SS316-Ti, it is assumed at some point the RC vessel made of P91 will be a secondary source of corrosion impurities. The section 7.2 is dedicated to identify the corrosion products, mechanisms, and its source.
 - **Pulsed shot (projectile + target):** considering the input metallic impurities given by FLF (Fe, Cr, AlN), it is assumed in the current document that part of these impurities will be generated at the pulsed operation due to the projectile impact with the target, example of this is the presence of Cr. Future studies will be necessary to identify and classify the impurities result of the pulsed operation.

7.1.1 Lithium initial impurities

The initial lithium impurities is a key source in terms of traceability, even more considering that these impurities can mutate within the system under neutronic irradiation. The Figure 7-1 shows the list of impurities, ranked in the horizontal axis by concentration and vertically the density of element.

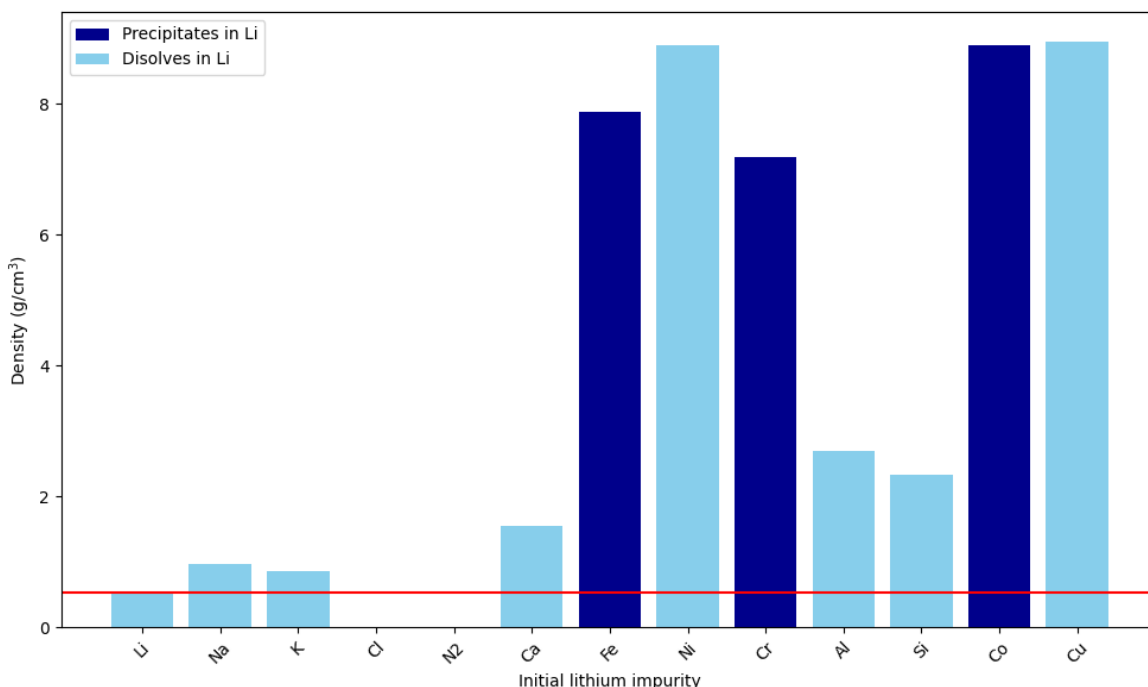


Figure 7-1: Initial lithium impurities.

xxxxxxxxxxxxxxxxxxxxxxxxxxxx explanation here about the results in the graph,

Element	Content	Density
Li	99.98 %	0.534 g/cm ³
Na	0.0034 %	0.971 g/cm ³
K	0.0032 %	0.862 g/cm ³
Cl	0.0031 %	0.003214 g/cm ³
N ₂	0.0020 %	0.001250 g/cm ³
Ca	< 0.001 %	1.550 g/cm ³
Fe	< 0.001 %	7.874 g/cm ³
Ni	< 0.001 %	8.900 g/cm ³
Cr	< 0.001 %	7.190 g/cm ³
Al	< 0.001 %	2.702 g/cm ³
Si	< 0.001 %	2.330 g/cm ³
Co	< 0.001 %	8.900 g/cm ³
Cu	< 0.001 %	8.960 g/cm ³

Table 7-1: Lithium initial impurities concentration ref. [3].

7.2 Corrosion Products

The deliverable [2], listed the lithium impurities and how they are related with the corrosion products together with the effects in steel pipework (SS316). The current section, aims to provide more information gathered from the literature, producing the following table:

Li impuri-ties	Effect on Materi-als	Corrosion Product	Conditions/Notes	References
Nitrogen	General dissolution and intergranular penetration in stainless steel.	Primary attack via chromium forming Li9CrN5 and iron forming Li3FeN2.	High nitrogen levels lead to corrosion at temperatures between 400-600 °C.	[4], [5], [6], [7]
Oxygen	Formation and dissolution of unstable ternary oxides.	Li5FeO4, LiCrO2, Li2Ni8O17 formed between Li2O and steels.	Limited information, reactions involve Li2O interacting with Fe, Cr	[8], [9], [10]
Carbon	Formation of Cr23C6 precipitates on stainless steel surfaces.	Cr23C6 precipitates enhance chromium concentration at the surface.	Higher weight loss in type 316 stainless steel compared to 9Cr1Mo ferritic steel.	[11]
Hydrogen	Significant decarburisation of stainless steel. Formation of new phase $Fe_{50}Cr_{43}Mo_3Ni_4$ on steel surface exposed at 700 °C showing intergranular corrosion.	Decrease in carbon content more pronounced in austenitic steel.	Affects both austenitic and ferritic/martensitic steels.	[11] [12]
Aluminium	Not known to cause corrosion in stainless steel directly.	Addition of Al reduces weight loss in stainless steel; may form AlN in presence of dissolved nitrogen.	Adding 5wt% Al to lithium reduced weight loss of type 316 stainless steel.	[13], [4]
No impuri-ties added.	The austenitic area in the welded joint showed morphological changes induced by the dissolution of Ni in Li. The ferritic parts exhibit a fine-grained surface structure.	$M_{23}C_6$ and NiC_x particles in sizes of 1-2 μm .	Study of welded joints (SS316 and SS410) in liquid lithium.	[12], [14]

Table 7-2: Corrosion Effects of Impurities in Liquid Lithium on Materials.

7.3 Maroni's Process

The Maroni process has been studied in the SoA deliverable ref. [2], where the process diagram Figure 7-2 of a molten-salt extraction and its stages were analyzed. Nevertheless, the current section is focused in study the advantages/disadvantages of Maroni process, presented in Table 7-3.

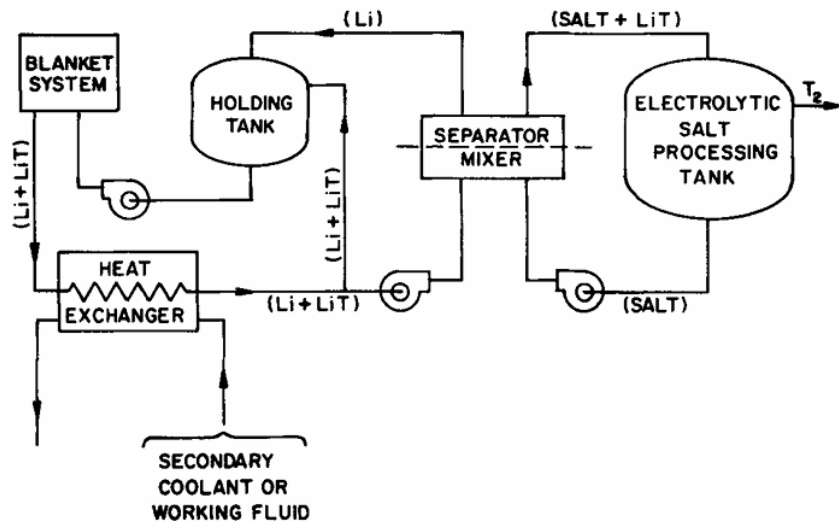


Figure 7-2: Schematic diagram of a molten-salt extraction diagram [15].

Before jumping in the Table 7-3, it is important to remind the Maroni process: based on high temperature molten mixed alkali-metals halide salts (LiCl-KCl at 530 °C) as an extraction solvent for the Li + LiT.

Advantages

Continuous tritium extraction: The capability to maintain a steady-state tritium inventory within the lithium loop has been incorporated as a critical consideration in the design of the RTPR. This aspect of the design underscores the importance of ensuring a consistent tritium flow and concentration within the system, which is fundamental to the reactor's operational efficiency and safety.

Disadvantages

Solubility: At the operational temperatures of mixing/separating the lithium and salts, the saturation solubility will be reached in the other. The main concern is the presence of salt dissolved in lithium, being significant in terms of corrosion and the products formed under neutronic irradiation (with regard of long-lived radioactive-isotope from the presence of KCl in the lithium jets).

Advantages	Disadvantages
<p>Tritium-salts affinity: The distribution coefficients for 500-600 °C are 2.6 for volumetric distribution and 5.8 for molar distribution, being the ratio of tritium content in the salt (T_{salt}) to tritium content in lithium (T_{Li}) demonstrating that distributions of LiT between the salt and metal phases can be achieved. This advantage of tritium-salts affinity, might allow tritium recovery in the HEX system.</p>	<p>Required potential (V): The extraction of tritium from the salt medium is proposed to be conducted via electrolysis at a potential of 1.5V. However, this process is constrained by the limitation that salt decomposition occurs at potentials exceeding 2.0V. Consequently, to maintain the integrity of the salt medium while ensuring a steady-state tritium inventory, the efficiency of the tritium recovery process must be optimized for operation at the designated 1.5V potential.</p>
<p>Density: Lithium density is less dense than the molten salt by a factor or 3, thus leading to exploit separation system from gravitational settling to centrifugal action. The later separation system could be exploited with hydrocyclones due to its efficiency and low energy cost.</p>	<p>Corrosion: The interaction of materials with lithium, particularly in contexts requiring controlled corrosion rates, remains a significant area of ongoing research. This challenge is further intense in scenarios involving lithium-salt mixtures within mixing/separator devices. To mitigate these issues, the employment of specialized alloys, such as Niobium, was studied in the literature. However, the selection of appropriate materials for lithium loops presents complex considerations, notably due to the specific corrosion behaviors and operational temperature demands associated with fusion nuclear environments.</p>
	<p>Volatile elements: The use of electrolytic process to extract the tritium from salts could involve potential volatile elements such as hydrogen chloride, hydrogen fluoride, hydrogen bromide or its tritium analogs have a direct impact in the feasibility of the tritium extraction in form of gas. Recent studies mitigate the volatile using benign lithium hydroxide (LiOH) or lithium carbonate (Li_2CO_3).</p>

Table 7-3: Maroni process: advantages/disadvantages [15], [16].

8 CHEMICAL ANALYSIS

This section investigates the nucleation of impurities within liquid lithium, which serves as a breeder and shielding material in the reaction chamber. The nucleation of impurities within liquid lithium poses a complex challenge, impacting not only the material's thermal and physical properties but also the safety and longevity of the fusion reactors. Despite its significance, the study of impurity nucleation in liquid lithium remains underexplored, with limited literature providing a comprehensive understanding of these mechanisms.

Due to the objective of using purification processes based on centrifugation phenomena, the limiting factor of these impurities will be their densities, the quantities in which they are present and above all the particle size of these impurities. Therefore, as a starting point for the characterisation of these impurities from a thermodynamic and kinetic point of view, classical nucleation theory (CNT) and kinetic theory have been used to study the evolution and speed of this phenomenon.

The primary issue with this model stems from its oversimplifications, which will be detailed in subsequent sections. A significant limitation is that these models originate from statistical mechanics, constraining them to a limited number of particles. Specifically, when examining clusters of macroscopic particles on the scale of micrometers, employing statistical mechanics or molecular dynamics models proves impractical. Consequently, for such scales, the application of continuous models becomes more appropriate, examples of which include phase field models [17, 18], computational fluid dynamics or precipitation dynamics [19].

Furthermore, this research can serve as a foundational basis for applying continuous models more effectively. For instance, one could enhance these models by incorporating the distributions of nanometric particles within the system as input parameters.

This section is structured for clarity and comprehension, starting with an explanation of classical nucleation theory and the thermodynamics of the nucleation process. This is followed by an analysis of the kinetic treatment of the process. The section concludes with the characterization of each impurity.

8.1 Nucleation Theory

First-order phase transitions, such as the condensation of vapor, boiling of a liquid, and crystallization of a melt, are critical phenomena in materials science and thermodynamics. The decay of metastable states, such as the solidification of a supercooled liquid, takes place through the nucleation and growth of some small-sized clusters within the system [20]. The initial stage of the phase transformation is usually described within the time-honored CNT [21, 22], where the droplet is described as a sphere of, say, bulk solid, separated from the liquid by a sharp interface, giving rise to a free-energy penalty proportional to the interface area and a total Gibbs-free-energy activation barrier.

$$\Delta G(i) = -|\Delta\mu|i + A\gamma_\infty i^{2/3}, \quad (1)$$

where i is the number of particles in the cluster, $\Delta\mu < 0$ is the chemical potential difference between

the two phases, $A = (36\pi\nu^2)^{1/3}$ being ν the molecular volume and γ_∞ the specific surface energy (surface tension) of the planar interface, all anisotropies being neglected at this stage. The droplet grows if it exceeds a critical size i^* corresponding to the maximum $\Delta G(i)$ ($\equiv \Delta G^*$). The CNT relies on the liquid droplet model, which assumes that tiny droplets possess the same characteristics as the bulk condensed phases and have surface energies identical to those of an infinite flat surface. Nonetheless, there is an ongoing debate about the applicability of macroscopic thermodynamic principles to describe liquid drops when dealing with small clusters composed of merely a few dozen molecules [23]. The inadequacy of the droplet model for small particles is highlighted by the fact that the energy required to form monomers is not zero [24]. This indicates that the attributes of small clusters cannot be simply categorized into bulk and surface properties, rendering the notion of surface tension somewhat misleading when applied to these clusters [25]. For instance, the 'monomers' of the new phase are indistinguishable from the molecules of the parent phase, leading to the conclusion that the free energy of monomers should logically be zero ($\Delta G(1) = 0$) [26].

However, in the conceptual state of this work, this simple model is useful to provide quantitatively and qualitatively the critical size of these nuclei.

CNT also is able to estimate the nucleation rate

$$I = I_0 e^{-\beta \Delta G^*}, \quad (2)$$

where $\beta = 1/(k_B T)$ is the inverse temperature and I_0 a kinetic prefactor that varies slowly with T . Clearly, this connection between I and γ_∞ relies on several severe approximations. Moreover, I_0 is notoriously influenced by genuinely non-equilibrium effects and various expressions resulting from a more detailed consideration of the nucleation kinetics are known since a long time [22].

In the nucleation regime, the evolution of the system is significantly marked by the formation of clusters that represent a new equilibrium phase. The dynamics of this process are intricately governed by the balance between volume and surface contributions, as encapsulated by the capillary approximation. The volume contribution, acting as the driving force behind nucleation, lowers the system's free energy and is directly proportional to the cluster's volume, thereby favoring the formation and growth of these clusters. Conversely, the surface contribution introduces an energetic cost, scaling with the cluster's surface area. This cost is associated with creating an interface between the original phase and the new cluster, serving as a barrier that inherently inhibits the growth of the cluster [27].

The critical size of the nucleus and the nucleation barrier are determined by setting the derivative of ΔG with respect to the size, i , equal to zero:

$$R^* = -2\gamma_\infty(\Delta\mu/\nu)^{-1}, \quad (3)$$

and

$$\Delta G^* = \frac{16\pi}{3}\gamma_\infty^3(\Delta\mu/\nu)^{-2}. \quad (4)$$

Analyzing the critical parameters obtained from the CNT, is it evident that the key variables of the model are the nucleation driving force and the surface energy. In the following sections, some formalisms for the driving force will be presented and discussed, as well as for the surface energy.

8.1.1 Driving force

The nucleation driving force is obtained by considering the difference in chemical potentials between the parent and the equilibrium phases for all atoms composing the cluster:

$$\Delta\mu = \sum_i y_i^e (\mu_i^e - \mu_i^0), \quad (5)$$

where y_i^e is the atomic fraction of type i atoms in the nucleating equilibrium phase, and μ_i^e and μ_i^0 are the corresponding chemical potentials in the nucleating equilibrium phase and in the parent phase, respectively. In a metastable parent phase, chemical potentials are higher than those at equilibrium. The critical factors for applying CNT are the driving force, $\Delta\mu$, and the surface energy, γ_∞ , of the solid particle. The driving force depends on the nucleation pathway, such as the saturation-based formalism commonly used in the context of vapor to liquid or crystal transitions [28, 29, 30]:

$$\Delta\mu = \mu - \mu_{\text{coex}} = kT \ln \left(\frac{n_1}{n_1^{\text{sat}}} \right), \quad (6)$$

where the chemical potential is represented using the ideal gas expression, introducing a monomer density $n_1^{\text{sat}}(T)$ appropriate to a saturated vapor, i.e., a gas phase in coexistence with the condensed phase at the environmental temperature. The ratio of the monomer density in a metastable vapor to its value in a saturated vapor defines the supersaturation, S :

$$\Delta\mu = kT \ln S. \quad (7)$$

This driving force dictates the nucleation process, which is governed by temperature, the degree of supersaturation, and the interfacial energy. The nucleation rate increases with the degree of supersaturation and temperature and decreases with the interfacial energy. This behavior is illustrated in Figure 8-1, which shows the energy barrier that must be overcome to form a new phase for various degrees of supersaturation.

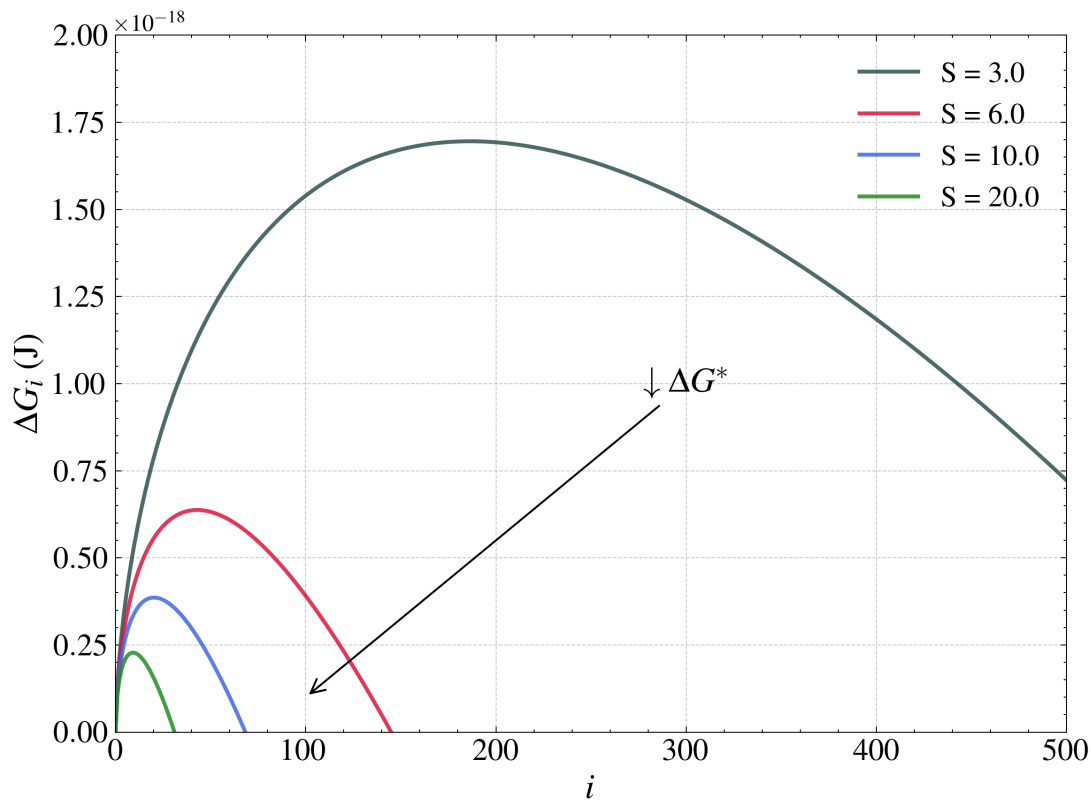


Figure 8-1: Required free energy, as per classical nucleation theory, for the formation of a cluster of size i . Curves represent different constant values of supersaturation and temperature, illustrating the free energy barrier associated with the critical size.

This formalism is pertinent for analyzing solutes dissolved in liquids that nucleate in either liquid or crystalline states. However, CNT is not always successful, primarily because the capillarity approximation, upon which it is based, is a very primitive characterization of small molecular clusters. Nevertheless, the expressions derived provide intuitive value, suggesting that increasing the vapor supersaturation, S , accelerates the nucleation of droplets, all other parameters being constant. Additionally, the nucleation rate is influenced by the surface tension of the condensed phase: higher surface tension, γ_∞ , results in a slower rate. The rate is also quite sensitive to supersaturation, surface tension, and temperature, as these quantities appear inside an exponential function [31].

To surpass the predictive capability of classical theory, it is necessary to compute the partition functions of clusters of various sizes and develop a more realistic model of the excess free energy; however, this is beyond the scope of this work.

Another formalism that may be useful for this study involves the definition of the driving force commonly used in the phase transition between melts and crystalline phases. Consider a single-component liquid initially at equilibrium, quenched to a temperature T , below its melting temperature T_m . Since the liquid and solid phases have the same composition, the nucleation free energy corresponds to the free energy difference between the liquid and solid states at temperature T , in other words, the driving force is a function that depends on the undercooling rate [27, 32]:

$$\Delta\mu = \frac{\Delta H_m}{T_m}(T_m - T) + \int_T^{T_m} \Delta C_p dT' - T \int_T^{T_m} \frac{\Delta C_p}{T'} dT', \quad (8)$$

where ΔH_m and T_m are the molar heat of melting and the melting temperature of the crystal, respectively, and $\Delta C_p = C_p^l - C_p^c$ is the difference between the molar heat capacities of liquid and crystal at constant pressure. The experimental values of ΔG_V are normally bounded by the approximations usually assigned to Turnbull and Hoffman that assume $\Delta C_p = 0$ and $\Delta C_p = \text{constant}$, respectively:

$$\Delta\mu(T) = \frac{\Delta H_m}{N_A} \left(1 - \frac{T}{T_m} \right), \quad (9)$$

$$\Delta\mu(T) = \frac{\Delta H_m}{N_A} \left(1 - \frac{T}{T_m} \right) \frac{T}{T_m}, \quad (10)$$

Here, ΔH_m is the melting enthalpy per mole of the crystal and N_A is Avogadro's number. When the undercooling is large, the expression may not be precise enough. One can then consider the next term in the Taylor expansion leading to the Turnbull and Hoffman equations respectively [27]:

$$\Delta\mu(T) = \frac{\Delta H_m}{N_A} \left(1 - \frac{T}{T_m} \right) - \Delta C_p \left(\frac{(T - T_m)^2}{2T_m} \right), \quad (11)$$

$$\Delta\mu(T) = \frac{\Delta H_m}{N_A} \left(1 - \frac{T}{T_m} \right) \frac{T}{T_m} - \Delta C_p \left(\frac{(T - T_m)^2}{2T_m} \right). \quad (12)$$

This formalism is widely used in the study of the nucleation of impurities in metallic melts, with a wide range of materials, such as metallic glasses like $\text{Li}_2\text{O}_2\text{SiO}_2$ and LS_2 , or other metallic alloys like $\text{Ge}_2\text{Sb}_2\text{Te}_5$ and (Ag,In)-doped Sb_2Te (AIST) [26, 33, 34, 35, 36, 30].

Using these models to describe the driving force, they exhibit certain limitations. Firstly, within the formalism derived from the degree of saturation, an ideal mixture is assumed. This is evident since concentrations or mole fractions are used to determine the degree of supersaturation rather than activities. To rigorously work through activities, the driving force can be determined if the interaction parameters between the components of the solution are known [37], or determine the mixing parameters starting from the partition function derived from the grand canonical potential, employing the quasi-chemical approximation formulation [38] or exponential models [39].

In the second formulation, which utilizes the undercooling rate to determine the driving force, the approach is widely recognized and accepted. However, this formula encounters limitations when applied to mixtures exhibiting degrees of immiscibility. Specifically, the challenge arises in scenarios where two phases coexist, such as in solid-liquid equilibrium. In these instances, given a particular composition for which a certain temperature allows both phases to be in equilibrium; this temperature is referred to as the liquidus temperature T_l .

The standard application of this formulation presents issues as it traditionally employs the absolute melting point to determine the driving force, neglecting the presence of different phases that may manifest within the system.

A potential rectification for this oversight involves the utilization of the T_l instead of T_m . However, this correction is not without its challenges. Specifically, when the fraction of one of the phases is exceedingly low, accurately determining the liquidus temperature within the phase diagram becomes problematic. This difficulty is compounded by the typical unavailability of high-resolution phase diagrams.

Ideally, the driving force in phase transition studies is determined by a comprehensive thermodynamic model that includes information about the elements present in the system, as demonstrated in previous works [40, 41]. However, due to the limitations previously stated, an alternative formulation for the driving force has been developed to provide a more accurate description of the volumetric free energy. This method involves calculating the Gibbs free energy change, ΔG , defined by the free energy expressions for the liquid (l) and solid (s) phases.

The chemical potential for component A in the liquid phase, μ_A^l , is determined by constructing a tangent to the liquid free energy curve at the composition x_l . The point where this tangent line intersects the $x_A = 1$ axis defines μ_A^l . Similarly, the chemical potential for component A in the solid phase, μ_A^s , is identified at the intersection of the tangent line with the $x_A = 0$ axis.

At the liquidus temperature T_l , the free energy curves for both the liquid and solid phases are tangent to the line constructed from the previous step. The solid composition that is in equilibrium with the liquid composition x_l at T_l is given by the tangent point on the Gibbs free energy curve. This equilibrium composition is denoted as $x_{s,eq}$ and can be identified on the equilibrium phase diagram.

At a temperature T , arbitrarily lower than T_l , the chemical potentials in the solid, μ_A^s and μ_B^s , and for the liquid, μ_A^l and μ_B^l , are determined as before for the liquid phase. The differences in chemical potential, which drive the phase transition, are defined as follows:

$$\Delta\mu_A = \mu_A^l - \mu_A^s \quad (13)$$

$$\Delta\mu_B = \mu_B^l - \mu_B^s. \quad (14)$$

The free energy change, per unit volume, associated with forming a small amount of solid of composition x_s^* out of the liquid is given by

$$\Delta G_v = [x_s^* \Delta\mu_A + (1 - x_s^*) \Delta\mu_B] / V \quad (15)$$

where V is the average molar volume of the solid, assumed here to vary linearly between the molar volumes V^A and V^B of the pure solid systems:

$$V = x_s^* V^A + (1 - x_s^*) V^B. \quad (16)$$

The solid composition that is most likely to nucleate, x_n , is assumed to be the one with the largest difference in free energy, ΔG_v , between the liquid and solid state. This intuitively obvious assumption is used because of its simplicity. Further justification based on a more rigorous calculation is given in Appendix I. It can be seen from that ΔG_v is maximized if $\Delta\mu^A = \Delta\mu^B$, so that the composition x_n

corresponds to the point of tangency on the solid curve of a line parallel to the tangent to the liquid curve at x_l , so that

$$\Delta\bar{G}_v \approx \Delta\mu^A \approx \Delta\mu^B. \quad (17)$$

Therefore, given the composition dependence of the liquid and solid free energies, one can calculate the solid nucleus composition and the free energy of formation for the nucleus as a function of initial liquid composition, x_l , and undercooling $\Delta T = T_l - T$.

For an actual calculation of ΔG_p , it is necessary to use solution models. Therefore, regular solution behavior is assumed for the liquid phase so that

$$\mu_l^A = \mu_l^{A,0} + RT \ln(x_l^A) + \alpha_l(x_l^A), \quad (18)$$

$$\mu_l^B = \mu_l^{B,0} + RT \ln(x_l^B) + \alpha_l(x_l^B). \quad (19)$$

The solid phase is assumed to be a dilute or ideal solution so that α_s^A and α_s^B are independent of composition:

$$\mu_s^A = \mu_s^{A,0} + RT \ln(x_s^A) + \alpha_s^A, \quad (20)$$

$$\mu_s^B = \mu_s^{B,0} + RT \ln(x_s^B) + \alpha_s^B. \quad (21)$$

Combining equations (18) and (20) gives

$$\Delta\mu^A = (\mu_l^A - \mu_s^A) + RT \ln\left(\frac{x_l^A}{x_s^A}\right) + \alpha_l(x_l^A) - \alpha_s^A. \quad (22)$$

For pure metals, it can be assumed that the difference between the heat capacities of the solid and liquid, ΔC_p , is small, so that

$$\mu_l^{A,0} - \mu_s^{A,0} \approx \Delta S_f(T_m^A - T), \quad (23)$$

where ΔS_f and T_m^A are, respectively, the entropy of fusion and the melting temperature of pure A. Therefore, combining equations (22) and (23) gives

$$\Delta\mu^A = T \left[R \ln\left(\frac{x_l^A}{x_s^A}\right) - \Delta S_f \right] + \alpha'_l(x_l^A), \quad (24)$$

where

$$\alpha'_l(x_l^A) = \alpha_l(x_l^A) - \alpha_s^A + \Delta H_f. \quad (25)$$

Similarly, for component B

$$\Delta\mu^B = T \left[R \ln\left(\frac{x_l^B}{x_s^B}\right) - \Delta S_f \right] + \alpha'_l(x_l^B). \quad (26)$$

Now recall that at $T = T_l$, $\Delta\mu^A = 0$ so that

$$\alpha'(x_l^A) = -T_l \left[R \ln \left(\frac{x_l^A}{x_{s,eq}^A} \right) - \Delta S_f^A \right]. \quad (27)$$

For a given x_l^A , T_l , and $x_{s,eq}^A$ can be found from the equilibrium phase diagram. Combining equations (24) and (27) and rearranging terms gives

$$\Delta\mu^A = (T_l - T) \Delta S_f^A + RT \ln \left(\frac{x_l^A}{x_s^A} \right) - RT_l \ln \left(\frac{x_l^A}{x_{s,eq}^A} \right). \quad (28)$$

Similarly, for component B

$$\Delta\mu^B = (T_l - T) \Delta S_f^B + RT \ln \left(\frac{x_l^B}{x_s^B} \right) - RT_l \ln \left(\frac{x_l^B}{x_{s,eq}^B} \right). \quad (29)$$

Finally, as discussed previously, at $T < T_l$, the free energy change on nucleation is

$$V\Delta G_v = \Delta\mu^A = \Delta\mu^B. \quad (30)$$

Also, since $\Delta\mu^A = \Delta\mu^B$, from equations (28) and (29)

$$(T_l - T)(\Delta S_f^A - \Delta S_f^B) + RT \ln \left(\frac{x_l^A(1 - x_s^A)}{x_{s,eq}^A(1 - x_l^A)} \right) = RT \ln \left(\frac{x_l^A(1 - x_{s,eq}^A)}{x_{s,eq}^A(1 - x_l^A)} \right). \quad (31)$$

Therefore, given x_l , ΔS_f^A , ΔS_f^B , and the equilibrium phase diagram, one can find ΔG , and x_n at an arbitrary temperature T from equations (28)–(31). In the limiting case that the solubility of B in crystalline A is zero, the derivation simplifies considerably. Equation (18) still holds but equation (20) becomes $\mu_s^A = \mu_{s,0}^A$. Therefore, as before

$$\Delta\mu^A = T(R \ln x_l^A - \Delta S_f^A) + \alpha'(x_l^A) \quad (32)$$

and since $\Delta\mu^A = 0$, at T_l ,

$$\alpha'(x_l^A) = -T_l(R \ln x_l^A - \Delta S_f^A) \quad (33)$$

so that

$$V\Delta G_v = \Delta\mu^A = (T_l - T)(\Delta S_f^A - R \ln x_l^A). \quad (34)$$

An analogous equation holds for crystallization of pure B. This simplified result is particularly useful for metal-metalloid glass forming alloys such as Au–Si where the equilibrium solid solubility of the metalloid in the crystalline metal is very low.

8.1.2 Surface energy

As discussed in the previous section, surface energy is one of the critical parameters in CNT. Firstly, because this theory fails to predict the behaviour of small clusters and at the same time assumes a surface

energy value for a flat surface. In addition, the dependence of the surface energy on the nucleation rate is probably the most important part of this formalism.

Because this parameter is an exponential in the calculation of the nucleation rate, it depends very strongly on the value of the surface tension. For example, a change in γ_∞ of only one order of magnitude leads to a change in the nucleation rate of about eight orders of magnitude [42].

Nonetheless, a dependable method for measuring surface tension is absent, with the exception of aligning experimental nucleation rate data with theoretical models [43]. Furthermore, a critical hypothesis of the CNT, referred to as the capillarity approximation, overlooks the influence of curvature and size on surface tension [44]. Therefore, ideally it has to be obtained from experiments or from ab-initio calculations [45, 46, 47, 48, 49]. Another well-accepted methodology is from the complete thermodynamic model of the mixture, using Buttler's formulation [50, 51, 52], the problem with this methodology arises in having all the information and having a detailed phase diagram.

Given the difficulties noted above in measuring or simulating the surface free energy of the liquid-solid interface, the natural question is whether theoretical methods can predict its magnitude and the physical processes that affect it. Theoretical methods can predict its magnitude and the physical processes that affect it.

In order to determine γ , it is useful to discuss the energetic and entropic components that make it up, since, as we shall see, the different models that have been developed differ markedly in the relative contributions they attribute to these two components. The surface Gibbs free energy can be written as

$$\gamma = E^{(s)} - TS^{(s)} + PV^{(s)} \quad (35)$$

In this context, $E^{(s)}$ represents the energy excess at the surface, $S^{(s)}$ denotes the entropy at the surface, and $V^{(s)}$ is the additional volume. The latter term remains negligible unless under conditions of high pressure, and can be completely negated by appropriately selecting the Gibbs dividing surface such that $V^{(s)}$ becomes zero. This results in only energetic and entropic elements contributing to γ .

An early and widely adopted model for assessing the free energy at the liquid-solid interface was introduced by [53]. This model presupposes complete wetting of the crystal by the liquid, leading to a contact angle θ of zero in the equilibrium involving three phases: crystal, liquid, and vapor. Following from Eq. 35, with θ set to zero and consequently $\cos\theta$ equal to one, the derived expression is

$$\gamma_{sl} = \gamma_{sv} - \gamma_{lv} \quad (36)$$

Assuming the general case holds, the analysis simplifies to evaluating γ_{sv} and γ_{lv} independently. This method involves deducing the energy difference due to bond disruption between the solid-vapor and liquid-vapor phases, incorporating the solid's fusion enthalpy and melting-induced volume change, alongside a modest entropic variation from the external layers of both phases. Consequently, the derived formula is

$$\gamma_{sl} = \frac{\Delta H}{4fN_A v^{2/3}} + \frac{2\Delta V}{3V_s} \gamma_{lv} + \frac{T_m(\Delta S_l - \Delta S_s)}{fN_A v^{2/3}} \quad (37)$$

where f is a factor that relates the area A of a mole of surface atoms to the volume of a mole of atoms in the bulk solid through

$$A = f N_A v^{2/3} \quad (38)$$

Numerically, the factor stands at 1.12 for the bcc (110) surface and 1.09 for the fcc (111) surface. Given the minimal entropic contribution in Eq. 36, this framework primarily emphasizes energy aspects. Predominantly, the initial term, hinting at a direct relationship between γ_{sl} and $\Delta H/v^{2/3}$, aligns with empirical findings from initial nucleation studies, underpinning classical homogeneous nucleation theory.

In [54] introduced an energy-centric model for surface free energy, emphasizing electron-ion interactions and significant volume changes upon melting. Conversely, Turnbull proposed an entropy-focused model, envisioning the solid as a plane intersecting the liquid.

$$\gamma_{sl} = \frac{T_m \Delta S}{2f N_A v^{2/3}} - \frac{\Delta H}{2f N_A v^{2/3}} \quad (39)$$

More recent approaches have applied physical or computational simulations, notably using hard sphere packings, to gauge surface free energy, as detailed by [55]. In these models, spheres form a densely packed crystalline structure, excluding octahedral voids to mirror the dense liquid's random packing. Preference is given to tetrahedral gaps, aiming to enhance interfacial layer density. After assessing the configurational entropy across different surface arrangements, findings indicated no significant density reduction at the interface compared to the dense, random liquid structure. This suggests a minimal energetic impact if hard spheres mimic atoms with attractive forces, thus classifying the model as predominantly entropic and forecasting minor energy contributions to γ_{sl} .

$$\gamma = \frac{\alpha_m \Delta S_f}{N_A v^{2/3}} T \quad (40)$$

where α_m is 0.86 for the fcc (111) or hcp (0001) surfaces, and 0.71 for the bcc (110) surface. At $T = T_m$, this has the same form as the empirical equation with γ proportional to $\Delta H/v^{2/3}$.

Up to now we discussed almost exclusively the case of one-component substances. There is considerable interest, in the nucleation of binary mixtures or alloys. Calculations in this case require a knowledge of the bulk thermodynamics of the mixtures (both liquid and solid).

In [56] extended the theory of [55] to binary alloys. They use Eq. 40

$$\gamma = \frac{\alpha_m \Delta S_f}{N_A v^{2/3}} T \quad (41)$$

and take v to change linearly with mole fraction between its values for the two pure components. In the same way they take

$$\Delta S_f = x_s^A \Delta S_f^A + (1 - x_s^A) \Delta S_f^B \quad (42)$$

where x_s^A is the mole fraction of A in the solid and ΔS_f^A and ΔS_f^B are the entropies of fusion of the two separate components.

This last equation is simple and useful as a starting point to obtain the surface energy for each

impurity.

8.2 Kinetic theory

Understanding the nucleation rate necessitates analyzing the dynamics of cluster size evolution. This is addressed within the framework of the classical nucleation theory, also identified as the phenomenological or Becker-Döring-Zeldovich (BDZ) theory, which is used to our analysis. Define $N_n(t)$ as the average quantity of clusters containing i molecules at an instance t . It is assumed that the interaction between clusters are neglected. As a result, alterations in the size of the clusters are only attributed to the mechanisms of evaporation and condensation, signifying that a cluster containing i molecules may either enlarge by acquiring another molecule or diminish through the release of one. Such is the fundamental postulate of the classical nucleation theory. Consequently, the variation in the count of clusters of a particular size is governed by what is known as the master equation [20].

$$\frac{\partial N_i(t)}{\partial t} = J_i - J_{i-1}, \quad (43)$$

where

$$J_i = g_{i+1}^+ N_{i+1}(t) - g_i^- N_i(t) \quad (44)$$

is a current in a size space, i.e., it is the rate at which clusters of size $i - 1$ grow to clusters of size i . Here g_{i+1}^+ is the rate of the molecule attachment to a cluster of size i , and g_i^- is the rate of detachment. According to the theory of thermodynamic fluctuations, the equilibrium distribution of clusters obeys the Boltzmann (or Gibbs) distribution

$$N_i^{\text{eq}} = N_0 \exp\left(-\frac{\Delta G_i}{k_B T}\right), \quad (45)$$

where ΔG_i is the minimum work needed to form a cluster of size i , k_B is Boltzmann's constant, T is the temperature, and N_0 is a pre-exponential factor.

At equilibrium the current J_i is zero, as this consequence only the forward rate needs to be specified to calculate the opposite rate.

$$g_{i+1}^+ N_{i+1}^{\text{eq}}(t) - g_i^- N_i^{\text{eq}}(t) = 0 \quad (46)$$

For crystal nucleation in melt or glass, the rate of attachment can be expressed as

$$g_{i-1}^+ = b D \lambda^{-2/3} i^{-2/3} \exp\left(-\frac{\Delta G_{i+1} - \Delta G_i}{2 k_B T}\right), \quad (47)$$

where $b = 24$ is a geometrical factor, D the diffusion coefficient, and λ the jump distance in the parent phase. The quantities we are mainly concerned with are the net formation rate of clusters of given size (observable size), and the number density of such clusters that exceed this size. The former can be expressed as

$$J_{i_0} = A_{i_0} N_{i_0} - D_{i_0+1} N_{i_0+1}, \quad (48)$$

where i_0 is the number of molecules in the cluster of “observable” size, while the latter is given by

$$N_{>i_0} = \sum_{i=i_0}^{\infty} N_i. \quad (49)$$

Owing to the finite maximum size one is able to handle in the computations, the evaluation of $N_{>i_0}$, is not without difficulties, and depends on the choice of the boundary conditions.

We set the following initial and boundary conditions. At $t = 0$, the cluster distribution is defined as $N_i = N_{\text{eq},i}$ for $i < u$, and $N_i = 0$ for $i \geq u$, where $u = 2$ unless specified otherwise. This scenario is interpreted as rapid cooling from high temperatures, where molecules predominantly exist in a monomeric state; that is, $N_1 = N_L \exp(-\Delta G_1/kT)$, with $\Delta G_1 = 0$, since monomers from the parent and new phases are indistinguishable. It is noted that most cluster models fail to accurately describe the smallest clusters, as evidenced by the non-zero ΔG_1 values they predict, leading to an unphysical number density for monomers. Consequently, setting $N_1 = N_L$ amounts to adjusting ΔG_i to $\Delta G_i - \Delta G_1$ (i.e., setting $\Delta G_1 = 0$), since only differences of the form $\Delta G_{i+1} - \Delta G_i$ are present in the rate coefficients [36].

In these studies, a “no-depletion” boundary condition maintains the monomer number density constant, $N_1(t) = N_{\text{eq},1}$, leading to an increase in system’s molecule count over time, which is an unphysical behavior. However, as demonstrated previously, this excess is negligible for the timescale of steady-state formation, provided that an absorbing boundary is set for the largest cluster, $N_{i_{\max}+1} = 0$. This condition unfortunately results in a nonzero flux of clusters out of the system, causing significant deviations in the truncated sum $\sum_{i=i_0}^{i_{\max}} N_i$ from the actual integrated formation rate J_{i_0} .

In this study, focusing on large cluster populations, we aim to validate numerical results by comparing $N_{>i_0}$ with $\int_0^{\infty} J_{i_0} dt$. Thus, we implement a unique upper boundary condition by setting both $A_{i_{\max}}$ and $D_{i_{\max}+1}$ to zero, effectively “closing” the system at i_{\max} . This ensures no flux between cluster sizes i_{\max} and $i_{\max} + 1$, maintaining the balance $N_{>i_0} = \int_0^{\infty} J_{i_0} dt$. However, this leads to an accumulation of clusters at i_{\max} due to these boundary conditions [36, 57].

This value, i_{\max} is equal to the number of equations which have to be solved simultaneously and is determined, therefore, by a balance between the critical number density and the available computer time [37]. To achieve this objective, a parametric code has been developed for the extraction of all thermodynamic data and for solving the system of master equations utilizing Python. However, for scenarios where the quantity of equations to be resolved is exceedingly large, an alternative version of the code has been implemented in Julia. This adaptation enhances both computational speed and memory efficiency for model resolution. In order to check that the code solves the model correctly, benchmarking has been proposed with the works of [26, 33, 34, 35, 36, 30] for $\text{Li}_2\text{O}_2\text{SiO}_2$. For this benchmark, the simulation is performed for a simplified set of physical properties of the lithium disilicate glass given in 8-1. In this case, the Gibbs molar free energy difference is calculated using the linear Turnbull approximation Eq. 9, while the calculations were performed at $T = 750\text{K}$.

In the following figures, comparisons between results from absorption and closing boundary conditions are presented. Utilizing ΔG_i from the uncorrected droplet model, maximum cluster sizes were set at $i_{\max} = 40$ and 100 , surpassing the critical size $i^* = 23$. In the Fig. 8-2, it can be seen that the

Table 8-1: Simplified set of physical properties of LS_2 .

Property	Symbol	Value
Molar mass	M	150.05 g
Mass density	ρ_m	2.5 g cm ⁻³
Jump distance	λ	4.6 Å
Interfacial free energy	γ_∞	150 mJ m ⁻²
Heat of fusion	ΔH_f	52 kJ mol ⁻¹
Melting temperature	T_f	1300 K
Arrhenius-coeffs. of diffusion:	D_0	$2 \times 10^{-9} \text{ m}^2\text{s}^{-1}$
	D_1	59 920.2 K

calculated driving force and the reference driving force are exactly the same, so we can be sure that the thermodynamics is defined in the same way.

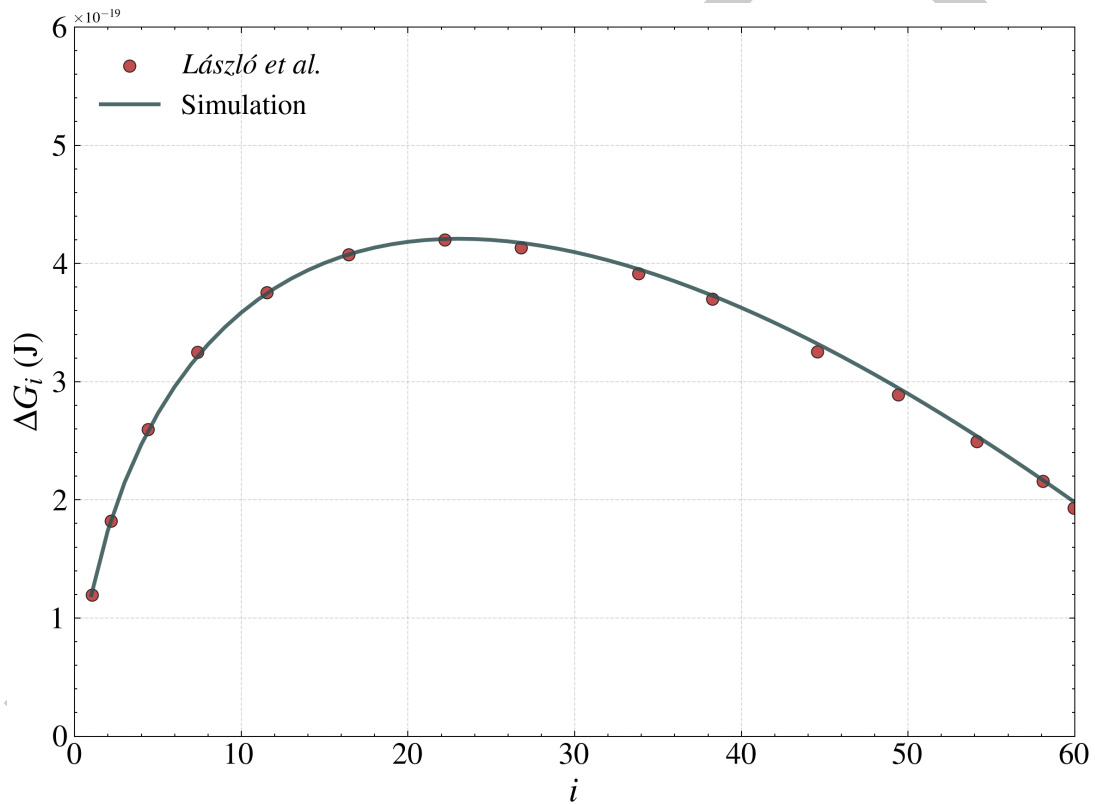


Figure 8-2: Simulation and reference size dependent free energy of clusters for the uncorrected classical droplet model, CNT.

In the case of the population distribution, the results obtained from the simulation are in perfect agreement with the reference results. We note the difference in the results depending on the upper boundary condition used. With the closed boundary condition the distribution is very close to the equilibrium distribution, for $i_{\max} = 40$, since for high i_{\max} the equilibrium distribution is not fulfilled for postcritical sizes, as can be seen for the case of $i_{\max} = 100$.

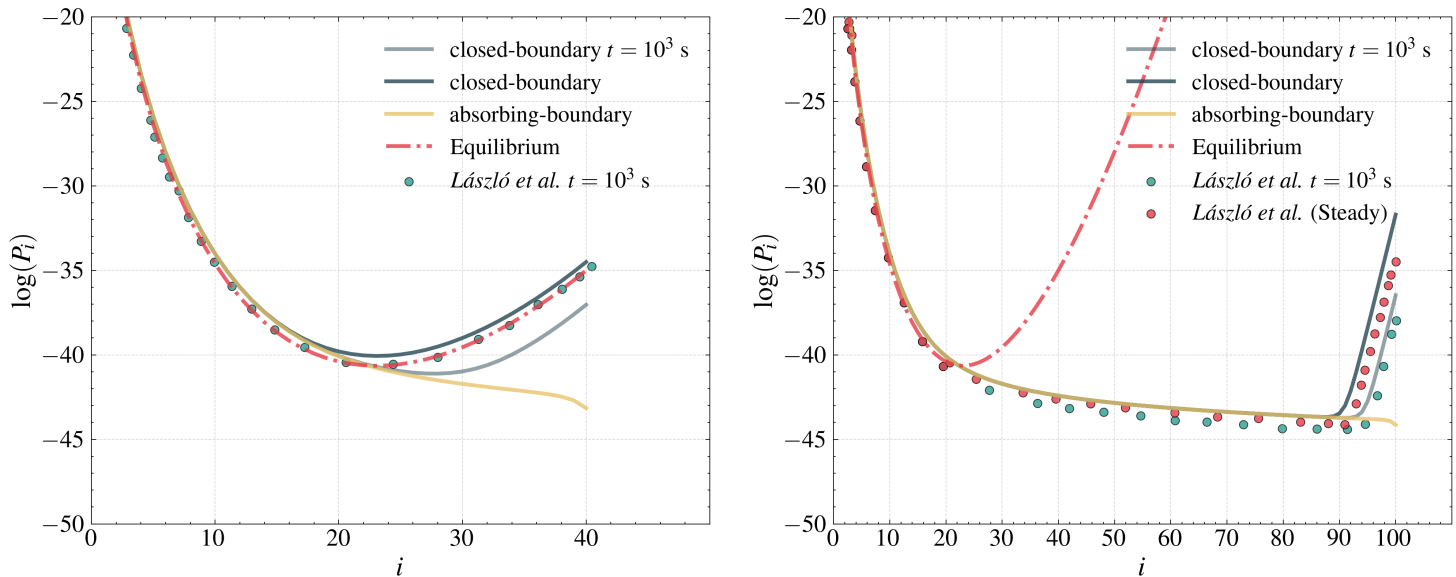


Figure 8-3: Effect of upper boundary condition comparison between simulation and reference cluster number density distribution for different sizes $i_{\max} = 40$ and 100 .

This analysis indicates that for extended times, the number densities of supercritical clusters, obtained by summing N_i and integrating the nucleation rate, match. In contrast, closing conditions lead to a peak in the nucleation rate before a steady state is reached, which is reflected in a drop to zero in later stages and a stabilization of the supercritical number densities. Similar qualitative results were achieved for $i_{\max} = 100$ as shown in Fig. 8-5, the steady state is reached under both boundary conditions. The variations emerge at larger cluster sizes and over extended durations. The accumulation at significant cluster dimensions affects the cluster population primarily near i_{\max} , marked by the exponential rise of N_i , requiring extensive computational efforts to achieve equilibrium for such nominal maximum sizes.

Due to the limitations of this study, where calculations are confined to $t = 10^5$ s required for reaching equilibrium at $i_{\max} = 40$, the outcomes using the closing boundary condition mirror those from the absorbing-state condition, aside from a trivial area near i_{\max} . Nonetheless, the equivalence of $N_{i>i_0} = \int_0^\infty J_{i_0} dt$ remains intact.

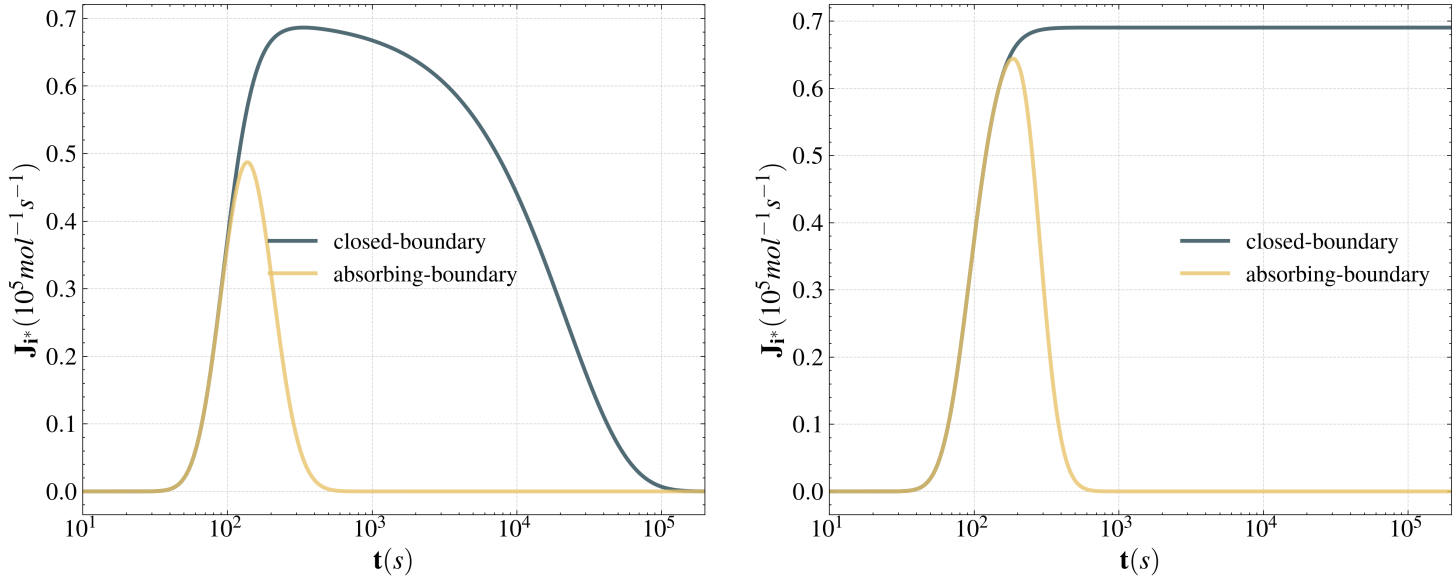


Figure 8-4: Effect of upper boundary condition comparison between simulation and reference postcritical nucleation rates for different sizes $i_{\max} = 40$ and 100.

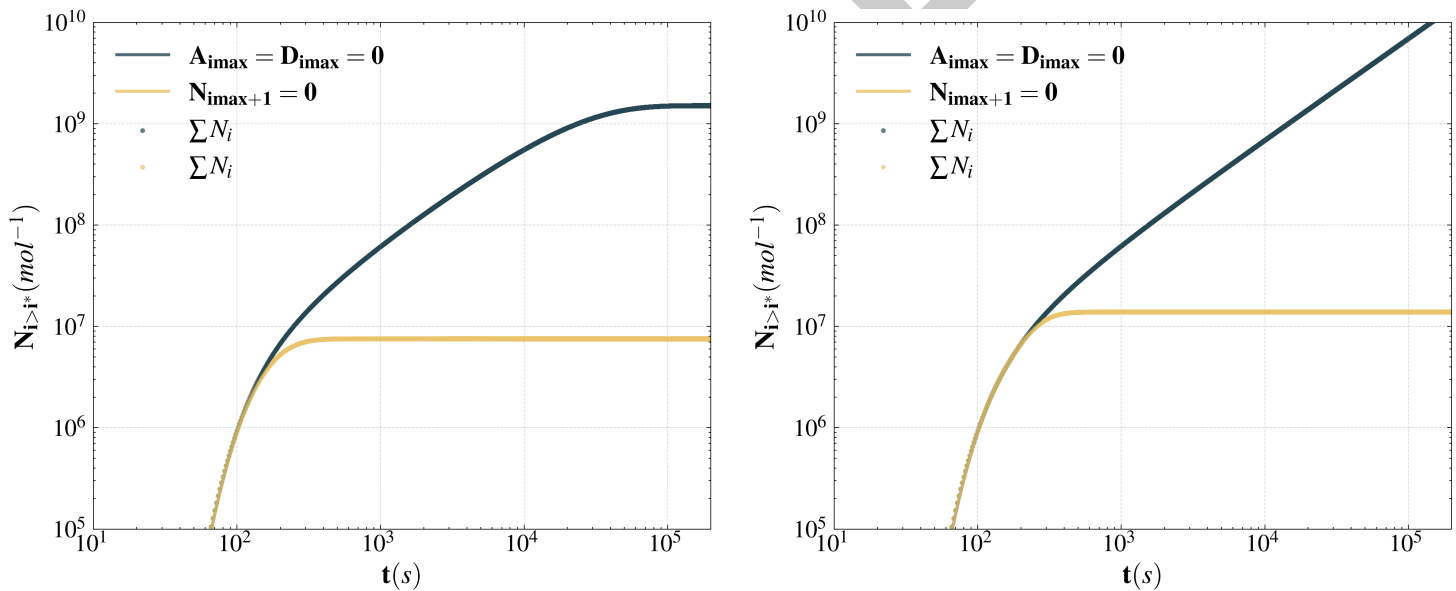


Figure 8-5: Effect of upper boundary condition comparison between simulation and reference postcritical total cluster number density for different sizes $i_{\max} = 40$ and 100.

To see the difference in nucleation rates for $i_{\max} = 40$ and 100 using different boundary conditions, the total nucleation rate for different molecule sizes is plotted. The figures are divided as follows, on the left are the results for $i_{\max} = 40$ using different upper boundary conditions, and on the right for $i_{\max} = 100$.

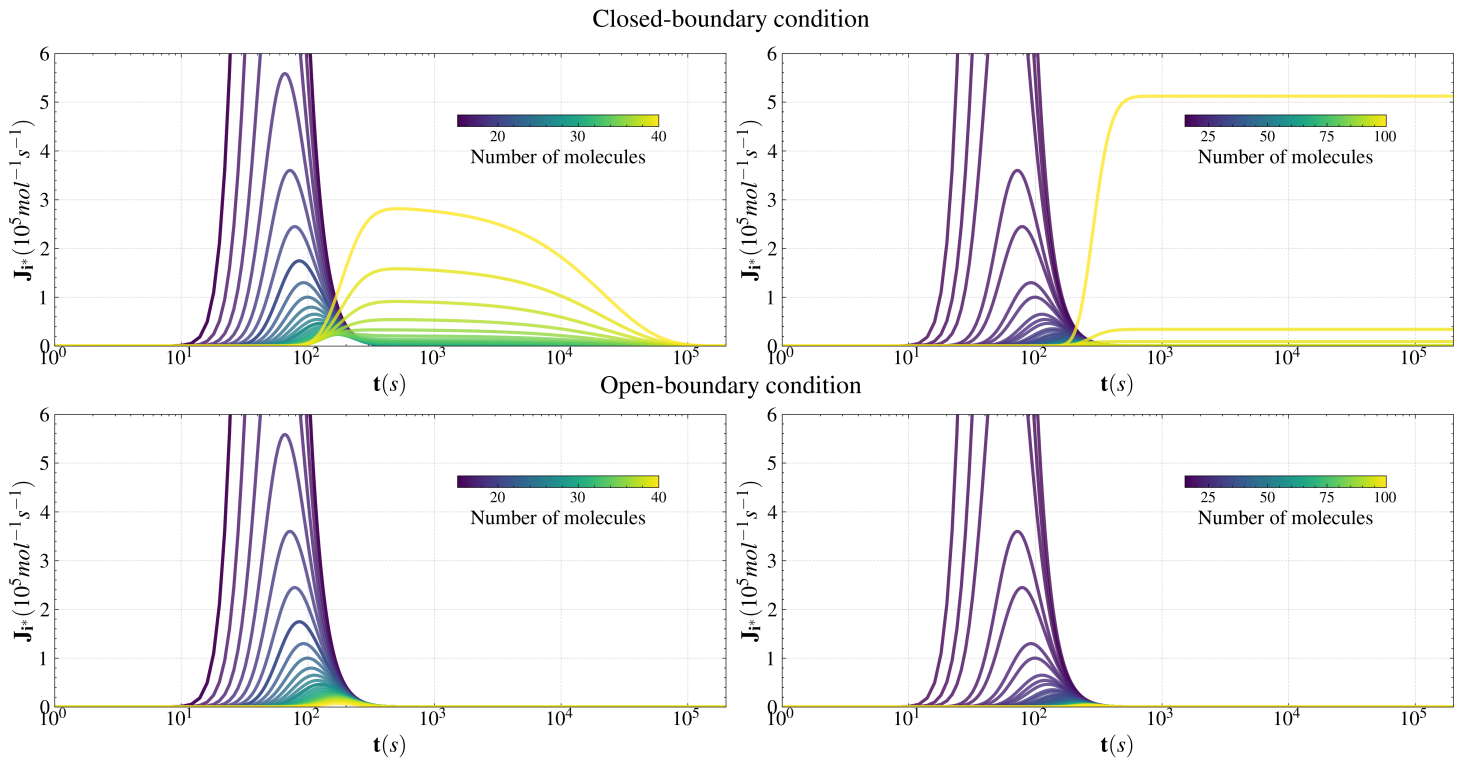


Figure 8-6: Nucleation rates for different observable sizes for closed- boundary (top) and open-boundary(bottom) for $i_{\max} = 40$ (left) and 100 (right).

The differences observed are primarily due to the boundary conditions, as previously mentioned. In scenarios with closed boundary conditions, there is an accumulation of large clusters, resulting in a higher nucleation rate compared to clusters of intermediate sizes.

Additionally, it has been noted that when the maximum cluster size i_{\max} increases, the behavior of the curve changes to an exponential form, maintaining a constant value at the steady state. This is in contrast to a maximum size of $i_{\max} = 40$, where the rate tends to zero, thereby mirroring the equilibrium distribution more closely.

From these observations, we can deduce that for smaller maximum sizes, the stationary population distribution aligns more closely with the equilibrium distribution. However, as the maximum size expands, the stationary distribution begins to diverge from the equilibrium state.

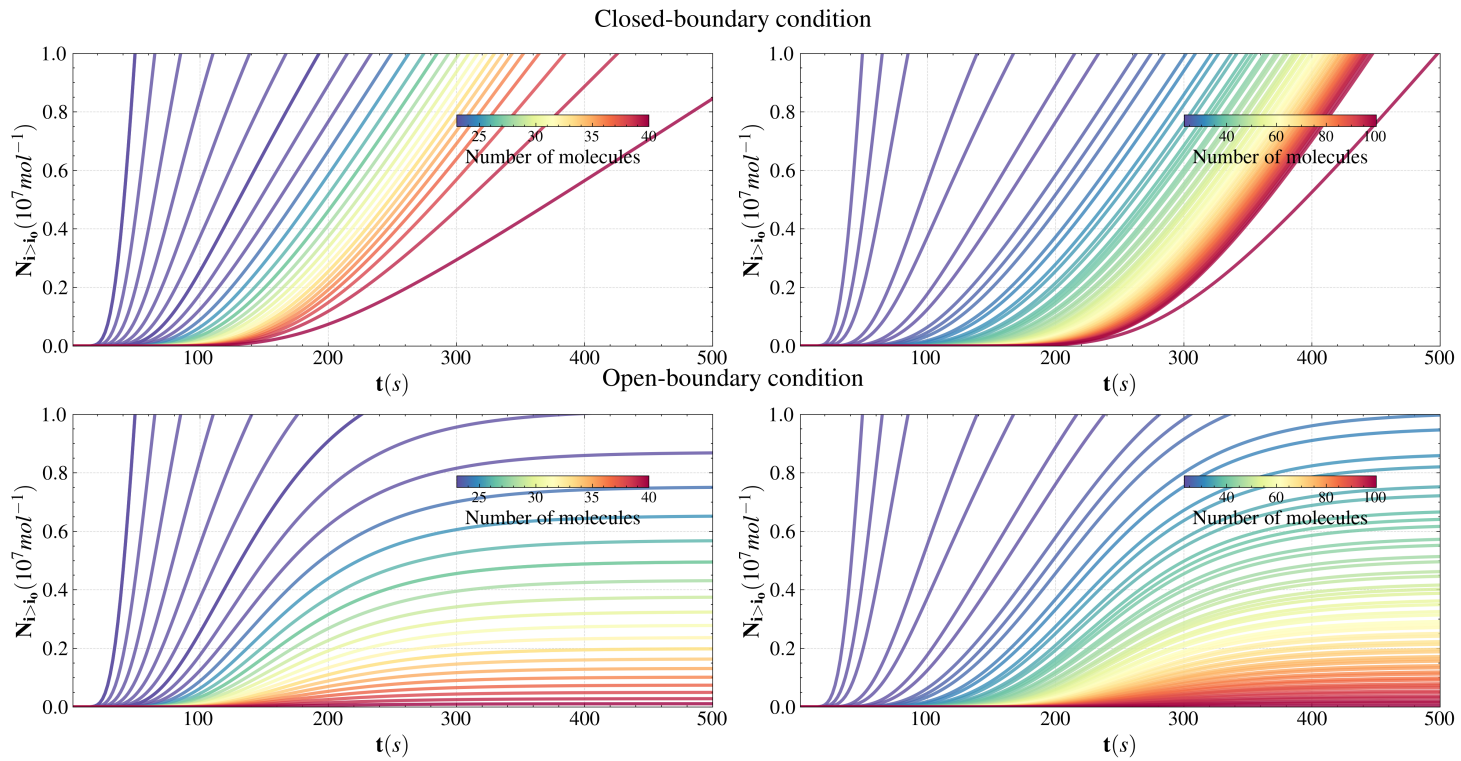


Figure 8-7: Total number density for different observable sizes for closed- boundary (top) and open-boundary(bottom) for $i_{\max} = 40$ (left) and 100 (right).

In the case of number density, for open boundary conditions, a steady state is reached more quickly than for closed conditions.

8.3 Impurities results

In this section we will summarise the thermodynamic parameters found for each impurity and the results obtained from simulation. The section is then divided into metallic and non-metallic impurities.

8.3.1 Metallic impurities

In this section the data and results for metallic impurities (Fe, Cr, AlN) are presented.

Fe

First of all, the most important thing to consider is which phases are present in the Li-Fe system at the temperature at which this fluid will be found. The phase diagram of the Fe-Li system is obtained from FactSage database [58], where also allows equilibrium calculations for some systems.

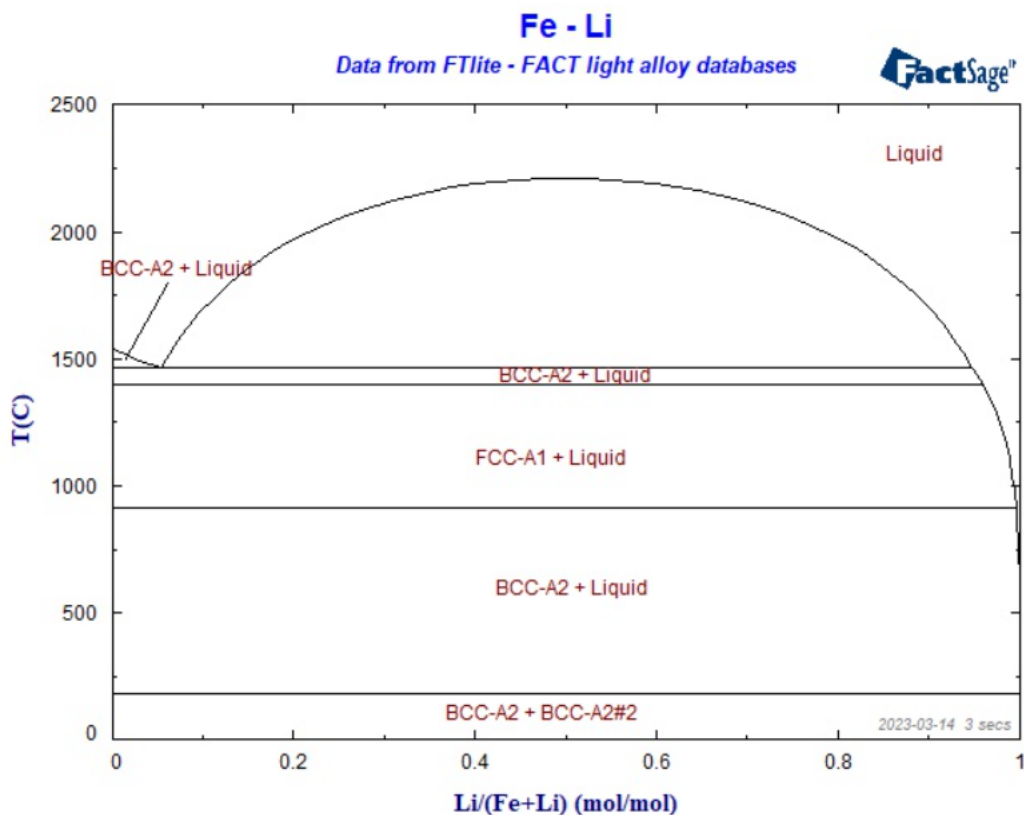


Figure 8-8: Phase diagram of Li-Fe mixture from FactSage database [58].

From [59] the solubility of Fe in Li is extracted ad different temperatures and then fitting the data. In the Fig. 8-9 the solubility of Fe in Li is shown.

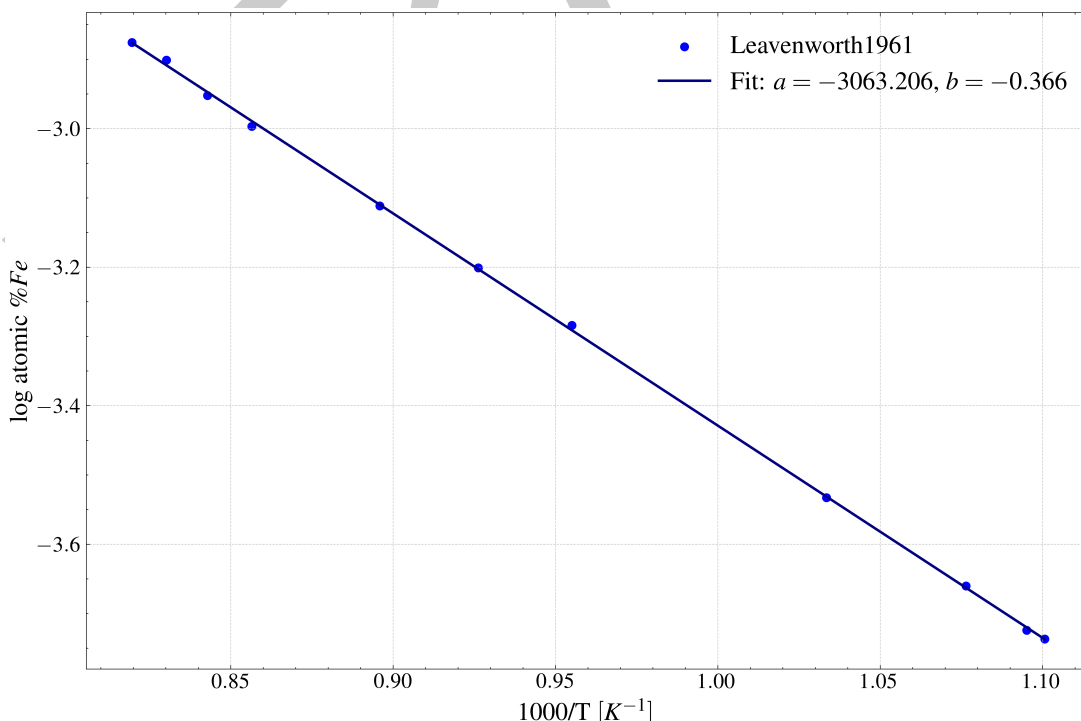


Figure 8-9: Fe solubility in liquid lithium dependence on temperature ??.

As previously mentioned, FactSage allows equilibrium calculations to be made for certain systems, in this case, for the Fe-Li system, it has been possible to calculate equilibrium compositions for the operating temperature and subsequently comparing the solubility of the reference with the calculated parameters.

	<i>Reference</i>	$x_{l,eq}^A$	$x_{s,eq}^A$
FactSage [58]		1.76×10^{-5}	1.00
Ref. [59]		1.12×10^{-5}	-

Table 8-2: Equilibrium compositions of iron using FactSage and reference data.

The findings closely match and share the same order of magnitude, indicating consistency in the values. In the table below, we display the balanced compositions calculated with FactSage for specific values: first, the initial values used, and then, those slightly increased.

Molar fractions (T = 668 K)			
Species	Amount/mol	Mole Fraction	Activity
Fe	1.6000×10^{-7}	1.6000×10^{-7}	1.3491×10^{-3}
Li	1.0000×10^0	1.0000×10^0	1.0000×10^0
PHASE: Liquid#1(#2)			
Species	Amount/mol	Mole Fraction	Activity
Fe	1.6000×10^{-7}	1.6000×10^{-7}	1.3491×10^{-3}
Li	1.0000×10^0	1.0000×10^0	1.0000×10^0
Total	1.0000×10^0	1.0000	1.0000
PHASE: BCC-A2#1			
Species	Amount/mol	Mole Fraction	Activity
Fe-alpha	0.0000×10^0	5.6693×10^{-16}	9.1079×10^{-3}
Li	0.0000×10^0	1.0000	7.7433×10^{-1}
Total	0.0000×10^0	1.0000	7.7433×10^{-1}

Table 8-3: Equilibrium compositions of iron using FactSage with an iron molar fraction used as input.

Molar fractions (T = 668 K)			
Species	Amount/mol	Mole Fraction	Activity
Fe	9.2880×10^{-5}		
Li	9.9991×10^{-1}		
PHASE: Liquid#1			
Species	Amount/mol	Mole Fraction	Activity
Fe	1.7601×10^{-5}	1.7603×10^{-5}	1.4813×10^{-1}
Li	9.9991×10^{-1}	9.9998×10^{-1}	9.9998×10^{-1}
Total	9.9992×10^{-1}	1.0000	1.0000
PHASE: BCC-A2#1			
Species	Amount/mol	Mole Fraction	Activity
Fe-alpha	7.5279×10^{-5}	1.0000	1.0000
Li	1.3112×10^{-18}	1.7418×10^{-14}	7.7432×10^{-1}
Total	7.5279×10^{-5}	1.0000	1.0000

Table 8-4: Equilibrium compositions of iron using FactSage with an iron molar fraction increased to $x_l^A = 9.2880 \times 10^{-5}$.

From these results, several conclusions can be drawn. Initially, it is evident that employing the assumed mole fraction as input results in the presence of only one liquid phase, thereby intersecting with the equilibrium state. This is a significant observation as it highlights the system's state under the given

conditions.

In an enhanced analysis, as illustrated by the second table, an increase in the mole fraction leads to the liquid phase reaching the equilibrium fraction of iron, equivalent to its solubility limit. Conversely, in the solid phase that subsequently forms, it is observed to be entirely composed of iron. This finding is critical as it suggests that, based on the mole fraction initially used for the input, iron is insoluble in lithium at the specified operating temperature.

Consequently, to determine the driving force, the formalism from Eq. 34 is used, considering that the solid fraction is entirely constituted by one of the mixture's elements. Similarly, for calculating the surface energy, the Eq. 41 is employed.

The following table provides a summary of the obtained and identified values, which are essential for calculating the size distribution of the clusters. The diffusivity of iron in liquid lithium has not been found, and therefore, the diffusivity of chromium in Pb-Li has been used for both iron and chromium [60].

Parameter	Symbol	Value (Unit)
Temperature	T	668 K
Molar Mass	M	55.85 g/mol
Mass Density	ρ	7.87 g/cm ³
Melting Point	T_m	1811 K
Heat of Fusion	ΔH_f	13.8 kJ/mol
Surface Tension	σ	0.11 J/m ²
Diffusion Coefficient	D	4×10^{-14} m ² /s

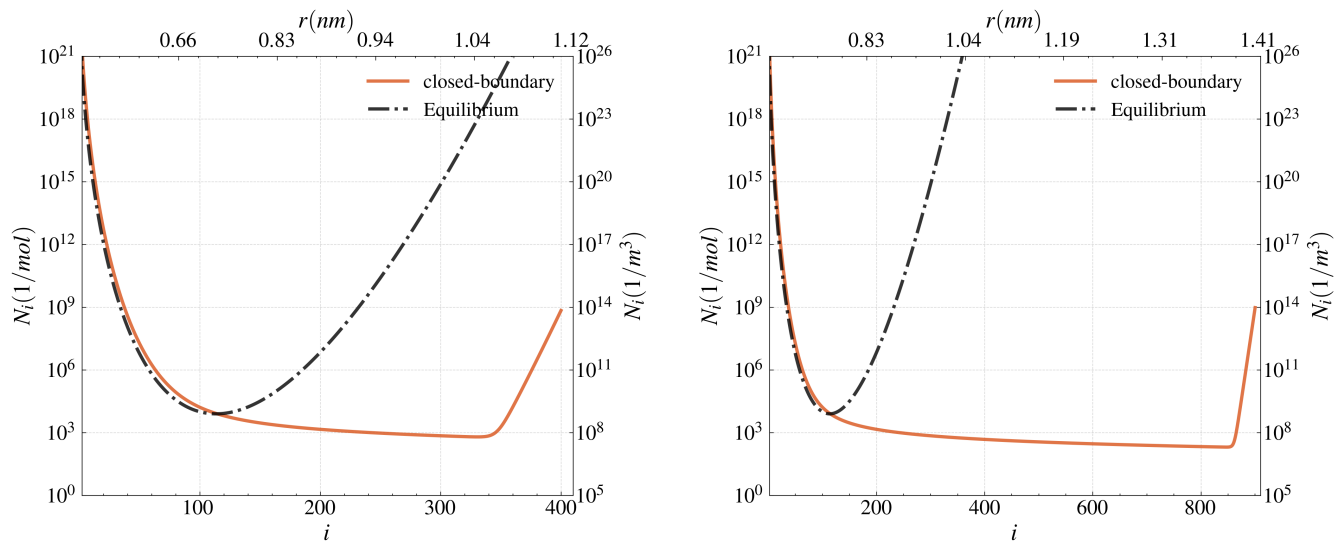
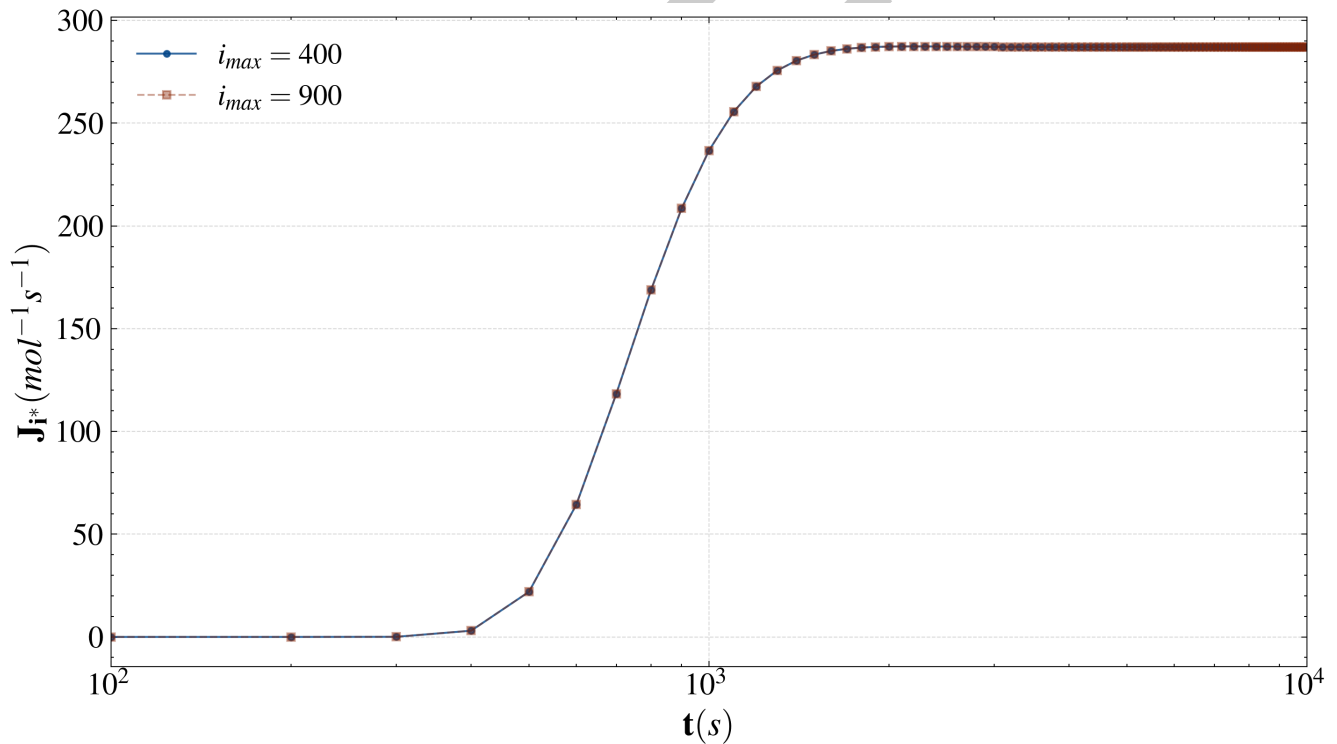
Table 8-5: Parameters for Fe

In Table. 8-6 the critical parameters are obtained.

Parameter	Symbol	Value (Unit)
Critical radius	r^*	0.35 nm
Energy barrier	ΔG^*	4.22×10^{-19} J
Critical number of molecules	n^*	114

Table 8-6: Critical values for Fe

To solve the system of kinetic equations and obtain the size distribution, we utilized the model described in the previous section. A closed boundary condition was selected for this purpose. Additionally, as a pre-exponential factor N_0 for the equilibrium distribution, the Avogadro number N_A was employed, consistent with methodologies used in prior benchmarking, ensuring that the results are expressed per mole. Furthermore, the jump rate λ has been defined as the cubic root of the solid's molecular volume. In this case, we have chosen to perform simulations with molecule sizes larger than $3 * n^*$, normally used in these kind of calculations. In the following graph we can see the size distribution for $i_{max} = 400$ and $i_{max} = 900$.

Figure 8-10: Iron cluster number density distribution for different sizes $i_{\max} = 400$ and 900 .Figure 8-11: Iron nucleation rates for different sizes $i_{\max} = 400$ and 900 .

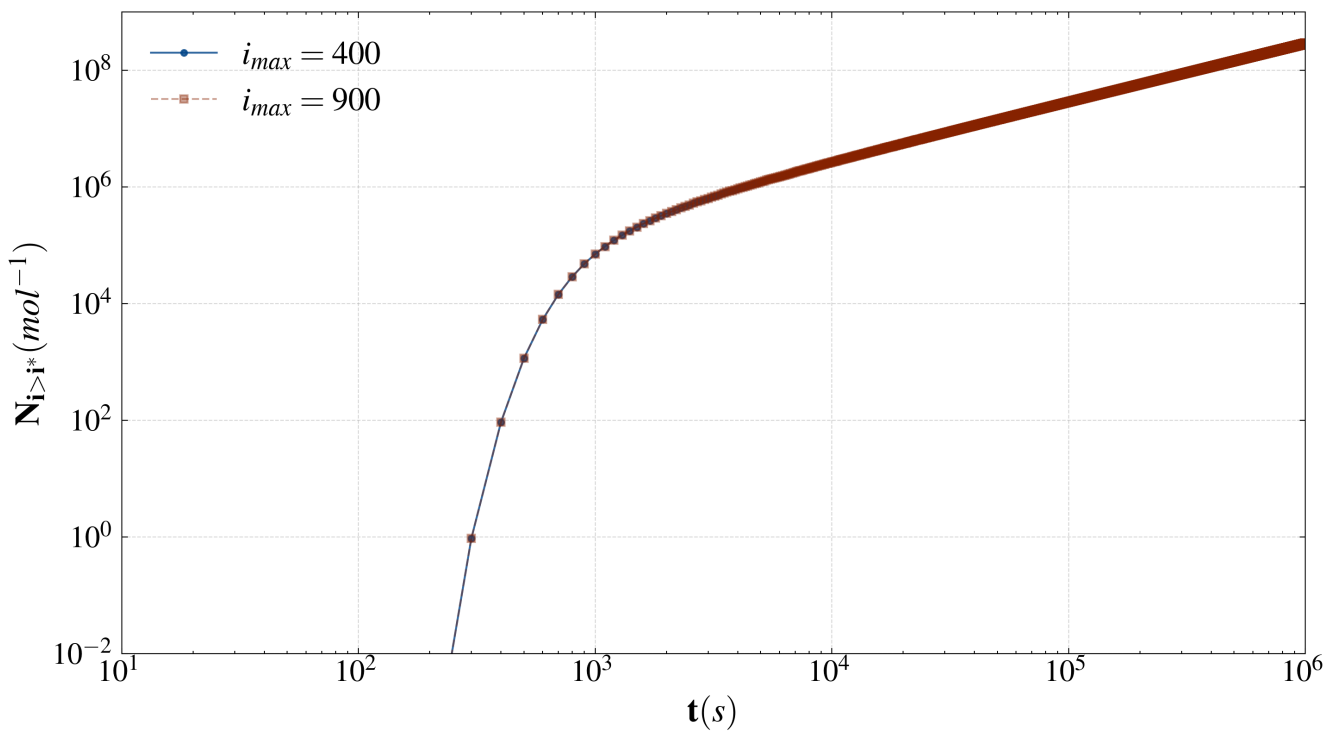


Figure 8-12: Iron postcritical total number density for different sizes $i_{\max} = 400$ and 900.

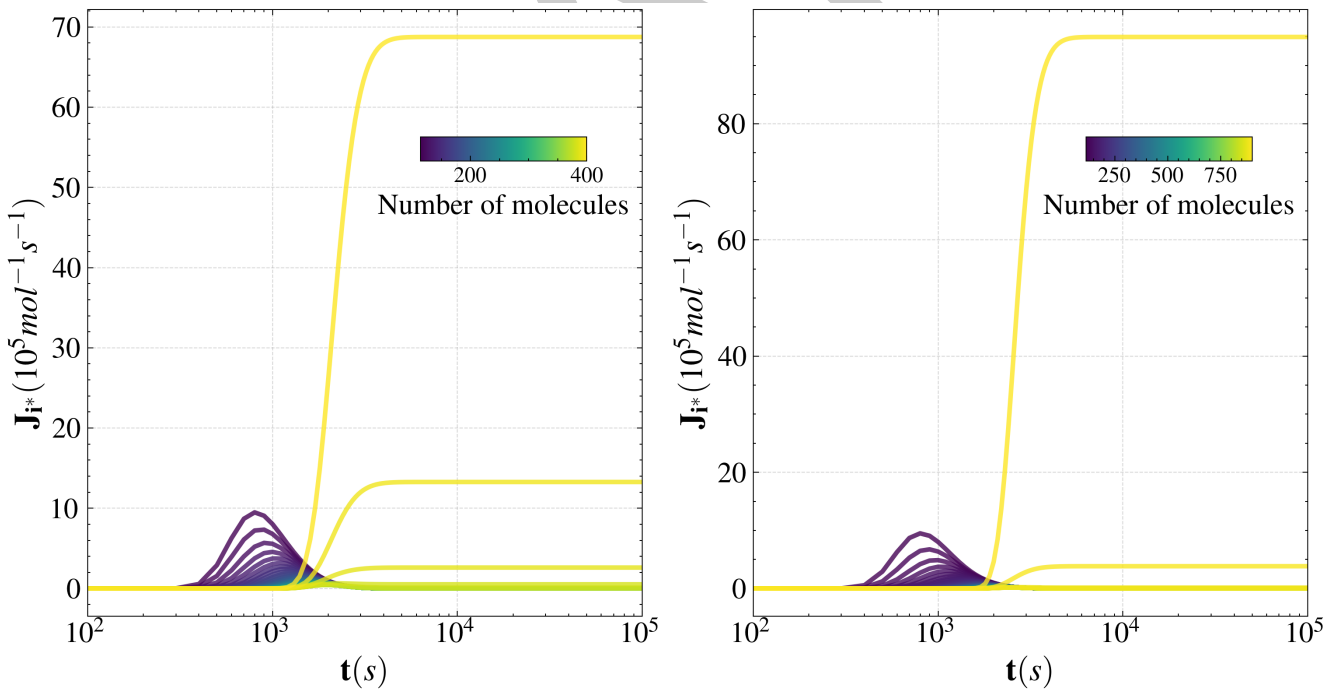


Figure 8-13: Iron nucleation rates for different observable sizes for $i_{\max} = 400$ (left) and 900 (right).

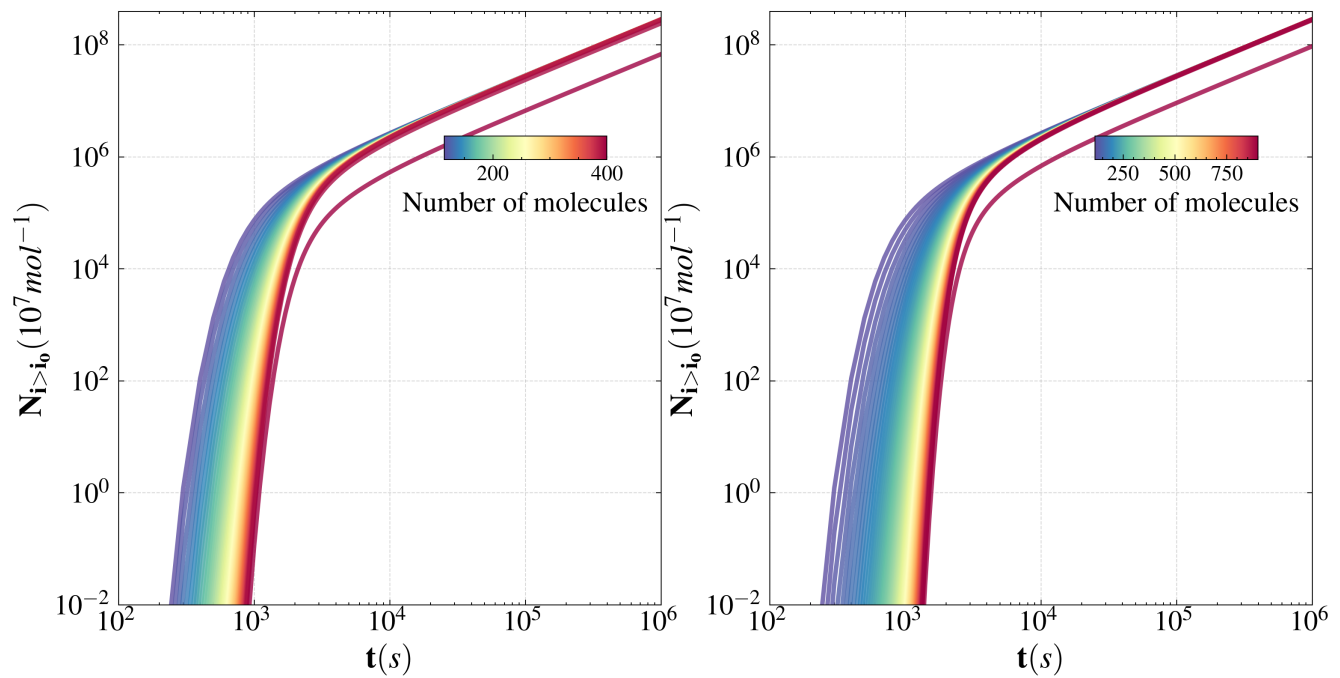


Figure 8-14: Iron postcritical total number density for different observable sizes for $i_{\max} = 400$ (left) and 900 (right).

Cr

The phase diagram of the Li-Cr system is shown below.

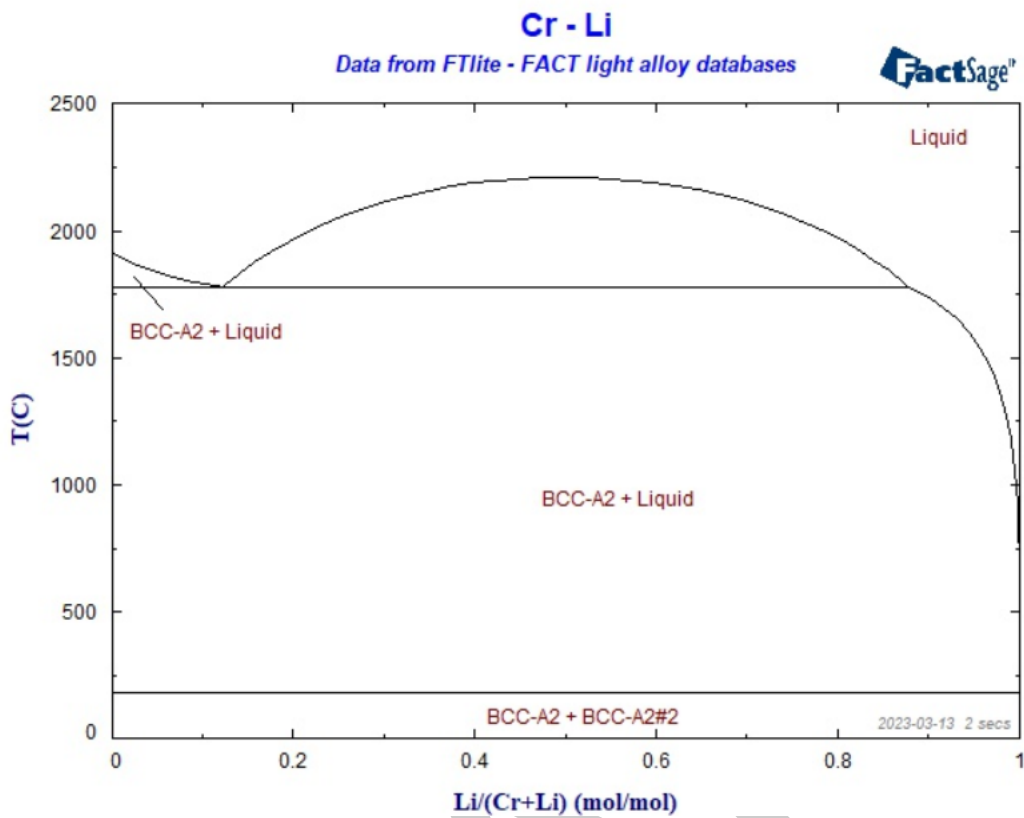


Figure 8-15: Phase diagram of Li-Cr mixture from FactSage database [58].

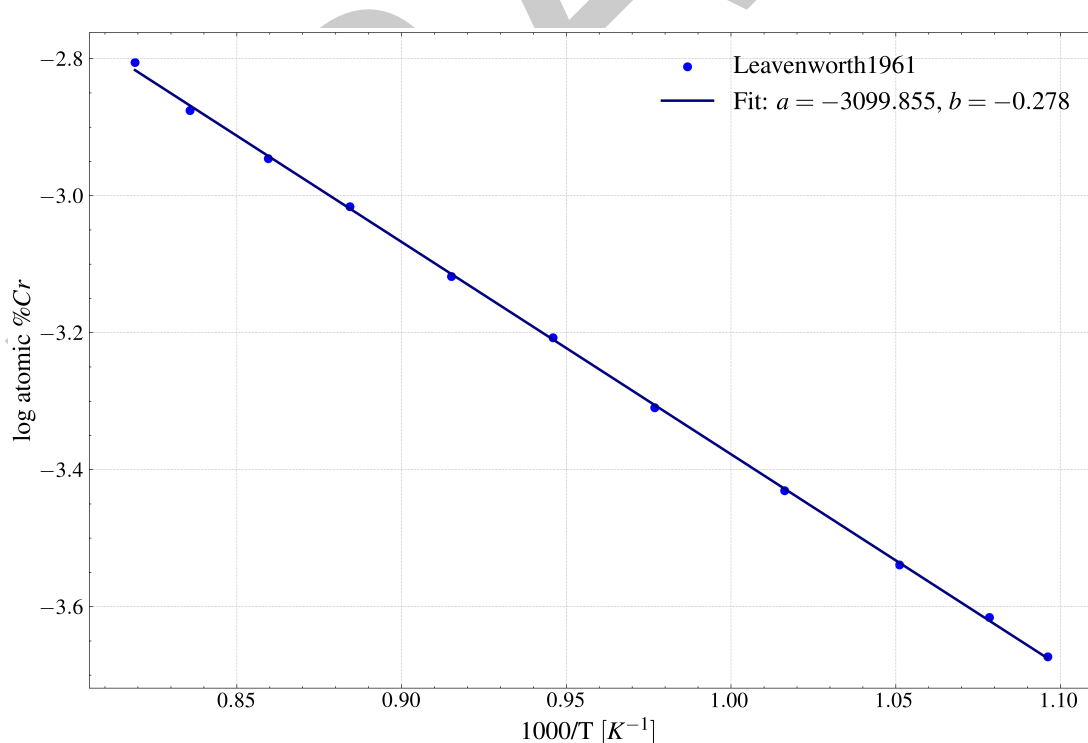


Figure 8-16: Cr solubility in liquid lithium dependence on temperature ??.

In Table. 8-11 the critical parameters are obtained.

In Fig. 8-29 the cluster population density is solved for two i_{max} , in this case smaller values than iron

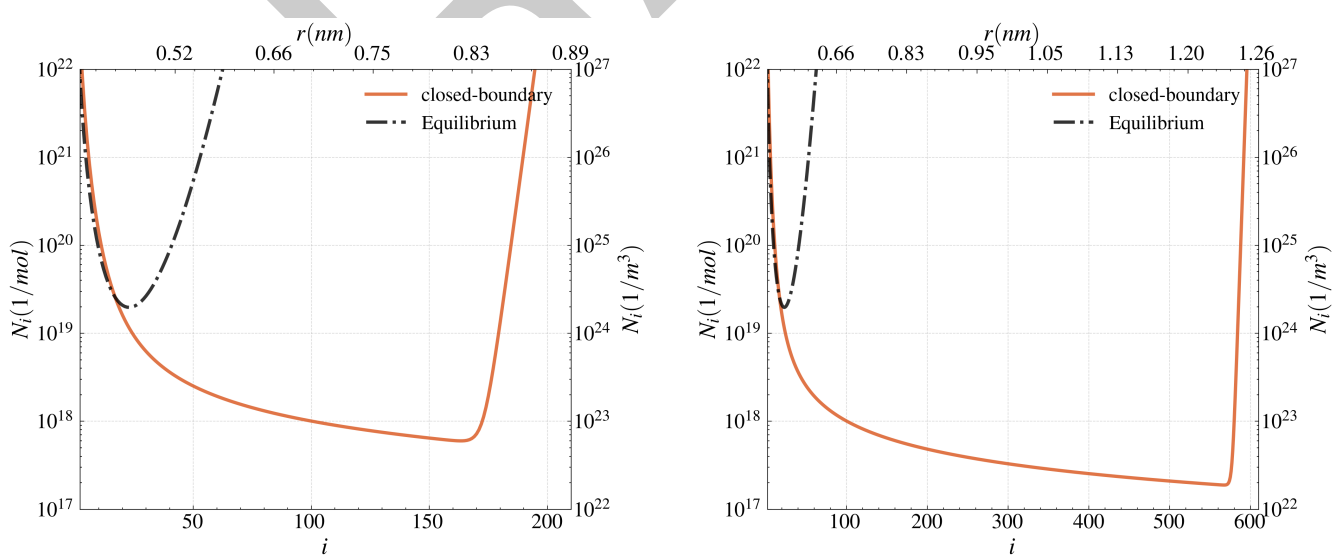
Reference	$x_{l,eq}^A$	$x_{s,eq}^A$
FactSage [58]	5.86×10^{-6}	1.00
Ref. [59]	1.21×10^{-5}	-

Table 8-7: Equilibrium compositions of iron using FactSage and reference data.

Molar fractions (T = 668 K)			
Species	Amount/mol		
Cr	2.0000×10^{-8}		
Li	1.0000×10^0		
PHASE: Liquid#1(#2)			
Species	Amount/mol	Mole Fraction	Activity
Cr	2.0000×10^{-8}	2.0000×10^{-8}	1.6853×10^{-4}
Li	1.0000×10^0	1.0000×10^0	1.0000×10^0
Total	1.0000×10^0	1.0000	1.0000
PHASE: BCC-A2#1			
Species	Amount/mol	Mole Fraction	Activity
Cr	0.0000×10^0	6.7643×10^{-13}	3.4140×10^{-3}
Li	0.0000×10^0	1.0000	7.7430×10^{-1}
Total	0.0000×10^0	1.0000	7.7430×10^{-1}

Table 8-8: Equilibrium compositions of chromium using FactSage with a chromium molar fraction used as input.

have been chosen, logically because the free energy barrier is lower producing smaller critical number of molecules and radius values. Therefore, due to this, the postcritical clusters have densities orders of magnitude higher than iron, therefore, it can be assured that the nucleation is more favourable for chromium than iron. Clusters with a number of molecules higher than the critical number in the case of chromium have a much higher probability. The higher the barrier, the higher the probability that a cluster will dissolve.

Figure 8-17: Chromium cluster number density distribution for different sizes $i_{max} = 200$ and 600 .

In the chromium nucleation rate, the order of magnitude is significantly higher than that of iron, due to the same reason as the particle distribution, the postcritical clusters have a significantly higher order of magnitude than the iron, due to the same reason as the particle distribution, the postcritical clusters

Molar fractions ($T = 668$ K)			
Species	Amount/mol		
Cr	1.1190×10^{-5}		
Li	9.9999×10^{-1}		
PHASE: Liquid#1			
Species	Amount/mol	Mole Fraction	Activity
Cr	5.8621×10^{-6}	5.8622×10^{-6}	4.9364×10^{-2}
Li	9.9999×10^{-1}	9.9999×10^{-1}	9.9999×10^{-1}
Total	9.9999×10^{-1}	1.0000	1.0000
PHASE: BCC-A2#1			
Species	Amount/mol	Mole Fraction	Activity
Cr	5.3279×10^{-6}	1.0000	1.0000
Li	6.3285×10^{-16}	1.1878×10^{-10}	7.7430×10^{-1}
Total	5.3279×10^{-6}	1.0000	1.0000

Table 8-9: Equilibrium compositions of chromium using FactSage with a chromium molar fraction increased to $x_l^A = 1.1190 \times 10^{-5}$.

Parameter	Symbol	Value (Unit)
Temperature	T	668 K
Molar Mass	M	51.99 g/mol
Mass Density	ρ	7.19 g/cm ³
Melting Point	T_m	2130 K
Heat of Fusion	ΔH_f	20.48 kJ/mol
Surface Tension	σ	0.14 J/m ²
Diffusion Coefficient	D	8×10^{-11} m ² /s

Table 8-10: Parameters for Cr

have a significantly higher order of magnitude.

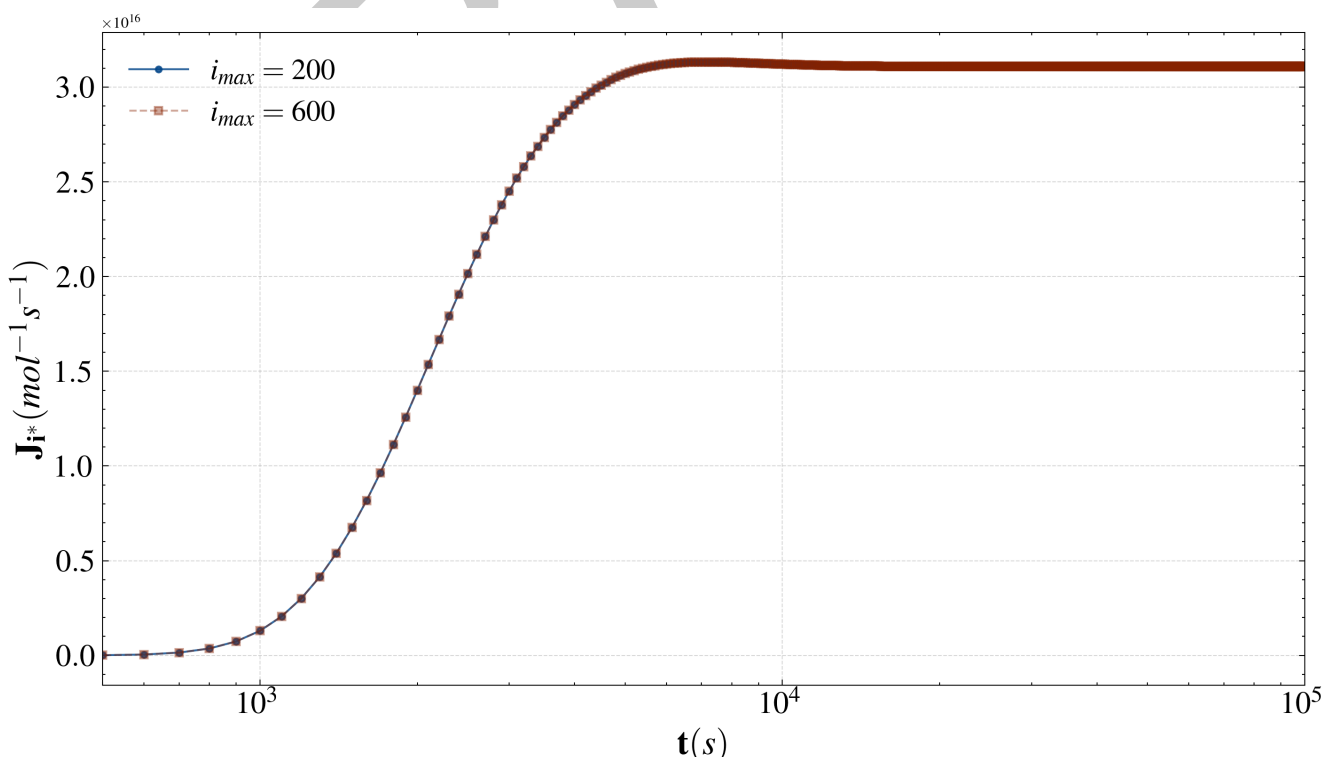
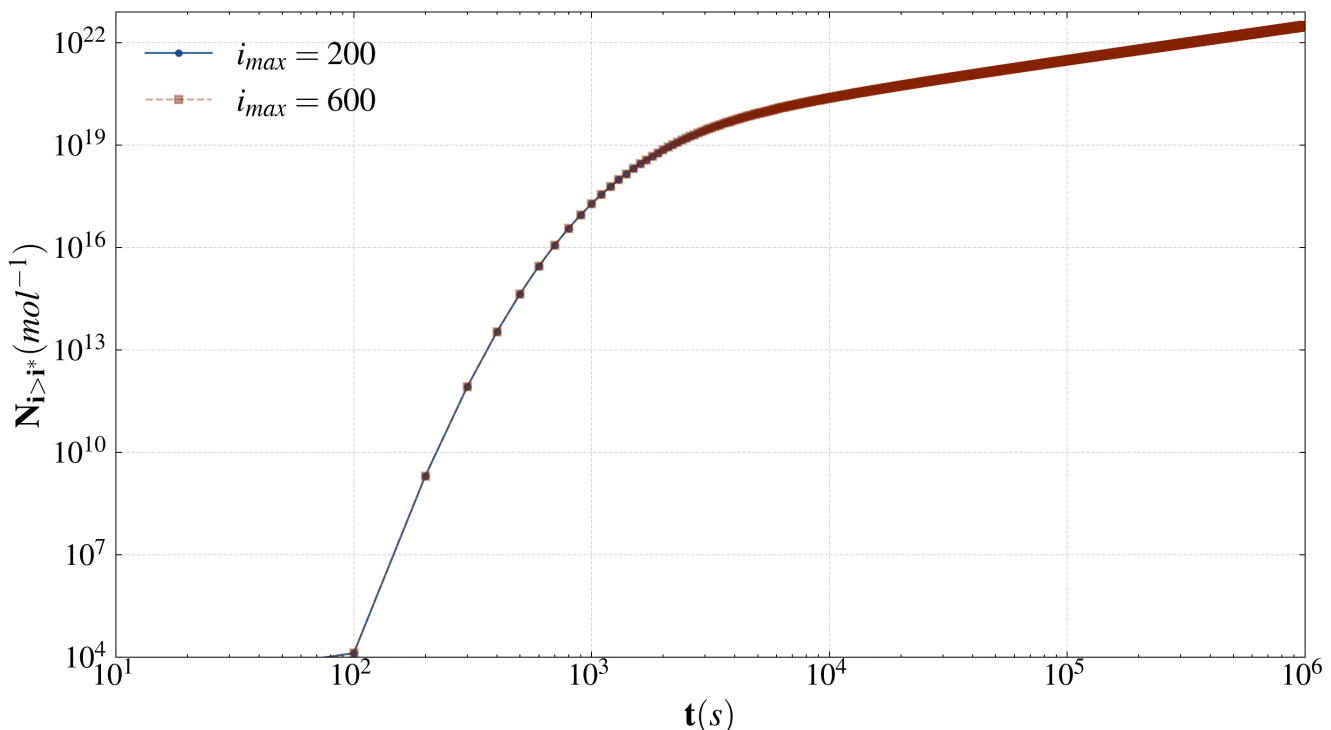


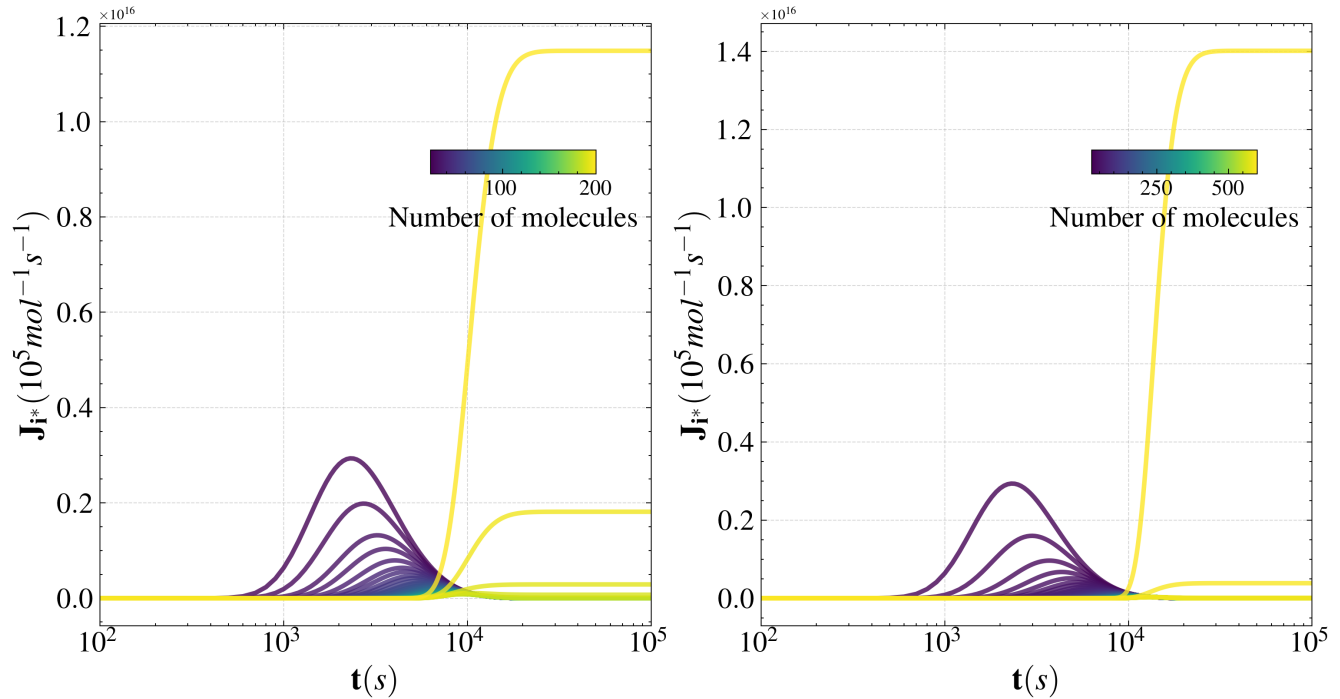
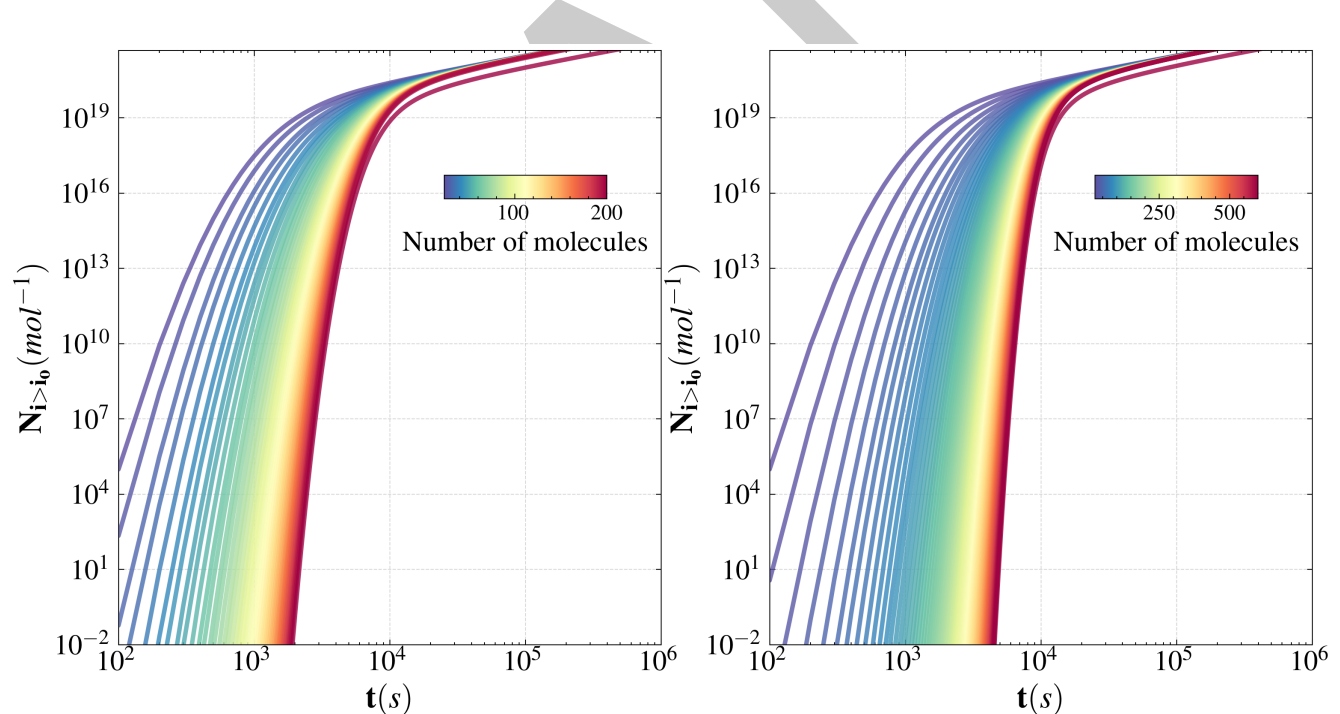
Figure 8-18: Chromium nucleation rates for different sizes $i_{\max} = 200$ and 600.

Parameter	Symbol	Value (Unit)
Critical radius	r^*	0.45 nm
Energy barrier	ΔG^*	2.26×10^{-19} J
Critical number of molecules	n^*	31

Table 8-11: Critical values for Cr

Figure 8-19: Chromium postcritical total number density for different sizes $i_{\max} = 200$ and 600 .

The change in behavior of the nucleation rate for postcritical clusters is noticeable. Initially, for smaller clusters, the pattern follows a normal distribution. As cluster size increases, the trend shifts to resemble the integral of a normal distribution. This shift in behavior is attributed to the adoption of closed boundary conditions, which are implemented to maintain the total number of clusters.

Figure 8-20: Iron nucleation rates for different observable sizes for $i_{\max} = 200$ (left) and 600 (right).Figure 8-21: Iron postcritical total number density for different observable sizes for $i_{\max} = 200$ (left) and 600 (right).**AlN**

In this case, for the impurity Al-N, no phase diagram with lithium has been found, ideally a ternary diagram would be available in great detail, but the biography is very scarce, only a ternary diagram has

been found but with little detail.[61] The only phase diagram with minimal detail available is that of the Li-Al system from FactSage. While it is not accurate to directly assume that the Li-Al-N system will exhibit identical behavior, for the sake of analysis, we might consider similarities. According to the phase diagram, at the operating temperature specific to lithium, a significantly high fraction of aluminum (Al) is necessary for the formation of two distinct phases. In the absence of sufficient aluminum, the system is expected to remain entirely in the liquid state.

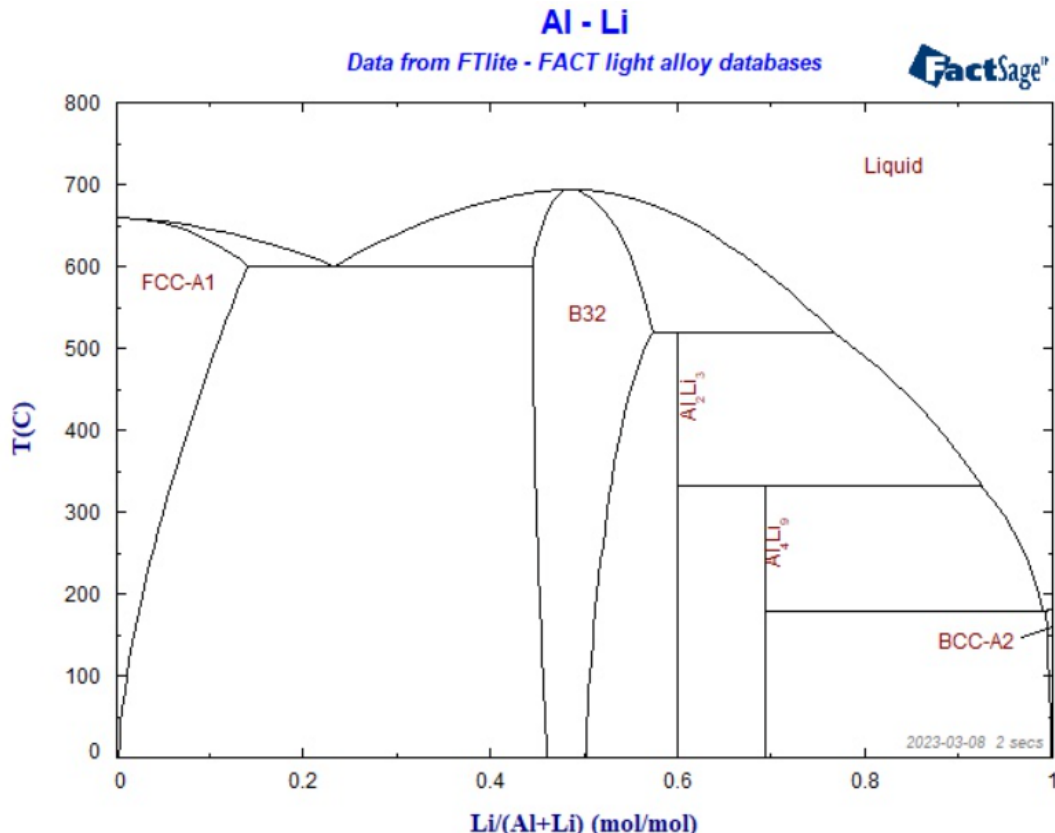


Figure 8-22: Temperature dependence of hydrogen isotope solubility in lithium. [58].

Additionally, information on the diffusivity of Al-N in lithium is lacking. The only rigorous reference identified pertains to the diffusivity of different phases of Al-N [62]. Due to the uncertainty surrounding the variables, it would be premature to present results that may not accurately reflect reality. Therefore, we propose deferring a more detailed investigation of this impurity to secure more reliable thermodynamic and kinetic parameters. Consequently, this deliverable will exclude simulations involving this specific impurity.

8.3.2 Non-metallic impurities

LiH, LiD, LiT

The system consisting of lithium, lithium hydride, and hydrogen (Li-LiH-H₂) has undergone numerous studies. References where solubilities are experimentally found have been reviewed [63, 64, 65, 66, 67].

In [64], experimental isotherms were obtained. Values have been compared with each other and the values are consistent. Each isotherm is divided into three distinct sections. Initially, the rising segment illustrates the interaction of hydrogen with lithium, leading to the formation of a uniform liquid phase where lithium hydride is uniformly mixed within lithium. This region of constant pressure delineates the area where two distinct phases coexist. The edge of this flat section indicates the precise mix of the two simultaneous phases: one predominantly composed of lithium with lithium hydride dissolved within, and the other primarily consisting of lithium hydride with lithium dissolved in it. Upon introducing a hydrogen isotope into this specific area, the proportion of the lithium-enriched phase reduces, whereas the lithium hydride-enriched phase expands, yet the makeup of each phase does not change. According to the precision of experimental measurements, the dividing line (or miscibility gap) and thus the makeup of the two phases remain consistent between the Li-LiH-H₂ and Li-LiD-D₂ systems. The latter part of the rise indicates a phase where lithium integrates evenly within the liquid lithium hydride.

The experimental data are considered in terms of the equilibrium [64]:



where H represents any of the hydrogen isotopes. The equilibrium constant for the above reaction is:

$$K = \frac{N_{LiH}\gamma_{LiH}}{N_{Li}\gamma_{Li}\sqrt{P_{H_2}}} \quad (51)$$

Within the concentration range, Eq. 51 can be rearranged to give the Sieverts relationship:

$$\sqrt{P_{H_2}} = K_s N_{LiH} \quad (52)$$

Where K_s is the Sieverts constant.

The solubilities chosen as design variables are shown in the Fig. 8-23.

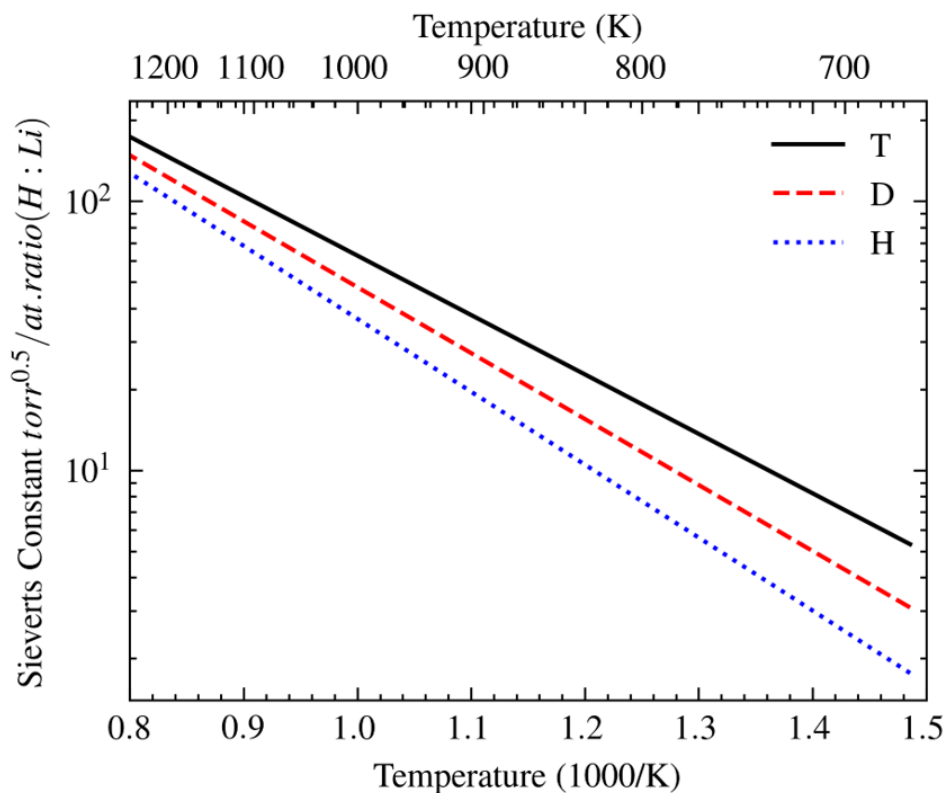


Figure 8-23: Temperature dependence of hydrogen isotope solubility in lithium.

At the operation temperature, the following equilibrium fractions are obtained for each of the hydrogen isotopes

Nuclide	Sieverts Constant (Torr ^{0.5} /[(H:Li)])	(H:Li) Ratio
H	1.65	0.0045
D	2.90	0.00363
T	5.02	0.00360

Table 8-12: Solubility of hydrogen isotopes in lithium

To examine the existing phases, presented below are two phase diagrams of the LiH system: one sourced from the FactSage database [58] and the other from a reference [65].

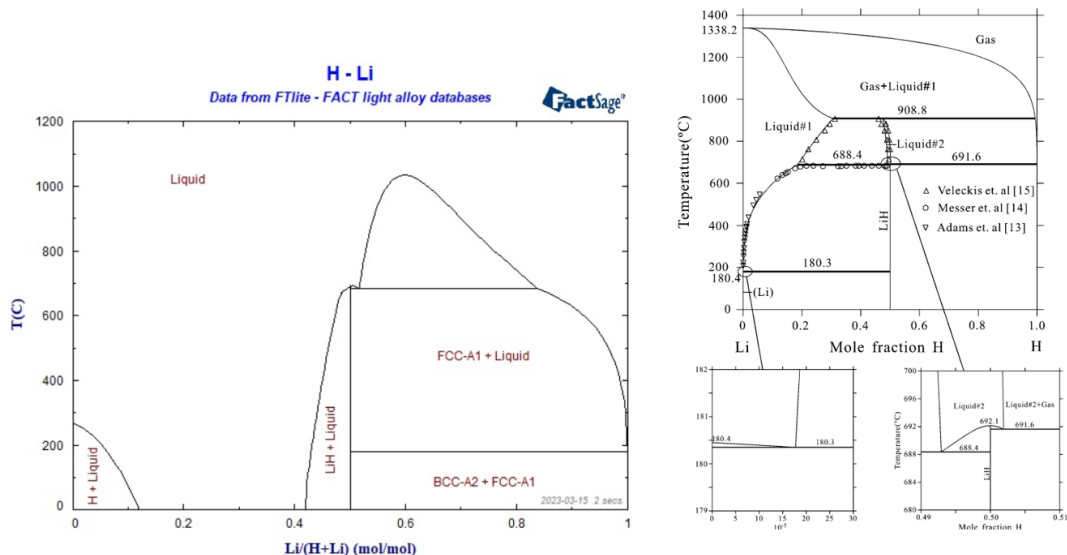


Figure 8-24: LiH phase diagram from FactSage database (left) and for [65] (right).

Unlike the other impurities, hydrogen isotopes are formed from neutron reactions between lithium and the neutrons generated by the fusion reaction. Therefore, the mass fraction obtained in one pulse is assumed. The following table shows the results obtained for each nuclide respectively and the neutron source used.

Reaction	Ratio	mol/m³	(H:Li) Ratio
(n, Xp)	0.015	6.5×10^{-7}	9.12×10^{-6}
(n, Xd)	0.15	6.34×10^{-6}	8.96×10^{-5}
(n, Xt)	1.53	6.5×10^{-5}	9.1×10^{-4}
Neutrons/Pulse	6.2×10^{21}		

Table 8-13: Hydrogen nuclides production

Based on the solubility data and phase diagrams at our disposal, it appears that the mixture will be quite dilute at these specific fractions, exhibiting only a single liquid phase. This observation implies that to reach a state of saturation, where nuclides can precipitate as lithium hydrides, the solution must undergo additional concentration. Consequently, achieving nucleation of the particles may necessitate multiple operational pulses to enhance the liquid's saturation level.

Hence, to acquire initial insights into the size distribution of the clusters, we will proceed under the assumption that the mole fraction of tritium is $1e-1$ and deuterium $1e-2$, and the liquidus temperature for each composition is extracted from the phase diagram [67]. Evidently, it is a concentrated fraction, but looking at the production per pulse of each nuclide, we will always have a higher order of magnitude for tritium compared to deuterium, also the hydrogen concentration will be low, to see the qualitative trend of the distribution of the clusters is enough. In future simulations, the mole fractions and their evolution by pulses will have to be much more refined. For the simulations the following table summarise the parameters, extracted form [68, 63, 64, 65, 66, 67]

Under the given conditions, can be seen that hydrides display a notably low density of postcritical

Parameter	Symbol	LiH (Unit)	LiD (Unit)	LiT (Unit)
Temperature	T	668 K	668 K	668 K
Molar Mass	M	7.95 g/mol	8.94 g/mol	9.93 g/mol
Mass Density	ρ	0.82 g/cm ³	0.82 g/cm ³	0.82 g/cm ³
Melting Point	T_m	961 K	963 K	964 K
Heat of Fusion	ΔH_f	22.59 kJ/mol	22.59 kJ/mol	22.59 kJ/mol
Surface Tension	σ	0.29 J/m ²	0.26 J/m ²	0.25 J/m ²
Diffusion Coefficient	D	1.5×10^{-12} m ² /s	1.4×10^{-12} m ² /s	1.3×10^{-12} m ² /s

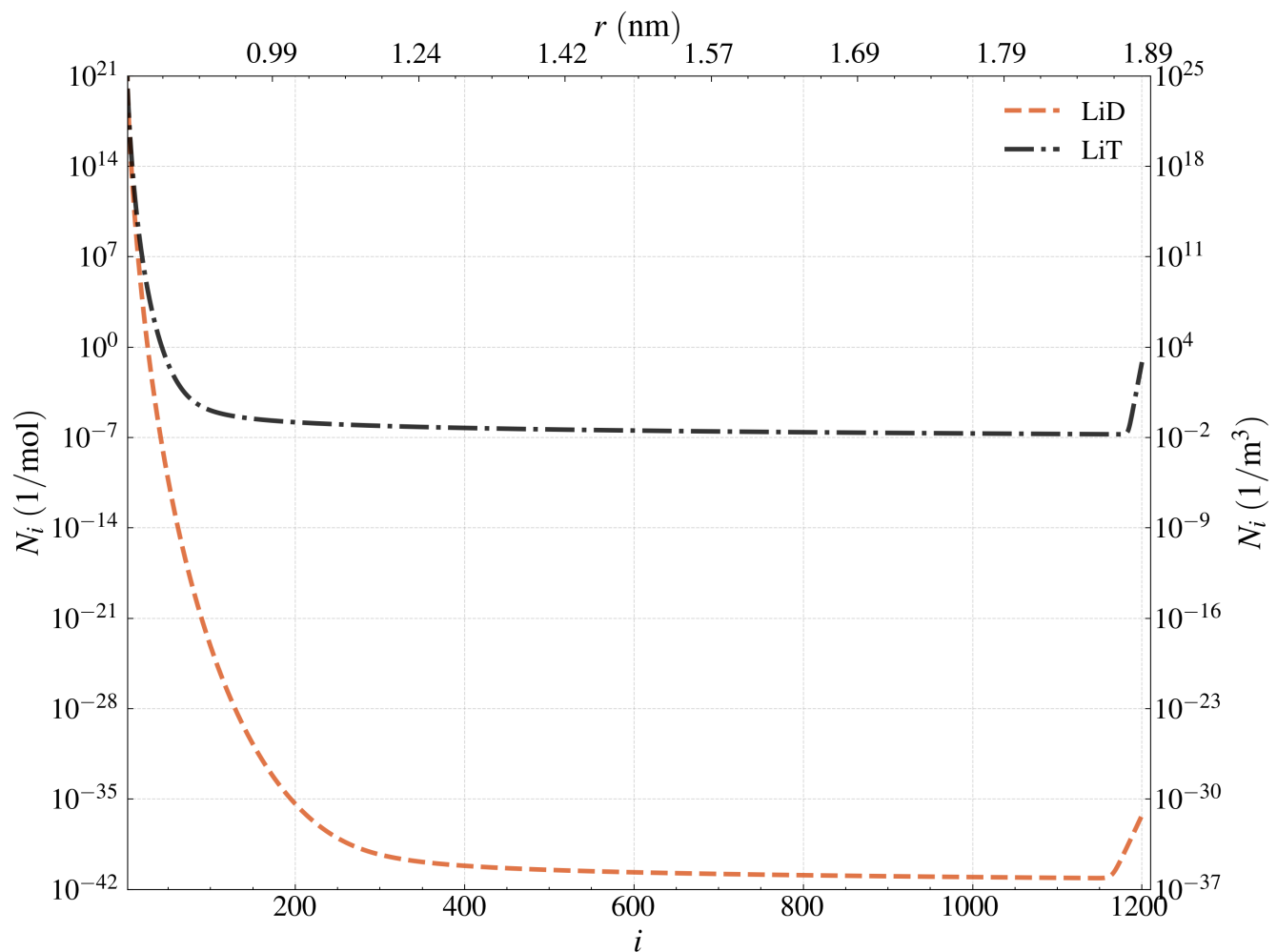
Table 8-14: Parameters for LiH, LiD, and LiT

Parameter	Symbol	D (Unit)	T (Unit)
Critical radius	r^*	1.1 nm	0.78 nm
Energy barrier	ΔG^*	1.36×10^{-18} J	6.31×10^{-19} J
Critical number of molecules	n^*	325	98

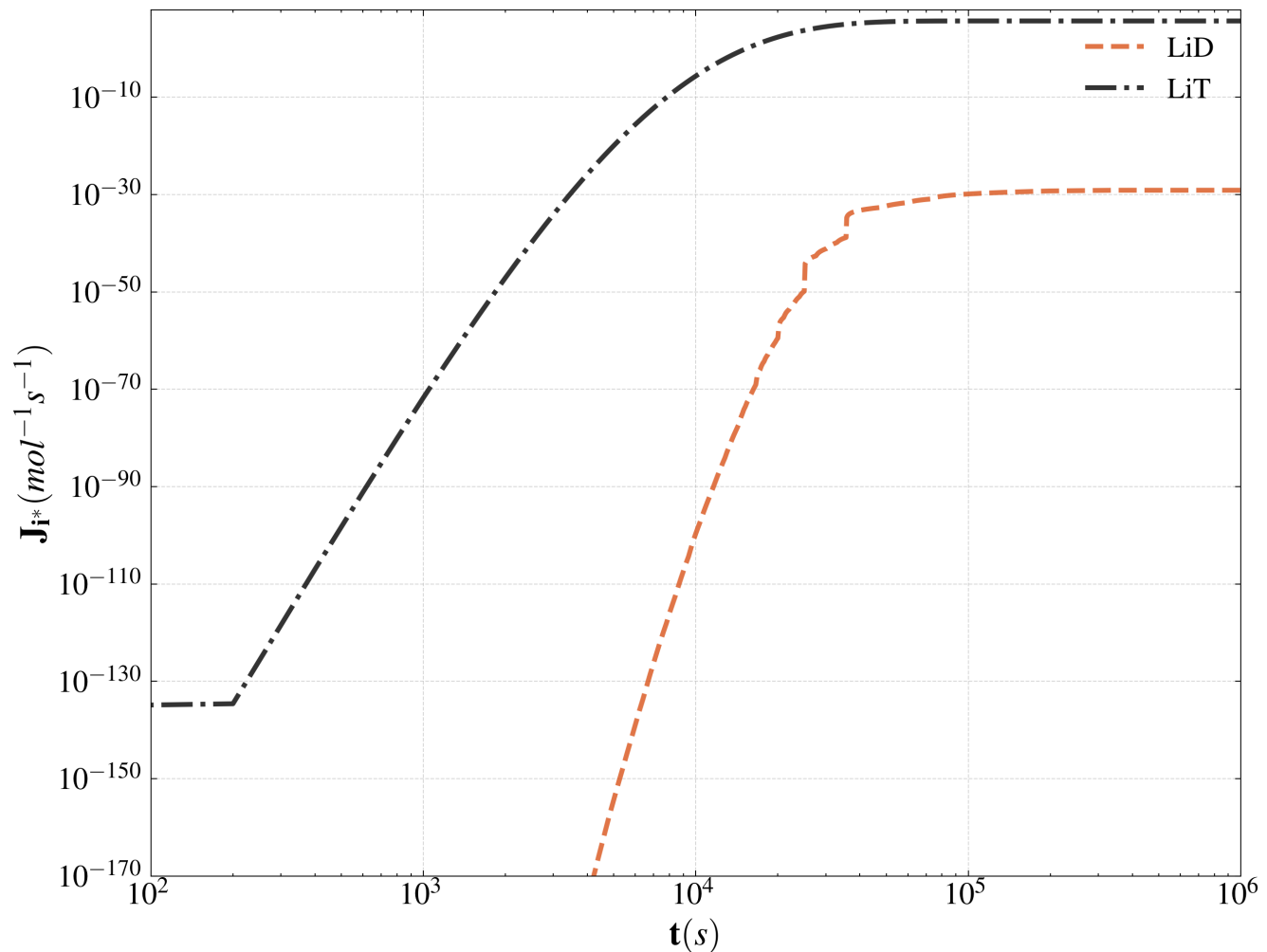
Table 8-15: Critical values for H, D, and T

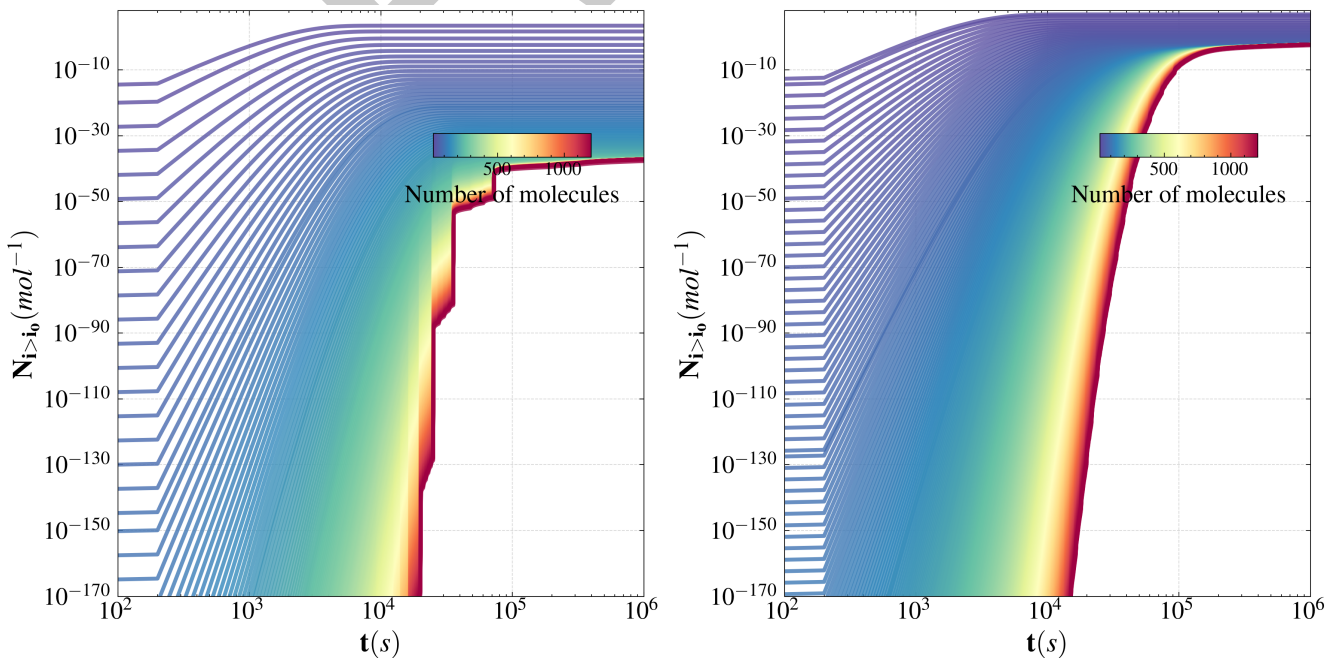
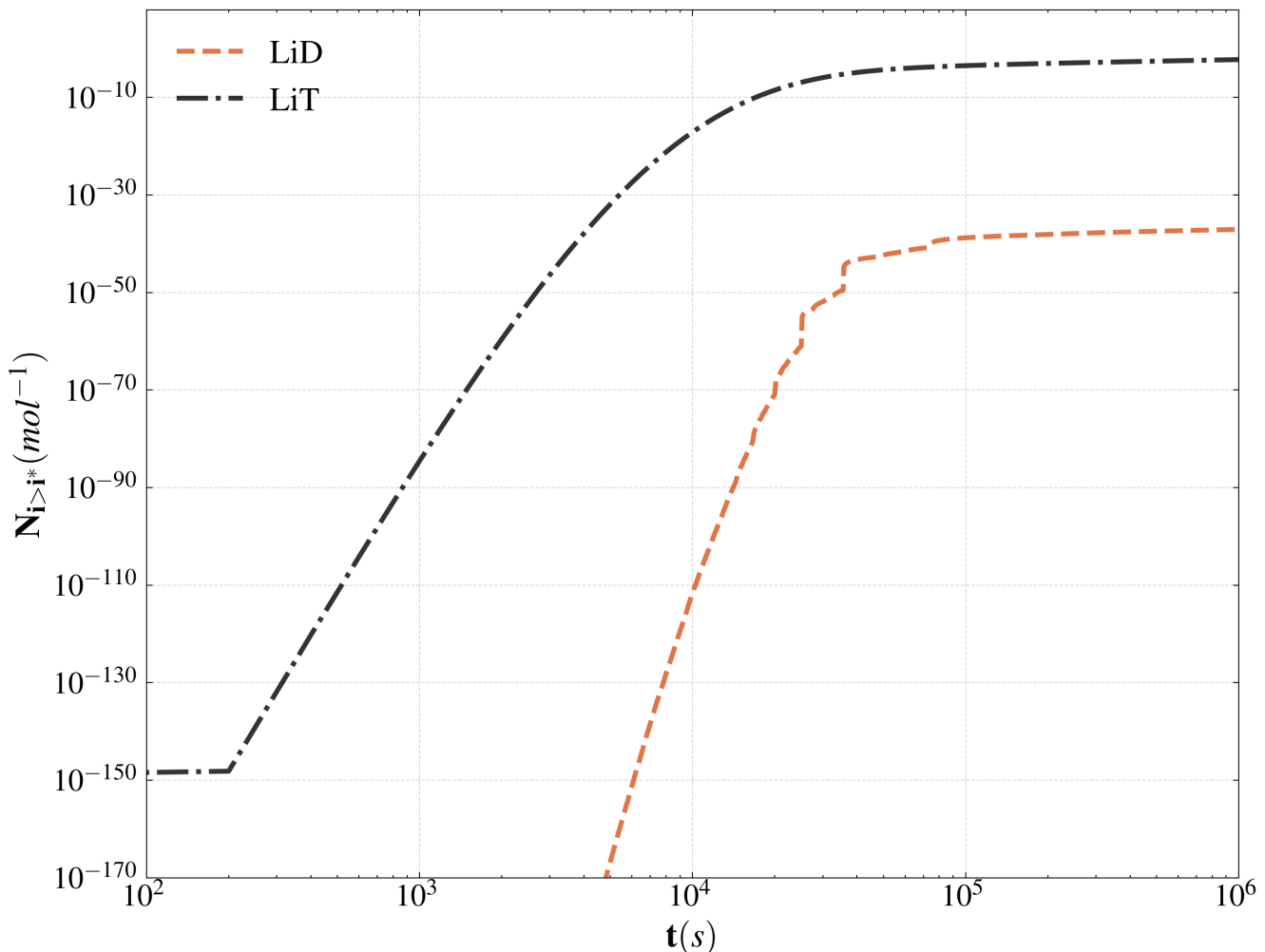
clusters, accompanied by a high energy barrier. This is particularly true for deuterium, which, under these conditions, demonstrates a lower concentration. The varying mole fractions and thermodynamic parameters lead to a distinct outcome: tritium exhibits a higher density of postcritical clusters, indicating it is the nuclide that forms more abundantly under these conditions.

Furthermore, the rate at which both nuclides reach a steady state in terms of postcritical nucleation is slow. Tritium, however, shows a sharp increase over a short duration, while deuterium's increase remains significantly lower. This same pattern is observed in the total number density of the nuclides.

Figure 8-25: Hydrides cluster number density distribution for $i_{\max} = 1000$.

DRAFT

Figure 8-26: Hydrides postcritical nucleation rates for $i_{\max} = 1200$.



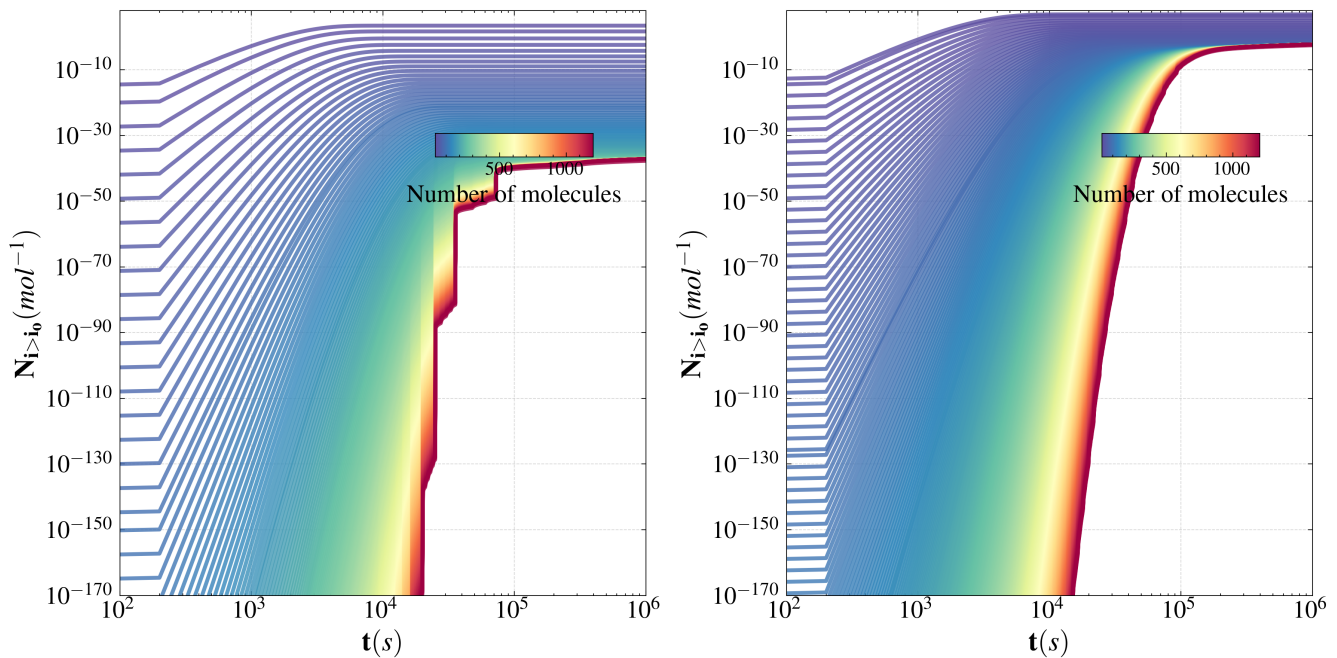


Figure 8-29: Hydrides nucleation rates (deuterium (left) and tritium (right)) for $i_{\max} = 1200$.

The figures presented showcase the nucleation rates and total number densities for deuterium and tritium across various cluster sizes. Notably, deuterium displays significantly lower postcritical values compared to tritium, leading to the inference that deuterium nuclei are more likely to dissolve in lithium without further growth.

Hydrogen is excluded from this analysis due to its substantially lower concentration, as previously mentioned. Therefore, beyond this kinetic examination of nucleus growth, a comprehensive thermo-hydraulic analysis, accompanied by neutron studies, is necessary to fully understand the evolution of hydrides within the system. Incorporating this kinetic analysis as a nucleation foundation allows for a detailed examination of the mass evolution of these nuclides, both on a kinetic level and within the broader scope of macroscopic process scales.

Additionally, as previously mentioned, the choice of model for defining the driving force is critical, as the relationships are exponential, meaning small changes can result in significant differences in the outcomes. Therefore, it is essential to conduct comparisons with careful selection of these parameters. Surface energy is another crucial factor, and it is recognized that this can vary based on cluster size among other factors. In this analysis, a constant value for surface energy has been assumed, which is acknowledged to potentially lead to significant discrepancies in results. Hence, it is determined that for non-metallic impurities, a more detailed examination of these parameters and their evolution within the heat exchanger is necessary.

Li₂O, Li₂C₂

For these non-metallic impurities, no input is available, but their precipitation behaviour in the heat exchanger is also important. Therefore, it has been decided to make a more detailed study for the next deliverable.

9 CENTRIFUGAL TECHNOLOGY SELECTION

With the aim to review the available commercial centrifuges, the current section analyses its application for the purification loop of the RC.

The baseline for the given technologies in sections 9.1 and 9.2 is taken from the SoA report [2], where centrifuge devices for liquid-liquid and liquid-solid separators has been analyzed.

9.1 Single Step Separation Approach

The aim of this study is to provide the centrifuge technology/ies for FLF primary loop with the purpose to extract the solid impurities in the system. The captured requirements for the impurity loop of FLF has been identified as follows:

- Continuous solid impurity extraction.
- Material compatibility.
- Energy efficiency.
- Efficiency for given particle size.
- Operating temperature.
- Maintenance and cleaning.
- Scalability: maximum flow rate.
- Scalability: pressure drop.
- Concentration of impurities.
- Residence time.

Disclaimer

The requirements outlined herein pertain specifically to centrifuge technologies and serve as the foundational basis for the current project. Please note that these requirements are not exhaustive and may be subject to expansion or modification as the project progresses through subsequent stages.

The technologies can be compared based in the criteria given by the requirements, in order to capture which device or set of devices meet successfully the limited framework. Figure 9-1 shows a radar chart with the aim to provide a benchmark based on 8 criteria aligned with the solid separator baseline.

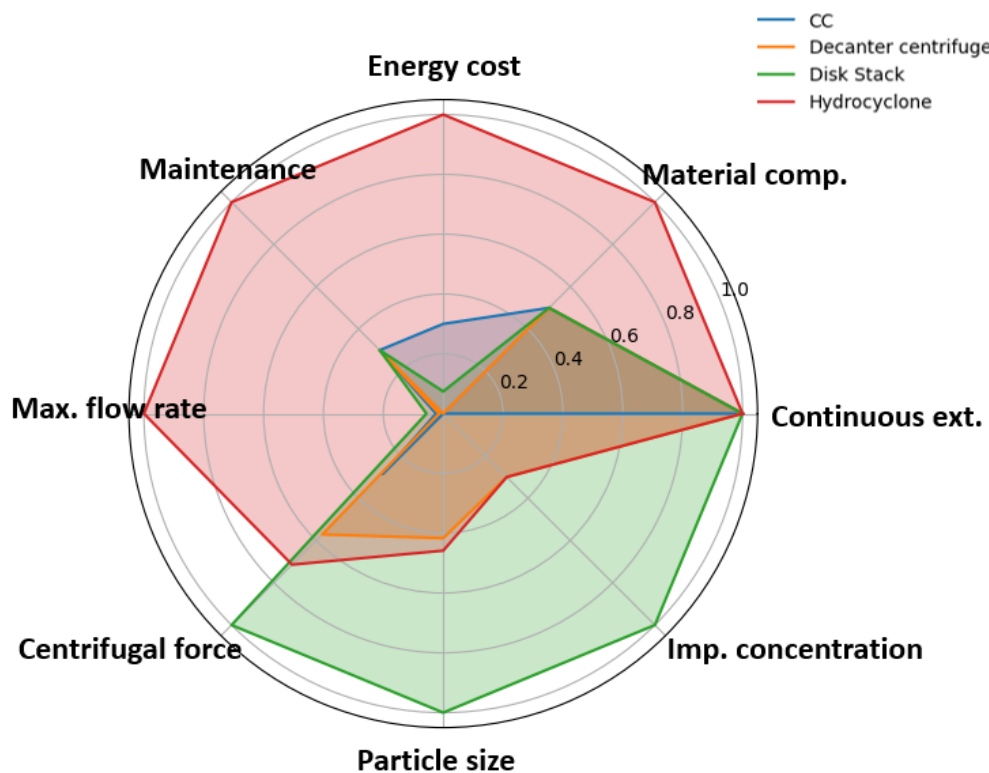


Figure 9-1: Centrifugal technologies comparison chart

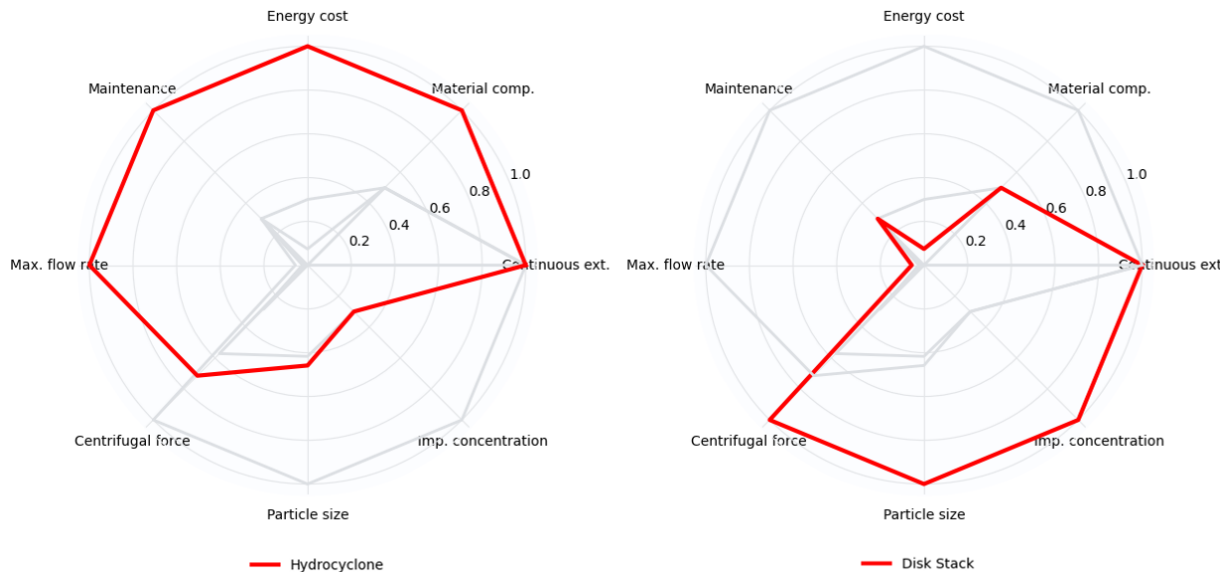


Figure 9-2: Hydrocyclone vs Disk Stack separator: radar plot results

Figure 9-1 shows the performance of 4 centrifugal technologies, with a direct comparison for 8 scores (table 11-1 has the values used for the comparison, that has been normalized, and inverted for Energy Cost, Particle Size, Imp. Concentration). Hydrocyclone and Disk Stack Separator are the technologies with better performance in the evaluated fields, better single definition can be found in figure 9-2, where:

Hydrocyclone

Advantages:

- Material compatibility: The hydrocyclone can be constructed using stainless steel, with SS16 being a commercially available option. Additionally, it can be fabricated from Fiber Reinforced Polymers (FRP), offering notable advantages in aggressive environments such as those found in chemical and nuclear applications with activating products. This versatility in material selection ensures adaptability to varying operational requirements and environmental conditions, enhancing the hydrocyclone's reliability and longevity in demanding settings.
- Maintenance: Characterized by its absence of rotatory components, comprising four conical segments interconnected via flange bolted connections. This design feature ensures facilitated access to the internal cavity, enabling procedures for cleaning, replacement, or repair purposes.
- Energy cost: The inherent design features, including a tangent inlet inducing a vortex through the cone, eliminates the necessity for moving parts, thus precluding the need for an engine. This architectural advantage translates into significant energy savings, as the hydrocyclone operates without any associated energy costs. Moreover, rigorous examination of inlet velocity's impact underscores the meticulous engineering approach applied to optimize performance.
- Flow rate: It demonstrates superior flow rate management in comparison to the other three analyzed technologies. Moreover, it is commercially available to operate within a manifold architecture, allowing for efficient handling of large volumes. Consequently, it emerges as a prime candidate for processing the primary loop lithium in a single operation.

Disadvantages:

- Particle size: Commercially available up to a particle size of $12 \mu m$, with an impressive efficiency rate of 98%, while maintaining scalability with a compromise on pressure drop (10-200 KPa). This equilibrium represents the optimal trade-off. Consequently, particles below $12 \mu m$ can be captured by the hydrocyclone; however, ensuring consistent efficiency for particles of this size is not assured. Therefore, additional stages specifically designed for particles of this size range must be incorporated into the purification system to ensure thorough filtration and purification.
- Impurity concentration: The technology's optimal operational range encompasses concentrations of impurities in the medium exceeding 10%. Therefore, it is recommended to position this technology as the initial stage within the purification system. This strategic

placement ensures efficient removal of contaminants at higher concentrations, thereby enhancing the overall effectiveness of the purification process. Future stages may address more accurate the impurity concentration in the system.

Assessment: The hydrocyclone offers exceptional material compatibility, maintenance-friendly design (without of rotatory components), with negligible energy costs and superior flow rate management, based on manifold architectures: the hydrocyclone emerges as an ideal candidate for processing the primary loop fluid. Despite limitations in capturing particles below $12 \mu m$ and optimal operation at impurity concentrations exceeding 10%, strategic integration within purification systems enhances overall effectiveness.

Disc Stack Separator

Advantages:

- Particle size: One of the most notable strengths of this technology lies in its ability to effectively capture particles as small as $1 \mu m$, facilitated by its high centrifugal force and innovative ribs cavity design, which accelerates solid precipitation. Particularly advantageous in scenarios where prior classification or clearance of larger particle sizes has been performed, allowing for optimal exploitation of its particle-capturing capabilities.
- Impurity concentration: The operational range for these devices remains optimal when impurity concentrations are below 10%, presenting an advantageous characteristic when integrated into multi-stage system operations.
- Centrifugal force: As a high-speed separator capable of achieving up to 14,000 G, the disk stack separator offers a distinct advantage due to its efficient operation at relatively low energy costs, contrasting with decanter centrifuges. While centrifuge contractor may require similar energy inputs, they do not attain comparable levels of centrifugal force, highlighting the disk stack separator's pivotal role in separation processes based on its design principles.

Disadvantages:

- Energy cost: Exhibits relatively higher energy consumption compared to alternative solutions. This aspect should be considered in the evaluation of operational costs and efficiency metrics within the full-scale context.
- Maintenance: The trade-off associated with attaining high-speed rotation velocities may influence the maintenance of components, wherein direct access to elements is not a direct action, requiring mechanical assembly-disassembly processes that are less straightforward compared to hydrocyclones.

- Flow rate: The limited maximum flow rate capacity of such devices makes them unsuitable for fully processing all the lithium within the primary loop. Furthermore, the absence of commercially available manifolds presents a challenge. Therefore, a rigorous study could be needed to strategically place these devices within the system, coupled with the feasibility assessment for developing a manifold configuration to optimize operational efficiency.

Assessment: The Disk Stack Separator offers good particle capture capabilities, particularly for particles as small as $1 \mu\text{m}$, making it ideal for scenarios requiring precise filtration after prior particle classification. However, its higher energy consumption and maintenance complexities warrant careful consideration. When compared with hydrocyclones, which excel in energy efficiency and maintenance simplicity, they form complementary components in a comprehensive purification system, each tailored to specific operational requirements and constraints. Integrating both technologies strategically within a multi-stage system can optimize overall efficiency and performance, complementing their disadvantages.

Decanter Centrifuge

Decanter centrifuges demonstrate comparable performance to hydrocyclones in particle size handling, centrifugal force generation, and impurity concentration control. However, hydrocyclones offer superior energy efficiency, enhanced material compatibility, and lower maintenance requirements, presenting clear advantages. Notably, hydrocyclones excel in maximizing the maximum flow rate, making them a preferred choice in scenarios prioritizing throughput efficiency and operational cost-effectiveness.

Centrifuge Contactor

While centrifuge contactors offer the advantage of producing four-phase liquid separation, they do not present a significant advantage in the fields compared to hydrocyclones. The technology lacks suitability in efficiently handling impurities at required flow rates with the precision demonstrated by alternative technologies, diminishing its practical utility in for the primary loop.

9.2 Multi-Step Separation Approach

In the context of a multi-stage separation process, the integration of hydrocyclones and Disk Stack Separators offers a comprehensive solution for fluid purification. The hydrocyclone, as particle cut-off controlled by operation parameters, is particularly adept at classifying and separating coarser particles ($> 12 \mu\text{m}$), thereby facilitating the initial removal of larger impurities. Its attributes, including superior material compatibility and a maintenance-friendly design, make it a suitable choice for efficiently processing substantial fluid volumes, thanks to its ability to handle high flow rates and adapt to various manifold configurations.

However, the hydrocyclone's inherent limitations, such as its inability to capture particles below $12 \mu\text{m}$ and its optimal operation in scenarios with impurity concentrations above 10%, necessitate additional stages for thorough purification. This is where the Disk Stack Separator comes into play, especially in scenarios where specific targets, such as low impurities or activated products separated by density differences like Li-H, need to be addressed. Renowned for its exceptional particle capture efficacy, particularly for particles as small as $1 \mu\text{m}$, the Disk Stack Separator strategically placed downstream of the hydrocyclone enhances the purification process by effectively removing finer particles and residual impurities at low concentrations (up to 0.05%), thereby ensuring the level of lithium purity.

Despite its advantages, the Disk Stack Separator incurs relatively higher energy consumption and maintenance complexities compared to the hydrocyclone. Therefore, meticulous attention is needed in optimizing the integration of these technologies to ensure overall efficiency. For example, incorporating the Disk Stack Separator as a secondary stage in the purification process allows for precise filtration after larger particles have been removed by the hydrocyclone, as shown in Figure 9-3. At the same time, it raises the requirement to project a future device that captures the high efficiency for small particles at the energy cost and lithium volumes of the hydrocyclone.

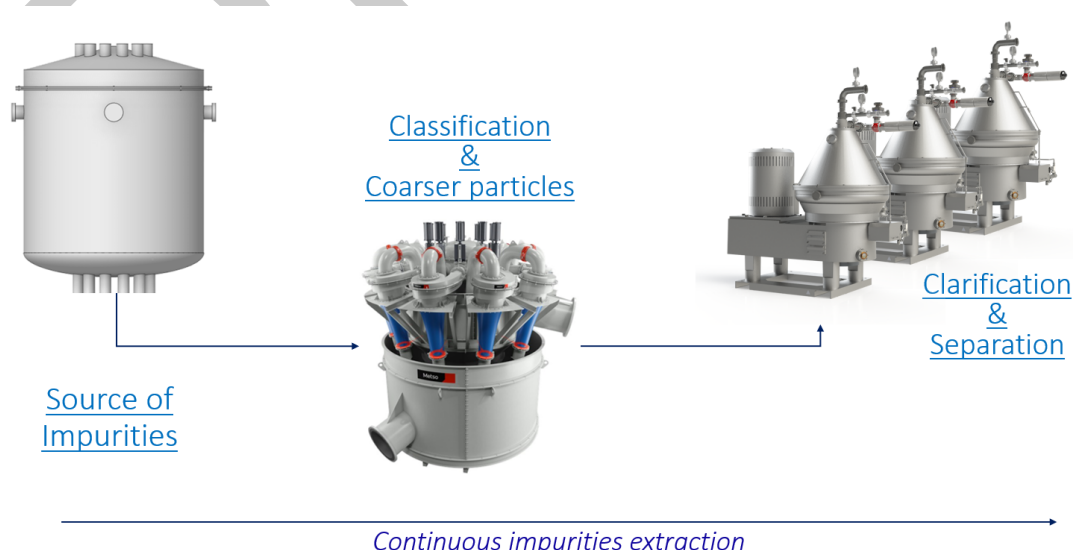


Figure 9-3: Multi stage configuration

In this multi-stage paradigm, the symbiotic relationship between the hydrocyclone and Disk Stack Separator maximizes each technology's strengths while mitigating respective weaknesses.

The relevant technical specifications for both technologies are delineated in Figure 9-4. This technical data serves as the foundational benchmark for subsequent stages of the project, guiding the development of solutions aligned with the current multi-stage framework. The analysis of this data informs decisions regarding the integration of technologies, aiming to optimize the process schema and ultimately enhance overall efficiency and effectiveness.

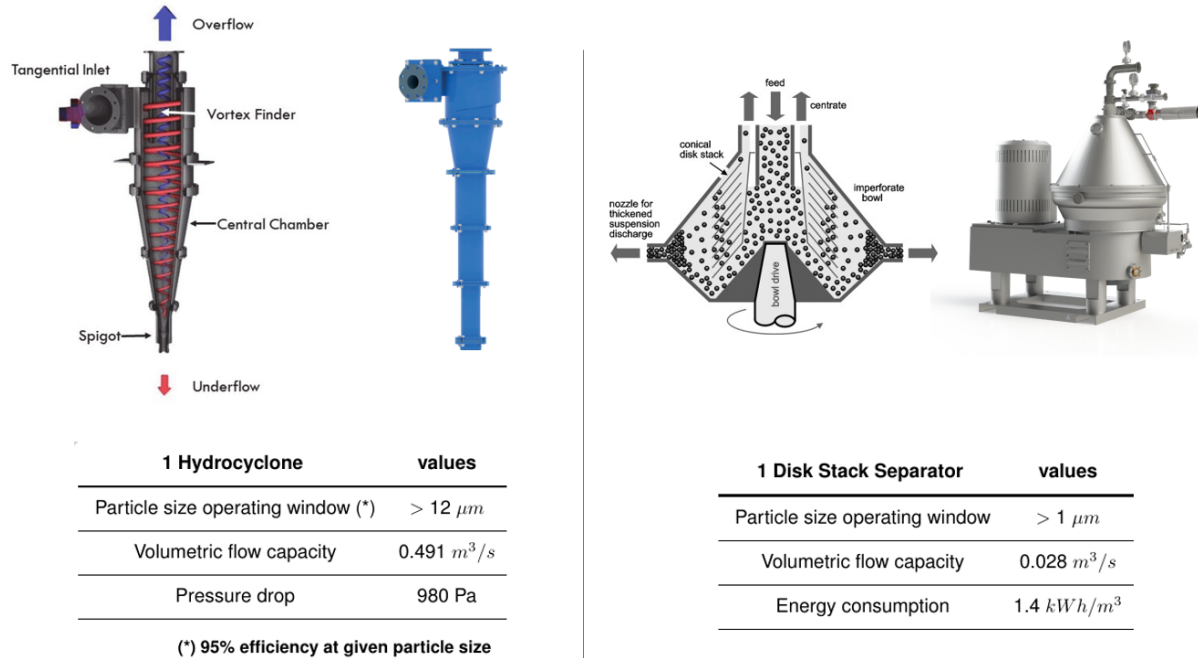


Figure 9-4: Multi stage device data-sheet

9.3 Hydrocyclone: Mathematical modelling

Cyclone separators are widely used in the field of chemical, mine and petroleum industries. ref.[69] With the advantages of relative simplicity to fabricate, low cost to operate and good adaptability to extremely harsh conditions, cyclone separators have become one of the most important particle removal devices which are preferably utilized in both environmental and chemical engineering. In order to describe the performance of cyclone separators, many (gas or liquid)-particle separation theories were developed using different methods with different simplifications and assumptions. All these can be roughly divided into the pure theory, the semi-empirical theory and the numerical simulation. The former two include the equilibrium-orbit model, time-of-flight model and hybrid model, etc., the later mainly refers to the computation fluid dynamics (CFD) approach ref.[70].

In detail, the equilibrium-orbit model, as an early methodology of particle separation, determines the particle size for which centrifugal force is exactly balanced by the drag force. Correspondingly, the collection efficiency for the critically sized particle is often assumed to be 50% efficiency called cut particle diameter $d_{c,p}$ ref.[71].

In this section, the necessary parameters and assumptions are defined to correctly define the equilibrium orbit model and obtain an expression for the cyclone separation efficiency.

Assumptions

The following assumption have been made in order to develop the equilibrium-orbit model ref. [72]:

- The particle is spherical in shape, the motion of the single particle is not influenced by the presence of neight-boring particle.
- The tangential velocity of the particle is same as the disperse phase stream; and with the particle is the right dispersed phase, the radial velocity direction to the particle always point to inner vortex.
- The particle move into the inner vortex is the only way to be separated.

Figure (9-5) show a generic scheme of the cyclone and the description of the different variables is presented in table (9-1).

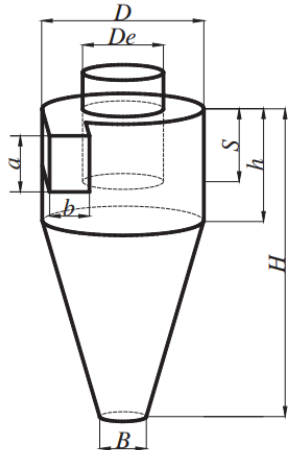


Figure 9-5: Schematic diagram of typical cyclone dimensions.

variable	description
<i>a</i>	Cyclone inlet height (m)
<i>b</i>	Cyclone inlet width (m)
<i>B</i>	Particle outlet diameter (m)
<i>D</i>	Cyclone body diameter (m)
<i>D_e</i>	Liquid outlet diameter (vortex finder diameter) (m)
<i>h</i>	Cyclone cylinder height (m)
<i>H</i>	Cyclone height (m)
<i>S</i>	Liquid outlet duct length (m)

Table 9-1: Description of the geometrical variables of one cyclone.

9.4 Fluid model

Swirling flow, or vortex flow, occurs in different types of equipment, such as cyclones, hydrocyclones, spray dryers and vortex burners. Two types of ideal swirling flows are ref.[73]:

- Forced vortex flow: swirling flow with the same tangential velocity distribution as a rotating solid body.

$$v_{\theta,f} = \omega r \quad (53)$$

- Free vortex flow: the way a frictionless fluid would swirl. The tangential velocity in such a swirl is such that the moment-of-momentum of fluid elements is the same at all radius.

$$v_{\theta,f}(r) = \frac{\kappa}{r^n} \text{ where } 0.4 < n < 0.9 \quad (54)$$

where κ is a geometrical parameter and n is a experimental value taken 0.88 as in ref.[74]

Figure (9-6) show the schema of the real tangential velocity distribution and the comparison with the forced and free vortex flow.

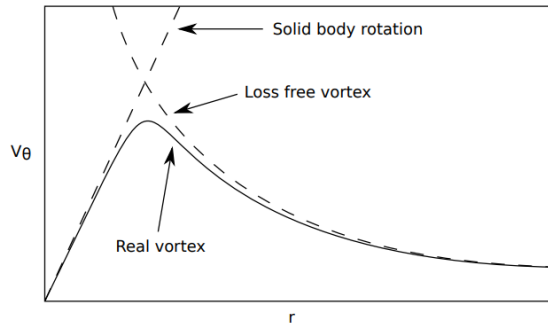


Figure 9-6: Scheme of the 2 ideal vortex model and the tangential velocity distribution in a real vortex.
ref.[73]

9.5 Motion of suspended particles

In a hydrocyclone, the particles of interest are almost always moving relative to the liquid at their terminal velocity, and the terminal velocity of a given particle determines whether the particle will be captured or lost.

Applying Newton's law to a particle moving in a fluid, equating its mass times acceleration to the sum of the forces acting on it, gives :

$$m \frac{dv}{dt} = F_{body} + F_{drag} + F_{unsteady} \quad (55)$$

where the body force is normally due to a centrifugal force and the fluid drag represents the drag acting on a particle that moves with a steady velocity relative to the fluid ref.[74]. According to several authors ref.[69, 73], it turns out that these unsteady terms can be ignored both for the case of a gas cyclone and a hydrocyclone, as practical plant experience with their design and operation indicates that it is not necessary to include either of the terms.

The centrifugal force (first term on the right part) can be expressed as :

$$F_{body} = F_{centrifugal} = V_p (\rho_p - \rho_f) \mathbf{a} \quad (56)$$

where V_p is the particle volume, ρ_p is the particle density, ρ_f is the fluid density and \mathbf{a} is the global effect of the radial and angular particle acceleration.

In cylindrical coordinate, omitting the axial contribution,

- $a_r = \frac{dv_{r,p}}{dt} = \frac{d^2r}{dt^2}$ particle radial acceleration
- $a_c = r \left(\frac{d\theta}{dt} \right)^2 = r \left(\frac{v_{\theta,f}(r)}{r} \right)^2$ particle angular acceleration

assuming that the radial particle acceleration in the steady state is negligible, the centrifugal force is equal to:

$$F_{centrifugal} = \frac{1}{6} \pi d_p^3 \cdot (\rho_p - \rho_f) \cdot \frac{v_{\theta,f}^2(r)}{r} \quad (57)$$

on the other hand, when the particle Reynolds number is low ($Re_p = \frac{d_p v_{r,p}}{\nu} \ll 1$), the equations of

motion for the fluid moving around the particle can be solved, and the drag force calculated. If there is no slip between fluid and particle surface, the particle velocity is equal to the velocity of the fluid at the surface, the result is Stokes drag law:

$$F_{drag} = 3\pi\mu d_p v_{r,p}(r) \quad (58)$$

Therefore, in the steady state, the drag force have to be equal that the centrifugal force:

$$\sum F_p = 0 \Rightarrow F_{centrifugal} = F_{drag} \quad (59)$$

and the radial velocity of the particle can be expressed as a function of the angular velocity of the fluid given by the vortex flow model as

$$v_{r,p}(r) = \frac{\Delta\rho d_p^2}{18\mu} \cdot \frac{v_{\theta,f}^2(r)}{r} \quad (60)$$

The following subsections define different parameters necessary to calculate the cyclone separation efficiency.

9.6 Cyclone effective volume

To avoid the non-uniform effect on particle collection distance caused by difference between cylindrical and conical shape, the cylinder-conical geometry is equivalently modified as a right cylinder cyclone according to the principle of conservation of effective volume. The equivalent cyclone volume (V_{cs}) and radius (R) can be calculated by: ref.[71]

$$V_{cs} = \begin{cases} \frac{\pi D^2 h}{4} + \frac{\pi D^2}{4} \cdot \frac{S+l-h}{3} \cdot \left[1 + \frac{D_c}{D} + \left(\frac{D_c}{D} \right)^2 \right], & \text{if } l \leq (H-S) \\ \frac{\pi D^2 h}{4} + \frac{\pi D^2}{4} \cdot \frac{H-h}{3} \cdot \left[1 + \frac{B}{D} + \left(\frac{B}{D} \right)^2 \right], & \text{if } l > (H-S) \end{cases} \quad (61)$$

$$R^* w = \begin{cases} \left[\frac{V_{cs}}{\pi(S+l)} \right]^{1/2}, & \text{if } l \leq (H-S) \\ \left[\frac{V_{cs}}{\pi H} \right]^{1/2}, & \text{if } l > (H-S) \end{cases} \quad (62)$$

where $D_c = D - \frac{(D-B)(S+l-h)}{H-h}$ and l is called as the natural vortex length of cyclone separator. It is defined as the vertical distance from the bottom of the vortex finder to the end of the vortex at which the outer vortex is reversed or turned into the inner vortex. l is actually the effective vortex length in cyclone separator if it is less than the dimension $H-S$. Otherwise, $H-S$ should be the effective vortex length because it depends on the geometrical dimensions of cyclone. The most famous and widely used relation for estimating the natural vortex length is the Alexander' formula ref.[71]:

$$l = 2.3 \left(\frac{D^2}{ab} \right)^{1/3} \quad (63)$$

9.7 Residence time model

The residence time t_{res} is the average time that a particle is inside the cyclone. The expression to calculate t_{res} depend of the geometry of the cyclone and the inlet volumetric flow rate, so according to the geometry selected (Figure 9-5) the residence time can be calculated as ref.[71]:

$$t_{res} = \begin{cases} \frac{\pi(R^2 - R_e^2)}{Q/2} \cdot l, & \text{if } l \leq (H - S) \\ \frac{\pi(R^2 - R_e^2)}{Q/2} \cdot (H - S), & \text{if } l > (H - S) \end{cases} \quad (64)$$

9.8 Separation efficiency model

In order to calculate the separation efficiency of the cyclone, a balance of mass was made in the volume of control presented in the Figure (9-7) ref.[71, 72].

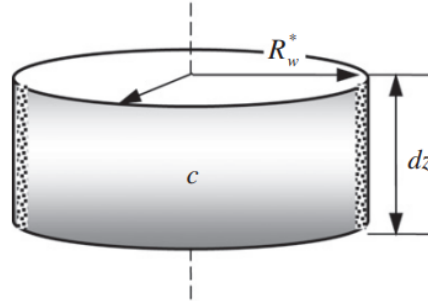


Figure 9-7: volume of control used in the separation efficiency model. ref.[71]

In this control volume, it is assumed that uncollected particles in any plane perpendicular to the cyclone axis presents a status of complete radial back-mixing, the boundary layer near the equivalent wall is neglected and particles which move to the equivalent wall will be trapped. If the particle concentration in the control volume is c , then the particle flux toward the equivalent wall is $cv_{r,p}(R_w^*)$. Therefore, over a height dz the sedimentation rate of particles at the equivalent wall is $2\pi R_w^* cv_{r,p}(R_w^*)$. Correspondingly, the rate of particles separated from the control volume is $c\pi R_w^{*2} dz$. According to particle mass balance, we have:

$$\frac{dM}{dt} = \sum M_{in} - \sum M_{out} \quad (65)$$

$$\frac{d(c\pi R_w^{*2} dz)}{dt} = - \sum M_{out} = -cv_{r,p}(R_w^*)2\pi R_w^* dz \quad (66)$$

$$\frac{dc}{dt} = - \frac{2v_{r,p}(R_w^*)}{R_w^*} \cdot c \quad (67)$$

$$\frac{c(t)}{c_0} = \exp\left(-\frac{2v_{r,p}(R_w^*)t}{R_w^*}\right) \quad (68)$$

Integrating, with $c(t = 0) = c_0$ and $c_{final} = c(t_{res})$ where t_{res} is the particle residence time:

$$\frac{c_{final}}{c_0} = \exp\left(-\frac{2v_{r,p}(R^* w)t_{res}}{R^* w}\right) \quad (69)$$

therefore, the separation efficiency is defined as

$$\eta = 1 - \frac{c_{final}}{c_0} \quad (70)$$

$$\eta = 1 - \exp\left(-\frac{2v_{r,p}(R^* w)t_{res}}{R^* w}\right) \quad (71)$$

where $v_{r,p}(R^* w)$ is the particle settling velocity at the equivalent wall and is calculated according to Eq. (60)

10 Results: Parametric analysis

For the following analysis, the geometric dimensions present in the table 10-1 have been used as a basis. This information was used to see how the separation efficiency of the cyclone varies when the Lithium temperature, the diameter of the cyclone and the inlet flow change.

variable	value
D	0.5 m
$\frac{D_e}{D}$	0.5
$\frac{a}{D}$	0.5
$\frac{b}{D}$	0.2
$\frac{S}{D}$	0.5
$\frac{H}{D}$	4
$\frac{h}{D}$	1.5
$\frac{B}{D}$	0.375
Fluid material	Lithium
Fluid Temperature	688 K
Particle material	Fe

Table 10-1: Input information used for the parametric analysis section

10.1 Parametric analysis: Temperature

Figure (10-1) shows the efficiency as a function of the particle diameter of Fe for the temperature of the Start-Up, HEX outlet and lower tank calculated in ref. [75].

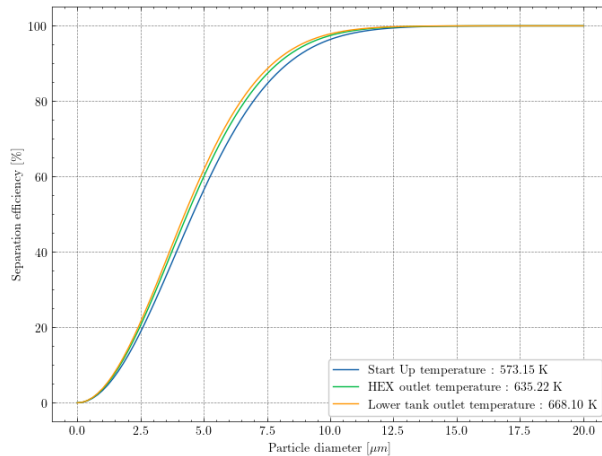


Figure 10-1: Separation efficiency as a function of the particle diameter of Fe for different temperatures.

As the temperature increases, the fluid viscosity decreases, so the drag force decrease and the particle velocity increase. Also, the difference in density fluid-particle also increases (since the density of lithium decreases with temperature) so that the centrifugal force grow. Those effects allows efficiency to increase with temperature.

10.2 Parametric analysis: Cyclone diameter

Figure (10-2) shows the separation efficiency as a function of the particle diameter of Fe for different cyclone diameters.

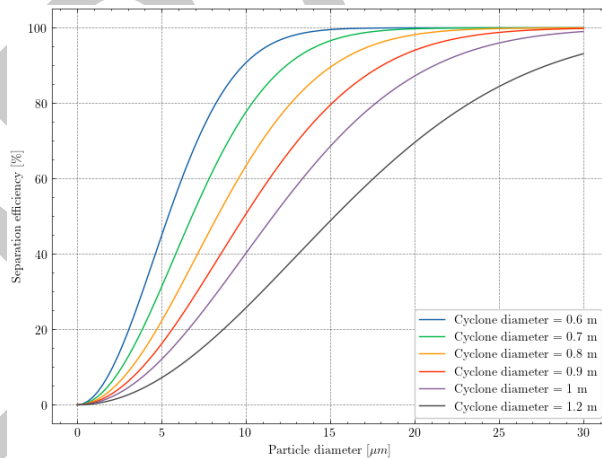


Figure 10-2

By increasing the diameter and keeping the scaling and flow variables constant, the velocity in the inlet decreases. This decrease causes that the velocity of the particles to drop and the efficiency to drop. On the other hand, as the diameter increases, the residence time increases given by the equation (64) and this effect tends to increase efficiency, however, it is not as important as the other effect mentioned before.

Thus, there is a trade-off in deciding the optimal cyclone diameter, and it will also depend on the minimum particle diameter of the impurities which need to be eliminated.

10.3 Parametric analysis: volumetric inlet flow rate

Given one of the limitations of cyclones is the possibility of scaling efficiency to industrial-type flows, in the chemical or mine industry it is very common to use more than 1 cyclone in parallel ref. [69]. For this reason it is of interest to know how the efficiency changes as we increase the volumetric inlet flow rate of the cyclone.

Figure (10-3a) show the separation efficiency as a function of the particle diameter for different volumetric inlet flow rate form from 0.5 to 3.5 m^3/s (similar to pilot plant).

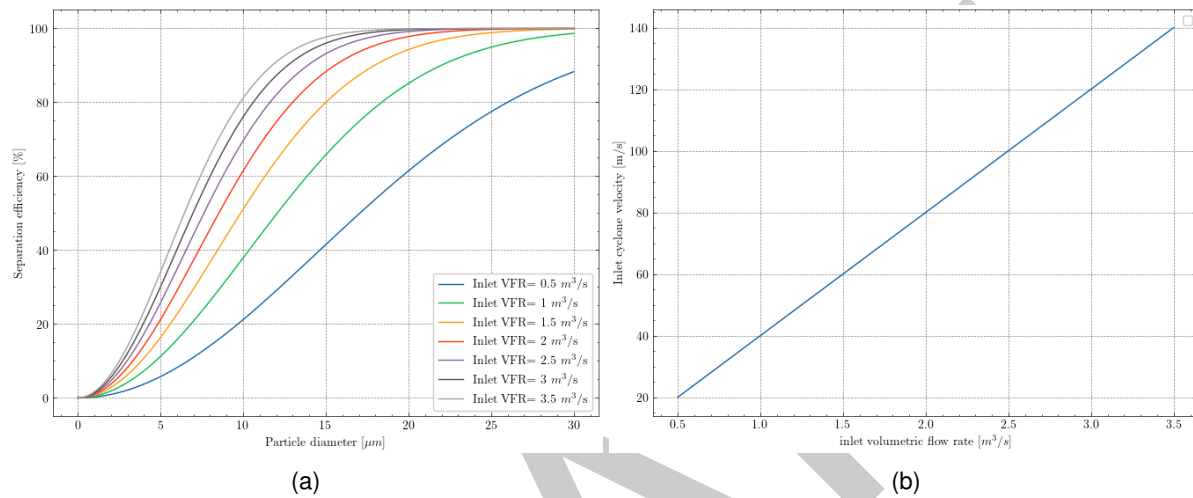


Figure 10-3

It can be seen that as volumetric flow rate decrease, the separation efficiency decreases. This is because as the flow rate at the inlet of the cyclone decreases, the velocity in the inlet drop (Figure 10-3b) and consequently the velocity with which the particle heads towards the walls of the cyclone. It is important to note that industrial-scale cyclones usually operate with an inlet speed between 20-30 m/s, so this limitation should be added in the following sections to have a realist results.

Figure (10-4a) show the separation efficiency as a function of the particle diameter when VFR change +/- 20 % using 3 m^3/s as a VFR_{base} . Figure (10-4) display the relative separation efficiency $\left(\frac{\eta(VFR) - \eta(VFR_{base})}{\eta(VFR_{base})} \right)$ as a function of the particle diameter.

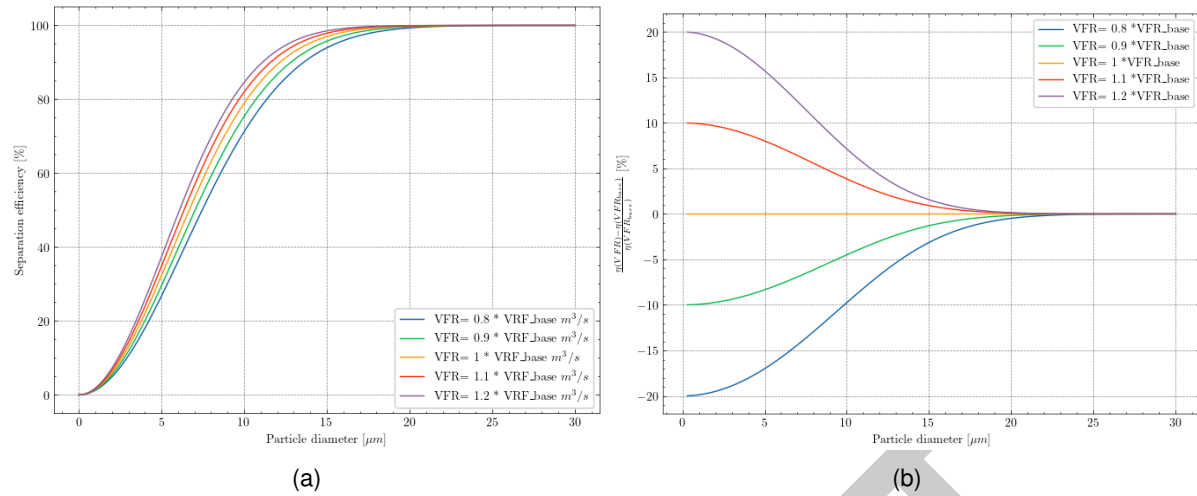


Figure 10-4

Figure (10-4) shows that the efficiency increases proportionally to the increase in VRF when the particle diameter is low. As the diameter of the particle increases, the effect of increasing VRF begins to decrease. However, it must be taken into account that the pressure loss varies with the square of the velocity in the inlet ($\Delta p \propto v_{inlet}^2$), so if the flow rate changes 10% the pressure loss would increase by approximately 21%.

10.4 Optimization methodology

In the previous section, the dimensions of a cyclone present in ref.[71] were used. That cyclone was used as a reference to see how the efficiency change for some parameters of interest such as temperature or flow rate, but said geometry was not optimal for the problem to be solved. For this reason, in this section the optimization process of the cyclone geometry is presented to maximize the separation efficiency, using both the fluid and the particle materials of interest for the problem.

10.4.1 Geometrical optimization

The next section presents how the optimization process was developed. For this, the Python library `Optimize` is used and `SLSQP` (Sequential Least Squares Programming) is used as the optimization method. In order to use this method, it is necessary to define the function to be minimized, the variables and both geometric and performance limitations.

In order to define the function, if a target efficiency η_{target} is defined, according to equation (71) the radial velocity of the particle is

$$v_{r,p} = -\frac{\ln(1 - \eta_{target})}{2t_{res}} \cdot R^* w \quad (72)$$

On the other hand, using the equation (54), (62) and (64) the diameter of the particle can be expressed

as:

$$d_p^2 = \frac{18\mu v_{r,p}(R^* w) R^* w}{\Delta \rho v_{\theta,f}^2(R^* w)} \quad (73)$$

$$d_p^2 = -\frac{\ln(1 - \eta_{target})}{2t_{res}} \cdot \frac{18\mu R^* w^2}{\Delta \rho v_{\theta,f}^2(R^* w)} \quad (74)$$

$$d_p^2 = -\frac{\ln(1 - \eta_{target})}{2t_{res}} \cdot \frac{18\mu R^*(2+2n)}{\kappa^2} \quad (75)$$

where the diameter of the particle is defined as a function of the target efficiency, inlet velocity (present in the parameter κ) and geometry (present in t_{res} , $R^* w$ and κ). With this information, was used as a function to minimize, the cut diameter defined as the particle diameter for which the capture efficiency is equal to 50 % $d_{p,c} = d_p(\eta = 50\%)$:

$$d_{p,c}(\vec{x}) = \left(-\frac{\ln(0.5)}{2t_{res}} \cdot \frac{18\mu R^*(2+2n)}{\kappa^2} \right)^{1/2} \quad (76)$$

where $\vec{x} = (D, D_e, H, B, h, S, a, b)$ is the vector with all of geometrical variables of the cyclone.

In order to close the problem, the constrains used were:

1. $h > S$
2. $h > a$
3. $D > D_e + b$
4. $D_e > b$
5. $H > S$
6. $H > h$
7. $D_e > B$
8. $10^\circ < \alpha < 20^\circ$, where $\alpha = \arctan\left(\frac{D-B}{2(H-h)}\right)$
9. $v_{inlet} < v_{max}$

Given that the problem has 8 variables there are only inequalities as a constrains, more than one local minimum may exist within the domain. For this reason, the optimizer was initialized with different seeds in order to obtain the different local minima present in the domain. Then, a family of cyclones was obtained that meet the conditions within the domain, where the cutting diameter varies by less than 10% and the geometric dimensions change.

10.4.2 Optimization: Results

Table (10-2) show the total volumetric mass flow rate for the commercial and pilot plant calculated in ref. [75].

Parameter	Pilot plant	Commercial plant
VFR per loop [m ³ /s]	3.27	4.9
VFR total [m ³ /s]	3.27	29.4

Table 10-2: Volumetric flow rate for the pilot and commercial plant calculated in ref. [75]

For the optimization process, a parametric analysis was carried out where the VFR was varied in the inlet of the cyclone in order to have the same operating conditions in the cyclone for both the commercial and pilot plants and, consequently, the highest separation efficiency with the minimum loss of energy. The ratio between the VFR of the commercial plant and the pilot plant is approximately 9 ($\frac{(VFR_{total})_{commercial}}{(VFR_{total})_{pilot}} \approx 9$) so if you want to have the same efficiency for both plants, it is necessary to increase the number of cyclones 9 times when scaling the plant from the pilot to the commercial one.

Figure (10-5a) ,(10-5b) and (10-5c) shows the cut off diameter ($\eta = 50\%$) for the Fe, Cr and AlN, respectively. For this analysis, it has been used that the maximum velocity in the inlet has to be less than 25 m/s.

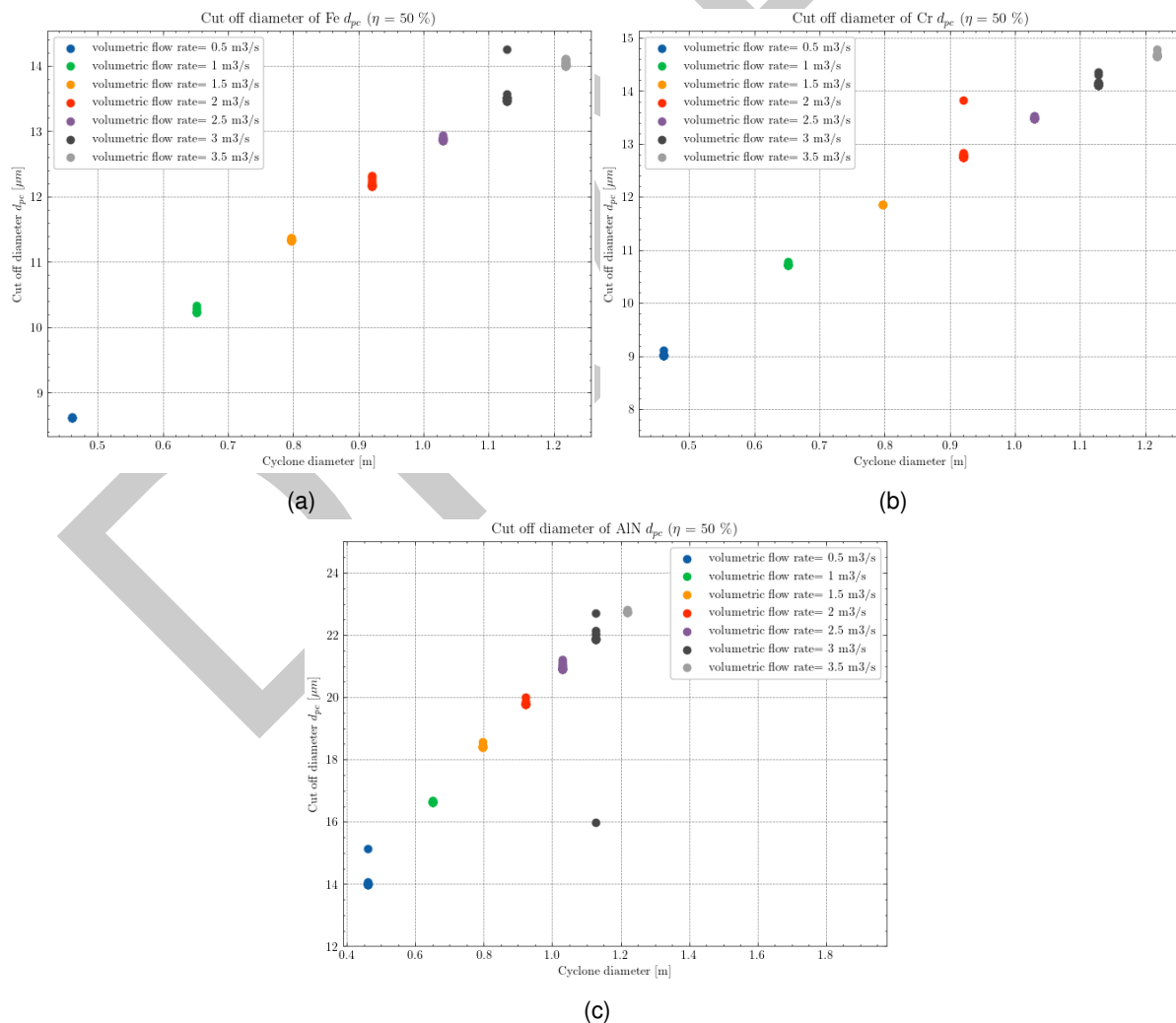


Figure 10-5

It can be seen that the cutting diameter of both Fe and Cr are quite similar and smaller than that of AlN. This is because the density of Fe is similar to that of Cr, while the density of AlN is much lower. This causes the radial velocity of the particle towards the walls to be lower and the efficiency tends to decrease, so the diameter of the particle must be larger to be captured.

Since the inlet maximum velocity was limited in the optimization process, when the volumetric flow rate increase the cyclone diameter and the inlet dimensions have to grow to have enough space to allocate the inlet and reduce the velocity.

Table (10-3) presents the dimensions of 5 cyclones that can operate at different VFRs. In addition, the cutting diameter for Fe, Cr and AlN is presented and an estimate of the number of cyclones that could be used either in the commercial plant or in the pilot plant.

Cyclone case	I	II	III	IV	V
Cyclone body diameter (m)	0.460	0.651	0.797	0.921	1.030
Liquid outlet diameter (vortex finder diameter) (m)	0.211	0.291	0.357	0.412	0.461
Cyclone inlet height (m)	0.230	0.326	0.399	0.460	0.515
Cyclone inlet width (m)	0.092	0.130	0.159	0.184	0.206
Liquid outlet duct length (m)	0.436	0.620	0.760	0.877	0.981
Cyclone cylinder height (m)	1.483	2.063	2.526	2.917	3.261
Cyclone height (m)	0.460	0.651	0.797	0.921	1.030
Particle outlet diameter (m)	0.046	0.065	0.080	0.092	0.103
Angle (°)	11.453	11.723	11.732	11.731	11.731
Inlet VFR (m³/s)	0.5	1.0	1.5	2.0	2.5
Inlet Velocity (m/s)	23.585	23.585	23.585	23.585	23.585
Cut off diameter Fe (microns)	8.610	10.230	11.322	12.053	12.864
Cut off diameter Cr (microns)	9.013	10.468	11.861	12.746	13.477
Cut off diameter AlN (microns)	10.207	16.620	18.393	19.765	21.215
Number of cyclone pilot plant	6	3	2		
Number of cyclone commercial plant	54	27	18		

Table 10-3: Cyclone optimization results

It can be seen that as the volumetric flow rate at the inlet increases, the cut off diameter decrease for all the particles analyzed, causing the loss of separation efficiency. On the other hand, in order to choose the correct cyclone, the total pressure loss of the system have to be considered. In the literature there are a large number of correlations to calculate pressure loss [69, 70], however these are developed mainly for gas-solid cyclones and not for liquid-solid as in this case. For this reason, in the CFD section,

importance will be given to the calculation of said parameter.

DRAFT

10.5 Conceptual Design Approach

In the forthcoming project phases, the conceptual design will navigate the design space between the hydrocyclone and Disk Stack Separator, aiming to optimize the multi-stage purification process. With the requirements outlined in Section 9.1 and the technical specifications detailed in Figure 9-4 serving as foundational guidelines, the design endeavor will seek to exploit the current capabilities of the multi-stage purification system. Drawing inspiration from external sources, such as referenced paper ref. [76], the conceptual design will explore innovative approaches (Figure 10-6) to enhance particle capture efficiency, impurity removal, and overall system performance.

Integration of advanced materials, novel geometries, and optimized operational parameters will be central to the conceptual design exploration. By leveraging insights from existing research and technological advancements, the conceptual design aims to push the boundaries of purification efficiency, ultimately culminating in the development of a device that maximizes the potential of the multi-stage purification process.

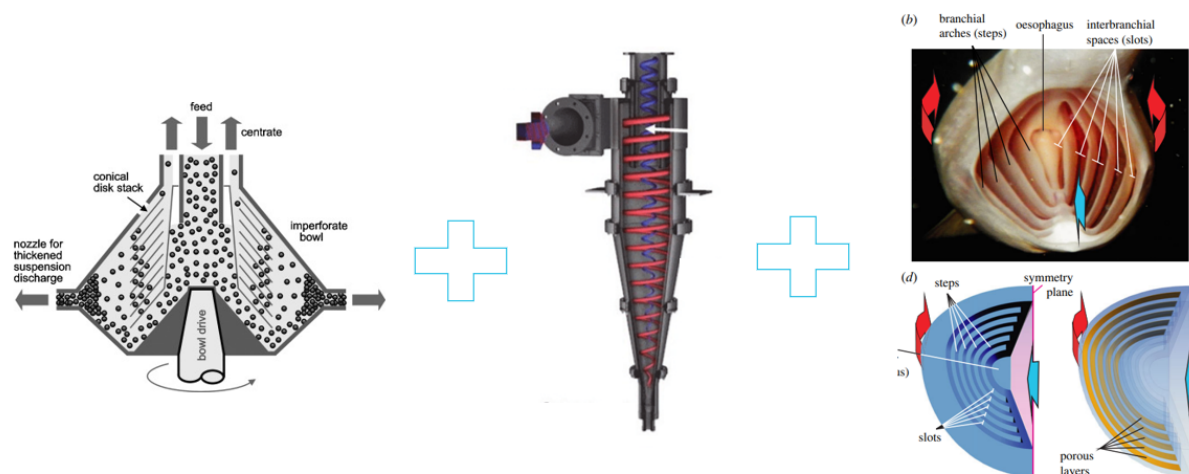


Figure 10-6: Conceptual design approach: possible lines of work

11 CONCLUSIONS

XX

DRAFT

References

- [1] NIST. "SI - Unit rules and style conventions". In: 1 (2003), p. 5.
- [2] IDOM S22641_SOA001_v.0. "Liquid Lithium solid impurities cyclone separator: SoA and Material assessment". In: (2023).
- [3] A. Ott. "Impurity Diffusion in Lithium 1. The Diffusion of Cd, Hg and Ga 2. Survey of the Diffusion of Metallic Impurities in Lithium". In: *J. Phys. Sci.* (1970). DOI: 10.1515/ZNA-1970-1020.
- [4] Robert F Keough and George E Meadows. "Lithium purification technique". In: (Jan. 1985). URL: <https://www.osti.gov/biblio/865506>.
- [5] O. K. Chopra and A. B. Hull. "Influence of carbon and nitrogen impurities on the corrosion of structural materials in a flowing lithium environment". In: (1988).
- [6] T. Muroga et al. "Compatibility of Reduced Activation Ferritic/Martensitic Steels with Liquid Breeders". In: (2008).
- [7] Annette Heinzel, Masatoshi Kondo, and Minoru Takahashi. "Corrosion of steels with surface treatment and Al-alloying by GESA exposed in lead–bismuth". In: *Journal of Nuclear Materials* 350.3 (May 2006), pp. 264–270. ISSN: 0022-3115. DOI: 10.1016/j.jnucmat.2006.01.014.
- [8] IAEA. *Challenges For Coolants In Fast Neutron Spectrum Systems*. 2020.
- [9] P.A. Finn, S.R. Breon, and N.R. Chellew. "Compatibility study of solid ceramic breeder materials". In: *Journal of Nuclear Materials* 103 (Jan. 1981), pp. 561–566. ISSN: 0022-3115. DOI: 10.1016/0022-3115(82)90658-4. URL: [http://dx.doi.org/10.1016/0022-3115\(82\)90658-4](http://dx.doi.org/10.1016/0022-3115(82)90658-4).
- [10] Richard J. Pulham, W. Robert Watson, and John S. Collinson. "Chemical compatibility between Lithium Oxide and transition metal". In: *Journal of Nuclear Materials* (1984).
- [11] Sanjit Kumar Parida et al. "Studies on chemical compatibility of steels with liquid lithium". In: *Journal of Nuclear Materials* 526 (Dec. 2019), p. 151761. ISSN: 0022-3115. DOI: 10.1016/j.jnucmat.2019.151761.
- [12] Wenxing Xia et al. "Study of corrosion behaviors of 316L Stainless steel welds in liquid lithium with hydrogen impurity". In: 2019. URL: <https://doi.org/10.1080/15361055.2018.1533618>.
- [13] Tortorelli P. F, J. H. DeVan, and J. E. Selle. "Corrosion in Lithium-Stainless Steel thermal convection systems". In: (1980).
- [14] V. TSISAR et al. "Morphological and Compositional Features of Corrosion Behavior of SUS410-SUS410, SUS316-SUS316 and SUS410-SUS316 TIG Welded Joints in Li". In: 2012. URL: <https://doi.org/10.1080/15361055.2018.1533618>.
- [15] Victor A. Maroni, Raymond D. Wolson, and Gustav E. Staahl. "Some Preliminary Considerations of A Molten-Salt Extraction Process to Remove Tritium from Liquid Lithium Fusion Reactor Blankets". In: *Nuclear Technology* 25.1 (Jan. 1975), pp. 83–91. ISSN: 1943-7471. DOI: 10.13182/nt75-a24351. URL: <http://dx.doi.org/10.13182/NT75-A24351>.

- [16] Todd M. Bandhauer and J. Adler. "ALTERNATIVE METHODS FOR TRITIUM RECOVERY FROM THE LIFELITHIUM BLANKET: FY13 FINAL REPORT". In: 2013. URL: <https://api.semanticscholar.org/CorpusID:43604591>.
- [17] J. Z. Zhu et al. *Three-dimensional phase-field simulations of coarsening kinetics of particles in binary Ni-Al alloys*. May 2004, pp. 2837–2845. DOI: 10.1016/j.actamat.2004.02.032.
- [18] Luneville et al. *Reconciliation of simulation and experiment*. 2022, p. 184102. DOI: 10.1063/5.0122126. URL: <https://hal.science/hal-04101531>.
- [19] C Sommitsch et al. *A Precipitation Model for Multi-Component Multi-Phase Systems in Nickel-Base Superalloys*.
- [20] Larissa V Bravina and Eugene E Zabrodin. *Homogeneous nucleation: Comparison between two theories*.
- [21] M. Volmer and A.Z. Weber. "Nucleus Formation in Supersaturated Systems". In: *Zeitschrift für Physikalische Chemie* 119 (1926), pp. 277–301.
- [22] Mitsuhiko Hayashi and Takaki Shichiri. *THEORETICAL AND EXPERIMENTAL STUDY OF THE GROWTH OF PERFECT CRYSTALS*. 1974.
- [23] Gerald. Wilemski. "Revised classical binary nucleation theory for aqueous alcohol and acetone vapors". In: *The Journal of Physical Chemistry* 91.10 (1987), pp. 2492–2498. DOI: 10.1021/j100294a011. eprint: <https://doi.org/10.1021/j100294a011>. URL: <https://doi.org/10.1021/j100294a011>.
- [24] László Gránásy and Ferenc Iglói. "Comparison of experiments and modern theories of crystal nucleation". In: *The Journal of Chemical Physics* 107.9 (Sept. 1997), pp. 3634–3644. ISSN: 0021-9606. DOI: 10.1063/1.474721. eprint: https://pubs.aip.org/aip/jcp/article-pdf/107/9/3634/19140858/3634_1_online.pdf. URL: <https://doi.org/10.1063/1.474721>.
- [25] Mikhail P. Anisimov. "Nucleation: theory and experiment". In: *Russ. Chem. Rev.* 72 (7 2003), pp. 591–628. DOI: 10.1070/RC2003v072n07ABEH000761. URL: <http://dx.doi.org/10.1070/RC2003v072n07ABEH000761>.
- [26] László Gránásy and P. F. James. "Non-classical theory of crystal nucleation: Application to oxide glasses: Review". In: *Journal of Non-Crystalline Solids* 253 (1-3 1999), pp. 210–230. ISSN: 00223093. DOI: 10.1016/S0022-3093(99)00354-3.
- [27] Emmanuel Clouet. *Modeling of Nucleation Processes*, pp. 203–219.
- [28] Allan S. Myerson, Deniz Erdemir, and Alfred Y. Lee. *Crystal nucleation*. Jan. 2019. DOI: 10.1017/9781139026949.003.
- [29] I. J. Ford. "Statistical mechanics of nucleation: A review". In: *Proceedings of the Institution of Mechanical Engineers, Part C: Journal of Mechanical Engineering Science* 218 (8 Aug. 2004), pp. 883–899. ISSN: 09544062. DOI: 10.1243/0954406041474183.
- [30] Yuzhu Sun et al. "Primary nucleation of lithium carbonate". In: vol. 3. Mar. 2009, pp. 73–77. DOI: 10.1007/s11705-009-0091-y.

- [31] Ian Ford. *Thermodynamics and Kinetics of Nucleation*.
- [32] Vladimir M. Fokin et al. *Homogeneous crystal nucleation in silicate glasses: A 40 years perspective*. Aug. 2006. DOI: 10.1016/j.jnoncrysol.2006.02.074.
- [33] G F Neilson and M C Weinberg. *A TEST OF CLASSICAL NUCLEATION THEORY: CRYSTAL NUCLEATION OF LITHIUM DISILICATE GLASS*. 1979, pp. 137–147.
- [34] K. F. Kelton, A. L. Greer, and C. V. Thompson. *Transient nucleation in condensed systems*. 1983, pp. 6261–6276. DOI: 10.1063/1.445731.
- [35] Laszlo Granasy and Peter F. James. *Transient nucleation in oxide glasses: The effect of interface dynamics and subcritical cluster population*. July 1999, pp. 737–749. DOI: 10.1063/1.479353.
- [36] Laszlo Granasy and Peter F. James. *Nucleation and growth in cluster dynamics: a quantitative test of the classical kinetic approach*. Dec. 2000, pp. 9810–9821. DOI: 10.1063/1.1322030.
- [37] J Bartels et al. *Evolution of cluster size distribution in nucleation and growth processes*. 1991.
- [38] Y.A. Odusote and A.I Popoola. “Thermodynamic Prediction of the Free Energy of Mixing and Activities of some Goldbased Binary Liquid Alloys”. In: *Nigeria Journal of Pure and Applied Physics* 9 (1 Apr. 2020), pp. 11–16. DOI: 10.4314/njpap.v9i1.3.
- [39] Shahsit Kumar Yadav et al. “Mixing Properties of Cu-Mg Liquid Alloy Using Exponential Model”. In: *Journal of Institute of Science and Technology* 28 (1 June 2023), pp. 91–101. ISSN: 2467-9062. DOI: 10.3126/jist.v28i1.54594.
- [40] G S Was and R M Kruger. *A THERMODYNAMIC AND KINETIC BASIS FOR UNDERSTANDING CHROMIUM DEPLETION IN Ni-Cr-Fe ALLOYS*. 1985, pp. 841–854.
- [41] Deepak Kumar. *PHYSICA Nucleation in binary mixtures*. 1996, pp. 128–139.
- [42] H. Ulbricht et al. *Thermodynamics of Finite Systems and the Kinetics of First Order Phase Transitions*. Leipzig: Teubner, 1998.
- [43] Vladimir M. Fokin et al. “Homogeneous crystal nucleation in silicate glasses: A 40 years perspective”. In: *Journal of Non-crystalline Solids* 352 (2006), pp. 2681–2714. URL: <https://api.semanticscholar.org/CorpusID:13793660>.
- [44] Keshra Sangwal. “Effects of impurities on crystal growth processes”. In: *Progress in Crystal Growth and Characterization of Materials* 32.1 (1996), pp. 3–43. ISSN: 0960-8974. DOI: [https://doi.org/10.1016/0960-8974\(96\)00008-3](https://doi.org/10.1016/0960-8974(96)00008-3). URL: <https://www.sciencedirect.com/science/article/pii/0960897496000083>.
- [45] Shiyang Sun et al. “First principle calculations study of AlN surface terminal structure evolution under different conditions”. In: *Surface and Interface Analysis* 52 (4 Apr. 2020), pp. 167–173. ISSN: 10969918. DOI: 10.1002/sia.6737.
- [46] J. Y. Lee et al. “The surface energy and stress of metals”. In: *Surface Science* 674 (Aug. 2018), pp. 51–68. ISSN: 00396028. DOI: 10.1016/j.susc.2018.03.008.
- [47] L Vitos et al. *The surface energy of metals*. 1998, pp. 186–202.

- [48] David Holec and Paul H. Mayrhofer. "Surface energies of AlN allotropes from first principles". In: *Scripta Materialia* 67 (9 Nov. 2012), pp. 760–762. ISSN: 13596462. DOI: 10.1016/j.scriptamat.2012.07.027.
- [49] S. J. Binnie et al. "Bulk and surface energetics of crystalline lithium hydride: Benchmarks from quantum monte carlo and quantum chemistry". In: *Physical Review B - Condensed Matter and Materials Physics* 82 (16 Oct. 2010). ISSN: 10980121. DOI: 10.1103/PhysRevB.82.165431.
- [50] Ana Rosa Silva et al. "SURFACE TENSION CALCULATION OF Si-Zr ALLOYS FOR REACTIVE MELT INFILTRATION OF SiC AND/OR ZrC BASED CERAMIC COMPOSITES". In: *Research and Reviews in Materials Science and Chemistry* 6 (2 2016), pp. 115–130. ISSN: 2319-6920. URL: <http://jyotiacademicpress.net>.
- [51] Radim Picha, Jan Vřešťál, and Aleš Kroupa. "Prediction of alloy surface tension using a thermodynamic database". In: *Calphad: Computer Coupling of Phase Diagrams and Thermochemistry* 28 (2 June 2004), pp. 141–146. ISSN: 03645916. DOI: 10.1016/j.calphad.2004.06.002.
- [52] Valery P. Krasin and Svetlana I. Soyustova. "Thermodynamic analysis of chromium solubility data in liquid lithium containing nitrogen: Comparison between experimental data and computer simulation". In: *Journal of Nuclear Materials* 465 (July 2015), pp. 674–681. ISSN: 00223115. DOI: 10.1016/j.jnucmat.2015.06.061.
- [53] Adam S. Skapski. "A theory of surface tension of solids—I application to metals". In: *Acta Metallurgica* 4 (1956), pp. 576–582. URL: <https://api.semanticscholar.org/CorpusID:95773455>.
- [54] S. N. Zadumkin and A. A. Karashaev. "Surface energy at metal/dielectric liquid interfaces". In: *Soviet materials science : a transl. of Fiziko-khimicheskaya mekhanika materialov / Academy of Sciences of the Ukrainian SSR* 1 (1966), pp. 86–88. URL: <https://api.semanticscholar.org/CorpusID:137028357>.
- [55] Frans Spaepen. "A structural model for the solid-liquid interface in monatomic systems". In: *Acta Metallurgica* 23 (1975), pp. 729–743. URL: <https://api.semanticscholar.org/CorpusID:137397767>.
- [56] Carl V. Thompson and Frans Spaepen. "Homogeneous crystal nucleation in binary metallic melts". In: *Acta Metallurgica* 31 (1983), pp. 2021–2027. URL: <https://api.semanticscholar.org/CorpusID:136589124>.
- [57] K F Kelton and A L Greer. *TRANSIENT NUCLEATION EFFECTS IN GLASS FORMATION*. 1986, pp. 295–309.
- [58] C. W. Bale et al. "FactSage Thermochemical Software and Databases - 2010 - 2016". In: *Calphad* 54 (2016), pp. 35–53.
- [59] H. W. Leavenworth and Robert E. Cleary. "The solubility of Ni, Cr, Fe, Ti and Mo in liquid lithium". In: *Acta Metallurgica* 9 (1961), pp. 519–520. URL: <https://api.semanticscholar.org/CorpusID:93159840>.

- [60] Kateryna Khanchych and Carsten Schroer. "Compatibility of EUROFER97 and leadlithium eutectic". In: *Nuclear Materials and Energy* 37 (2023), p. 101527. ISSN: 2352-1791. DOI: <https://doi.org/10.1016/j.nme.2023.101527>. URL: <https://www.sciencedirect.com/science/article/pii/S2352179123001667>.
- [61] Yizhou Zhu, Xingfeng He, and Yifei Mo. "Strategies Based on Nitride Materials Chemistry to Stabilize Li Metal Anode". In: *Advanced Science* 4 (Mar. 2017). DOI: 10.1002/advs.201600517.
- [62] Patrick J. Crowley, Kevin P. Scanlan, and Arumugam Manthiram. "Diffusional lithium trapping as a failure mechanism of aluminum foil anodes in lithium-ion batteries". In: *Journal of Power Sources* 546 (2022), p. 231973. ISSN: 0378-7753. DOI: <https://doi.org/10.1016/j.jpowsour.2022.231973>. URL: <https://www.sciencedirect.com/science/article/pii/S0378775322009545>.
- [63] Ewald Veleckis, Erven H. Van Deventer, and Milton Blander. "THE LITHIUM-LITHIUM HYDRIDE SYSTEM". In: *ChemInform* 5 (1974). URL: <https://api.semanticscholar.org/CorpusID:101555746>.
- [64] F J Smith, J F Land, and G M Begun. *THE SOLUBILITY AND ISOTOPIC EXCHANGE EQUILIBRIUM FOR HYDROGEN ISOTOPES IN LITHIUM*t. 1979, pp. 1001–1009.
- [65] Man Wang et al. "Thermodynamic modeling of the Li-H and Ca-H systems". In: *Journal of Phase Equilibria and Diffusion* 33 (2 Apr. 2012), pp. 89–96. ISSN: 15477037. DOI: 10.1007/s11669-012-9997-z.
- [66] H. Katsuta, T. Ishigai, and K. Furukawa. "Equilibrium pressure and solubility of hydrogen in liquid lithium". In: *Nuclear Technology* 32 (3 1977), pp. 297–303. ISSN: 00295450. DOI: 10.13182/NT77-A31753.
- [67] E Veleckis, R M Yonco, and V A Maroni. *SOLUBILITY OF LITHIUM DEUTERIDE IN LIQUID LITHIUM*. 1977, p. 85.
- [68] Konstantin A. Yakimovich and Tatiana Biryukova. "Thermodynamic Properties of Li-LiH (LiD, LiT) Systems. The Phase Diagram". In: *Open Journal of Physical Chemistry* 02 (03 2012), pp. 141–146. ISSN: 2162-1969. DOI: 10.4236/ojpc.2012.23019.
- [69] F. Concha. "Flow pattern in Hydrocyclones". In: *Department of Metallurgical Engineering, University of Concepcion* (2007).
- [70] S. Altmeyer et al. "Comparison of different models of cyclone prediction performance for various operating conditions using a general software". In: *Chemical Engineering and Processing* 43 (2003).
- [71] Bingtao Zhao. "Prediction of gas-particle separation efficiency for cyclones: A time-of-flight model". In: *Separation and Purification Technology* 85 (2011), pp. 171–177.
- [72] Wang Wei et al. "A new Method of Prediction the Hydrocyclone Efficiency with the Light Dispersed Phase". In: *International Conference of Applied Energy* (2016).
- [73] Svein Arne Marthinussen. "The Effect of Fluid Viscosity on Hydrocyclone Performance". In: *Department of Physics and Technology University of Bergen* (2011).

- [74] Reza Sabbagh et al. "Theoretical and experimental study of hydrocyclone performance and equivalent setting area". In: *ASME* (2014).
- [75] IDOM. "Reactor Chamber design: power scenario analysis". In: *SIM007 v.1* (2023).
- [76] S. Van Wassenbergh and S. L. Sanderson. "Hydrodynamic analysis of bioinspired vortical cross-step filtration by computational modelling". In: 2023. URL: <https://doi.org/10.1098/rsos.230315>.

DRAFT

ANNEX 1

Evaluation	units	CC	Decanter centrifuge	Disk Stack	Hydrocyclone
Continuous extraction	yes/not	yes	yes	yes	yes
Material compatibility	-	SS	SS	SS	SS/Polymers
Energy cost ¹	kW	18.5	250	75	0
Particle size	μm	NRAI ²	>10	>1	>12
Maintenance & cleaning	-	moving parts	moving parts	moving parts	excellent
Max. flow rate	m^3/s	0.012	0.007	0.028	0.5
Impurities concentration	%	NRAI ²	>10%	>0.02%	>10%
Centrifugal force	G	2000	4000	14000	5000

Table 11-1: Centrifugal separator comparison data-sheet

DRAFT

¹ Based on required engine power to achieve the operation centrifugal force, for comparative reasons.

² Not Reasonable Available Information.